

2015

# MEMS-compatible processes for fabricating nanostructures and their applications

Yuan He

*Iowa State University*

Follow this and additional works at: <https://lib.dr.iastate.edu/etd>

 Part of the [Electrical and Electronics Commons](#)

## Recommended Citation

He, Yuan, "MEMS-compatible processes for fabricating nanostructures and their applications" (2015). *Graduate Theses and Dissertations*. 14563.

<https://lib.dr.iastate.edu/etd/14563>

This Dissertation is brought to you for free and open access by the Iowa State University Capstones, Theses and Dissertations at Iowa State University Digital Repository. It has been accepted for inclusion in Graduate Theses and Dissertations by an authorized administrator of Iowa State University Digital Repository. For more information, please contact [digirep@iastate.edu](mailto:digirep@iastate.edu).

# **MEMS-compatible processes for fabricating nanostructures and their applications**

by

**Yuan He**

A dissertation submitted to the graduate faculty  
in partial fulfillment of the requirements for the degree of

DOCTOR OF PHILOSOPHY

Major: Electrical Engineering

Program of Study Committee:

Long Que, Major Professor

Liang Dong,

Jaeyoun Kim,

Meng Lu,

Ian C Schneider

Iowa State University

Ames, Iowa

2015

Copyright © Yuan He, 2015. All rights reserved

## TABLE OF CONTENTS

<b>ACKNOWLEDGEMENTS</b> .....	<b>v</b>
<b>PREFACE AND DISSERTATION ORGANIZATION</b> .....	<b>vi</b>
<b>ABSTRACT</b> .....	<b>viii</b>
<b>CHAPTER 1 INTRODUCTION TO PLASMA ETCHING TECHNOLOGY</b> .....	<b>1</b>
1.1 TYPES OF PLASMA ETCHING .....	1
1.2 PHYSICAL DESCRIPTION OF PLASMA ETCHING.....	2
1.21 Physics of DC Plasma.....	2
1.22 Physics of AC Plasma.....	4
1.3 PLASMA COMPOSITION .....	7
1.4 ETCHING PROCESS STEPS .....	8
<b>CHAPTER 2 INDUCTIVELY COUPLED PLASMA REACTIVE ION ETCHING</b> .....	<b>10</b>
2.1 ADVANTAGES OF ICP .....	10
2.2 MAJOR COMPONENTS OF ICP SYSTEM .....	12
2.3 ALCATEL GUI AND IN SITU MONITORING .....	15
2.4 BOSCH PROCESS .....	17
<b>CHAPTER 3 CHARACTERIZATION OF THE SILICON NANOPILLAR-SURFACE FILLED WITH NANOMATERIALS</b> .....	<b>24</b>
3.1 INTRODUCTION TO NANOPILLAR-SURFACE FILLED WITH NANOMATERIALS.....	24
3.2 EXPERIMENTAL DETAILS .....	26
3.2.1 Chemicals and materials.....	26
3.2.2 Fabrication of silicon nanopillar-surface filled and grafted with nanomaterials .....	27
3.2.3 Characterization.....	29
3.3 RESULTS AND DISCUSSION.....	30
3.3.1 Fabricated Arrayed Nanopillars .....	30
3.3.2 Contact angle measurements and surface topology of the nanopillar surface.....	31
3.3.3 Reflectance from surface with and without nanopillars.....	33
3.3.4 Reflectance measurements under different incident angles.....	35
3.3.5 Reflectance measurements of the nanopillar surface filled and grafted with different nanomaterials.....	37
3.4 CONCLUSION .....	39
<b>CHAPTER 4 SURFACE ENHANCED RAMAN SPECTROSCOPY (SERS) SUBSTRATE BASED ON SILICON NANOFORREST</b> .....	<b>41</b>
4.1 INTRODUCTION TO NANOFORREST FORMATION .....	41
4.2 EXPERIMENTAL DETAILS.....	43
4.2.1 Chemicals and Materials.....	43

4.2.2 Fabrication of the Silicon Nanoforest Surface .....	43
4.2.3 Characterization.....	45
4.3 RESULTS AND DISCUSSION.....	46
4.3.1 Fabricated Nanoforest .....	46
4.3.2 R6G SERS Measurement on Nanoforest .....	47
4.3.3 SERS Measurement on Gold-coated Nanoforest .....	49
4.3.4 SERS Measurement on Ag Particles Decorated Au-coated Silicon Nanoforest .....	51
4.3.5 Cell SERS Measurement on Au-coated Silicon Nanoforest .....	52
4.4 CONCLUSIONS.....	56
<b>CHAPTER 5 A TOP-DOWN FABRICATION PROCESS FOR VERTICAL SILICON NANOTUBES .....</b>	<b>57</b>
5.1 INTRODUCTION TO NANOTUBE FABRICATION .....	57
5.2 EXPERIMENTAL DETAILS .....	60
5.2.1 Chemicals and Materials.....	60
5.2.2 Fabrication of silicon nanotubes.....	61
5.2.3 Characterization.....	62
5.3 RESULTS AND DISCUSSION .....	62
5.4 CONCLUSIONS.....	72
<b>CHAPTER 6 ICP ETCHING TECHNOLOGY: GENERAL ANALYSIS AND DISCUSSION .....</b>	<b>74</b>
6.1 PHYSICAL PARAMETERS .....	74
6.2 CHEMICAL COMPOSITION.....	76
6.3 CONCLUSION .....	79
<b>CHAPTER 7 INTRODUCTION TO PATTERNED ANODIC ALUMINUM OXIDE (AAO) BASED BIOSENSOR .....</b>	<b>80</b>
7.1 INTRODUCTION TO AAO BIOSENSOR.....	80
7.2 INTRODUCTION TO AAO PATTERN FABRICATION .....	82
<b>CHAPTER 8 FABRICATION AND CHARACTERIZATION OF LITHOGRAPHICALLY PATTERNED AND OPTICALLY TRANSPARENT ANODIC ALUMINUM OXIDE (AAO) NANOSTRUCTURE THIN FILM .....</b>	<b>84</b>
8.1 FABRICATION PROCESS INTRODUCTION.....	84
8.2 RESULTS AND DISCUSSION.....	87
8.2.1 Fabricated AAO Nanostructure.....	87
8.2.2 Optical Property Measurement of AAO Nanostructure .....	91
8.3 CONCLUSION .....	96
<b>CHAPTER 9 A TRANSPARENT AAO NANOSTRUCTURED OPTICAL BIOSENSOR.....</b>	<b>97</b>
9.1 DEVICE AND EXPERIMENT DESIGN.....	98
9.1.1 Device Fabrication .....	98
9.1.2 Experiment Design .....	98
9.2 MATERIALS AND METHODS .....	100
9.2.1 Chemicals and Materials.....	100
9.2.2 Biodetection Procedure .....	101
9.2.3 Experimental Data Analysis.....	102
9.3 RESULTS AND DISCUSSION.....	103
<b>CHAPTER 10 AAO NANOSTRUCTURED OPTICAL SENSOR: CONCLUSIONS AND FUTURE WORK .....</b>	<b>107</b>

10.1 CONCLUSIONS.....	107
10.2 FUTURE WORK .....	108
<b>REFERENCES.....</b>	<b>110</b>

## ACKNOWLEDGEMENTS

Foremost, I want to express my sincere gratitude to my advisor, Dr. Long Que, for his generous and continuous support in my Ph.D. study and research, for his patience, motivation, enthusiasm, and immense knowledge. It is my great honor to be his doctoral student. This dissertation could not have been completed without his encouragement and constant guidance.

I would like to thank the rest of my advisory committee: Dr. Liang Dong, Dr. Jaeyoun Kim, Dr. Meng Lu, and Dr. Ian C Schneider, for their kind suggestions and guidance, and thank Dr. Chenxu Yu for helping us with the Raman signal measurement.

I want to thank my fellow labmates: Chao Wang, Zhen Xu, Xuan Qiao, Yifei Wang, Yin Huang, Benjamin Ch'ng and Jacob Nuhn from Iowa State University, Zhongcheng Gong, Pushparaj Pathak, Yi-Hsuan Tseng, Haocheng Yin, Wen-chuan Cheng, Ai-Yi Chang, Xiangchen Che from Louisiana Tech University for sharing their valuable research experience and great support.

I would like to thank MRC staff Dr. Wai Y. Leung, IFM staff members, Mr. Philip Coane, Mr. Ji Fang, Mr. Alfred Gunasekaran, and Mrs. Debbie Wood for the experimental support.

Finally, I would like to thank my family: my father, Aihua He, my mother, Bichi Wang, for their love, understanding and endless encouragement throughout my life.

## PREFACE AND DISSERTATION ORGANIZATION

Although this dissertation is in fulfillment of the PhD degree requirement, this work is also meant to document and summarize the etching and fabrication protocol to ensure that my understanding of process development and modification are available for Dr. Que Long's future group members and students at Iowa State University. It will be my great honor if others find some use or value from my experiments.

This dissertation includes two major parts, introducing two types of fabrication technologies to achieve some unique nanostructures and developing a series of micro-devices based on these nanostructures.

The first section of this dissertation is presented in Chapters 1 through 6, and focuses on the formation and application of high-aspect-ratio silicon nanostructures. In Chapter 1, the concepts of plasma and general mechanism of plasma etching are introduced to better understand the nanostructure formation process. The generation and application of DC and AC plasma are reviewed and discussed, respectively. The types of plasma etching, the composition of plasma, and the major etching steps are also discussed. In Chapter 2, an Alcatel Inductively coupled plasma (ICP) system in the laboratory is used as an example to analyze the major components and working principle of ICP system. A typical ICP etching process, the Bosch process, is described in detail, since it is the key process for silicon nanostructures formation. Chapters 3 through 5 introduce three high-aspect ratio nanostructures, including silicon nanopillars, nanoforests and nanotubes; nanomaterial-grafted nanopillar antireflection surfaces and nanoforest-based Surface Enhanced Raman Spectroscopy (SERS) substrates are also presented. Based on the experimental results from the aforementioned nanostructures,

Chapter 6 shows parameter effects for the tuning etching process and summarizes the achievements of the first section.

The dissertation's second section consists of Chapter 7 through Chapter 10. A nanoporous structure made up of thin film interferometers, based on Anodic aluminum oxide (AAO) nanopores, is introduced. Chapter 7 begins with the currently used label-free biodetection technologies and compares them with the AAO-based interferometer to explain the foundations of our work. Chapter 8 describes the successful fabrication of optically transparent anodic aluminum oxide (AAO) nanostructure thin film from lithographically patterned aluminum on indium tin oxide (ITO) glass substrates. Chapter 9 reports a new transparent nanostructured Fabry-Perot interferometer (FPI) device based on this fabricated substrate. Using this platform, the detection of bioreactions between biomolecules is demonstrated successfully. Finally, Chapter 10 summarizes the achievement from AAO nanostructure fabrication and biosensor platform development and considers possibilities for future research.

## ABSTRACT

During the past decades, many different nanostructures have been successfully synthesized and developed. Due to their nanoscale dimensions, the nanostructures (i.e., nanostructured film, nanotubes, quantum dots) usually exhibit unique optical, electronic, or mechanical properties, which differ from those of the same bulk material. This dissertation focuses on the development and applications of two types of nanostructures: high aspect ratio (HAR) silicon nanostructures and anodic aluminum oxide (AAO) nanopores.

(i) High aspect ratio (HAR) silicon nanostructures, including nanopillars, nanoforest and nanotubes, have attracted enormous attention in the fields of energy harvesting and storage, biomedical sensing, drug delivery, and template-based nanofabrication. Recently, several technologies, such as e-beam lithography and AAO template-based process, have been developed to synthesize HAR nanostructures such as silicon nanotubes. However, these technologies are expensive and usually complicated. In this effort, silicon nanopillars fabrication using nanospheres lithography (NSL) and nanoforest formation through a maskless Bosch process have been successfully developed. Nanomaterial grafted-nanopillar antireflection surface and a nanoforest-based SERS substrate have been demonstrated. Furthermore, a new simple process for fabricating silicon nanotubes at room temperature based on the Bosch process has been developed successfully, offering a unique platform for many potential exciting applications.

(ii) Among many different applications, anodic aluminum oxide (AAO) nanopores have been utilized as nanopore thin film interferometers for biochemical sensing. Using a two-step anodization process, AAO nanopores are usually fabricated from a piece of high purity Al foil.

However, the process is not compatible with a standard lithography- based microfabrication process. As a result, it is very difficult to fabricate arrayed AAO nanopore-based optical microsensors in a cost- effective manner. To address these issues, a new process has been developed to fabricate micropatterned AAO nanopores thin film on glass slide using a standard lithography based microfabrication process. Also, the electron-beam evaporation coated Al thin films become optically transparent after anodization, making it possible to use the transmitted optical signals as the transducing signals. The arrayed AAO thin film-based interferometers have been integrated into a microfluidic chip and the detection of the binding between biomolecules has been demonstrated successfully.

## CHAPTER 1 INTRODUCTION TO PLASMA ETCHING TECHNOLOGY

Plasma etching technology is an essential component for micro/nanofabrication. The industry-used plasma is a mixture of free electrons, ions, neutral radicals and gas molecules. Unlike normal gas or vapor phase compound, the average electron energy (also called electron temperature) is significantly higher than ion energy or ion temperature. It is probably caused by lighter electrons, which have a very poor energy transfer and remain warmer for longer periods of time. [1] Electrons with higher energy collide with molecules to enable high temperature reactions, which occur at relatively low temperatures, since the plasma consists of only a few high-energy electrons. Without a plasma assistant, the high temperature reaction could destroy protection masks or device structures. This chapter will introduce the basic concepts and mechanisms for plasma etching technology. The composition of plasma and major steps of etching will be discussed as well.

### 1.1 Types of Plasma Etching

In plasma etching, substrates are etched in the plasma phase instead of wet chemicals. The solid substrates can be removed physically by ion bombardment, chemically by chemical reaction, or by a combination of the two.

In physical ion etching, high-energy ions bombard the solid sample like millions of tiny balls and sputter the sample's atoms. Chemical reaction does not take place. Since the etching highly depends on the energy or momentum of the ions, the physical ion etching process has a relatively low selectivity and etching rate.

In chemical plasma etching, substrates are explored in a neutral reaction species environment. Gas or vapor phase chemicals, such as chlorine or fluorine, are introduced onto the substrate, where they react with the sample and form volatile products. This type of chemical reaction takes place in the horizontal direction as well as the vertical direction, which results in isotropic etching and undercutting.

In the case of reactive ion etching (RIE), both ions and neutral chemicals contribute to the reaction. High-energy ions damage the sample surface and make the substrate more reactive to chemical species. Ion bombardment is mainly in the vertical direction; the RIE-based processes are more anisotropic compared with chemical etching. Highly reactive species such as neutral radicals would etch the substrate chemically, resulting in a high etching rate under certain circumstances. This dissertation will focus on the development and application of a modified RIE-based etching process for a series of high-aspect ratio silicon nanostructure formation.

## **1.2 Physical Description of Plasma Etching**

### **1.2.1 Physics of DC Plasma**

To explain the mechanism for high-aspect-ratio structure fabrication, a general understanding of plasma is required. The simplest plasma generator consists of two parallel-plate electrodes with DC power supply. A reaction chamber filled with inert gas is maintained at low pressure, from a few mbar to several hundred mbar. The applied DC voltage generates a high electrical potential between electrodes. At the beginning of plasma excitation, an initial current flows through the electrodes. The produced electrons are accelerated by high electrical potential and collide with the inert gas molecules. When electrons with kinetic energy greater than the ionization potential of the inert gas bombard the gas

molecules, the resulting inelastic collisions remove the electrons from the gas molecules. The generated free electrons then collide with other gas molecules and create an avalanche of ions and electrons. With sufficient voltage, the low pressure chamber rapidly becomes filled with ionized inert gas. The discharge current builds up to a point when the voltage drop across the plasma is equal to the applied DC voltage, minus a voltage defined by a current-limiting resistor. Since ions are much heavier than electrons, the average velocity of electrons is larger, and more electrons are captured at the wall. To sustain the plasma, the high-energy ions bombard the cathode and generate secondary electrons.

Typically, the generated plasma consists of free electrons, ions, neutral radicals and gas molecules. The excitation and relaxation process of the plasma also emits visible light, resulting in a soft glow within the chamber. However, dark spaces are observed in certain places, normally near the electrodes. The voltage distribution and the light distribution are shown in Figure 1.1.

Positive ions near the cathode move toward the electrode slower than the electrons move away from it since the ions are much heavier than the electrons. Thus, there are more positive ions in this space compared with electrons. Ions are majority current carriers and move slower, resulting in low conductivity. Therefore, the most significant voltage drop resides at the cathode surface, called the cathode dark space.

The electrons are accelerated away from the cathode by the electric field through the dark space. The high-speed electrons are sped up until their energy is higher than the ionization potential, causing them to collide and ionize the gas molecules to sustain the plasma. When the ions drift into this dark space, they are accelerated toward the cathode by the electric field.

Thus, if a conductor is placed closed to the cathode, the ions bombard the conductor and etch the material. However, if a dielectric is placed in this space, the material rapidly charges. The electric field inside the dielectric is built up, which stops the ions' acceleration and plasma generation.

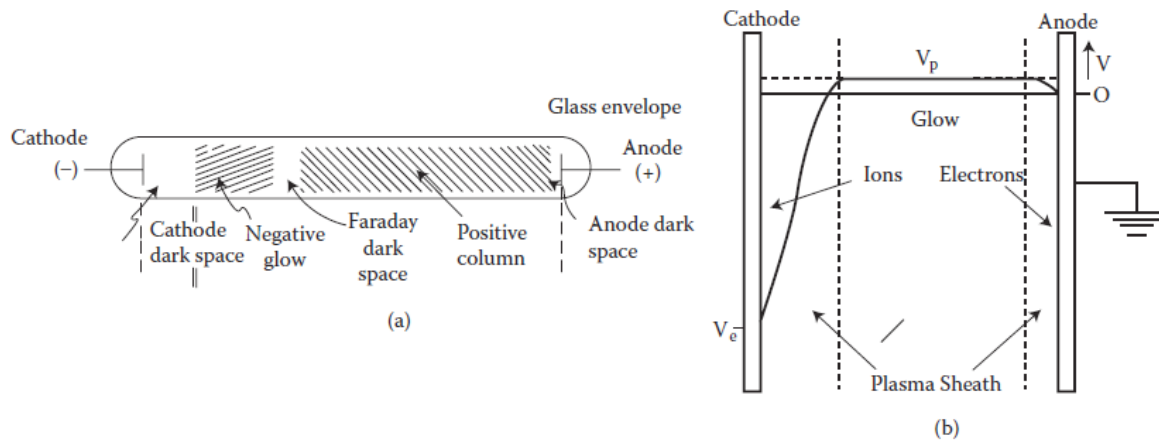


Figure 1.1 (a) Structure of the glow discharge in a long tube-based DC diode system (b) Voltage distribution in a real DC diode system [1]

## 1.22 Physics of AC Plasma

For this reason, high-frequency AC power sources are used for etching silicon wafers. A generated electric field reverses each half-cycle before the dielectric becomes fully charged; thus, the positive charge accumulation during a half-cycle can be neutralized by the next half-cycle. The commonly used frequency is 13.56MHz, chosen because of permission given by the Federal Communications Commission for its lack of interference with radio broadcast signals. In a radio frequency power supply system, the ions cannot respond to the high

frequency change of an electric field. The electrons are forced to oscillate at the same frequency since they are much lighter than ions; the result is sustainable plasma.

The differences between reactors, such as the capacitively coupled plasma reactor (CCP) or inductively coupled plasma reactor (ICP) will be discussed in detail in following chapters. Here we may examine the simple planar parallel-plate reactor. Substrates are placed on the cathode and sputtered as shown in Figure 1.2. When initiating an AC current to the system, a DC bias is induced by the plasma itself and established as follows. Since electrons are lighter than ions, they rapidly charge up the capacitively coupled electrode during the first half cycle. Because electrons cannot be transferred between parallel-plates of the capacitor, the charged electrode surface shows a negative DC bias, called self-bias voltage. The energy of ions bombarding the substrate is a key factor to the sputtering or etching process, which is determined by three potentials in the reaction chamber: the plasma potential, the self-bias voltage and the applied RF source voltage. The plasma potential  $V_p$ , DC cathode potential  $V_{DC}$ , and RF voltage  $(V_{RF})_{PP}$  are related as shown in Figure 1.3 or Equation 1.1 [1]:

$$2V_p \sim \frac{(V_{RF})_{PP}}{2} - |V_{DC}| \quad (1.1)$$

One of the most important etching conditions is the ions' bombardment energy. On the cathode of the reactor, the energy of the ions is:

$$E_{max} = e(|V_{DC}| + V_p) = eV_T \quad (1.2)$$

Meanwhile, the energy of the ions on the anode is given as:

$$E_{max} = e(V_p) \quad (1.3)$$

Typical values for industry-used RIE reactors are several hundred electron volts for the cathode and a few electron volts for the anode. To avoid anode etching,  $V_p$  should be kept small and reactor construction should be carefully designed to ensure the area of the cathode is significantly smaller than the anode, since the plasma potential is determined by the relative area of anode and cathode according to [1]:

$$\frac{V_T}{V_P} = \left(\frac{A_P}{A_T}\right)^4 = R^4 \quad (1.4)$$

To achieve a relatively small cathode, the anode and the chamber wall are grounded, creating a very small anode electron voltage. Thus, little sputtering takes place on the anode electrode.

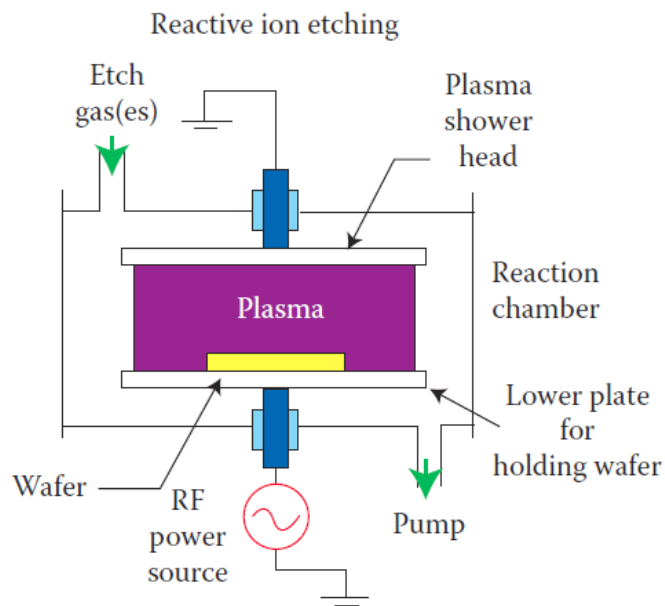


Figure 1.2 Two electrode setup for RF ion sputtering [1]

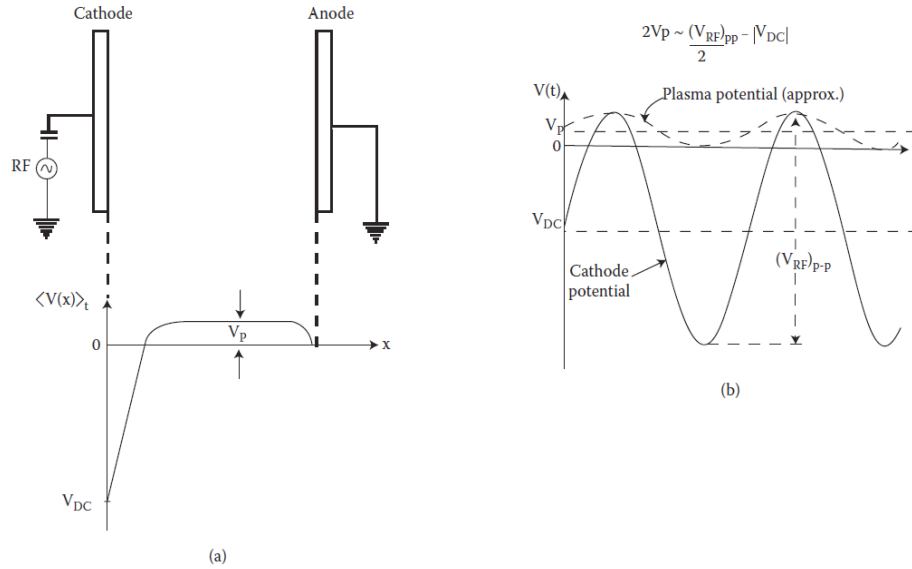


Figure 1.3 (a) Time-averaged potential distribution for RF system. (b) Potential distribution. [1]

### 1.3 Plasma Composition

Plasma is normally weakly ionized and the densities of species are depended on reaction conditions. Typically, electron density is in the order of  $10^9$ – $10^{12}$   $\text{cm}^{-3}$ , plasma ion density between  $10^9$ – $10^{12}$   $\text{cm}^{-3}$ , neutral species density around  $10^{15}$ – $10^{16}$   $\text{cm}^{-3}$ , and the ratio between ionized ions and neutral species is in the order of  $10^{-6}$ – $10^{-4}$   $\text{cm}^{-3}$ . In other words, there are millions more radicals than ionized species in the plasma, since it is easier to form neutral radicals, and a radical's lifetime is normally longer than an ion's. Even through both ions and radical etching substrates, most of the contribution is from highly reactive radicals, as the amount of radicals present is significantly higher than ions. Ions affect the reaction by physically bombarding the substrate surface and by increasing the directionality of the process.

The reaction chamber requires low pressure for plasma ionization and sustention. At higher pressure, the mean free path is very short, and it is difficult for electrons to achieve

energy higher than ionization potential before they collide with gas molecules. Only extremely high voltage may generate a high electric field and create an arc if it is higher than the breakdown voltage. Lightning at atmospheric pressure is shown in Figure 1.4. Breakdown voltage depends on the gas type, pressure, surface to volume ratio, and the distance between the electrodes. Paschen's law introduces more details that are not included in this dissertation.

[1]



Figure 1.4 Discharge in lightning [1]

#### 1.4 Etching Process Steps

The etching process consists of five major steps, as shown in Figure 1.5 shown [1]. (1) First, electrons are accelerated and the high-energy electrons collide with gas molecules. This collision process removes electrons from molecules and generates secondary electrons and ions. Meanwhile, the molecules can be broken down into neutral radicals with unsatisfied chemical bonds. (2) The ions and radicals diffuse to the space near the substrate, and then are accelerated by the bias voltage (ions) or by the energy transfer from the ions' bombardment

(neutral radicals). (3) The reaction species from the plasma are adsorbed on the sample surface and (4) react with the attached thin layer of the substrate top surface. This step is vital because most of the surface structures, such as undercutting, uniformity, aspect ratio, and selection of material can be determined by the reaction step. (5) Finally, the reaction products leave the substrate and diffuse into the plasma. If the products are not volatile, the reaction can be stopped. Re-deposition of products before diffusion to the plasma can introduce non-uniform process issues. Since the reaction is a combination of all five steps, the process speed is determined by the smallest rate.

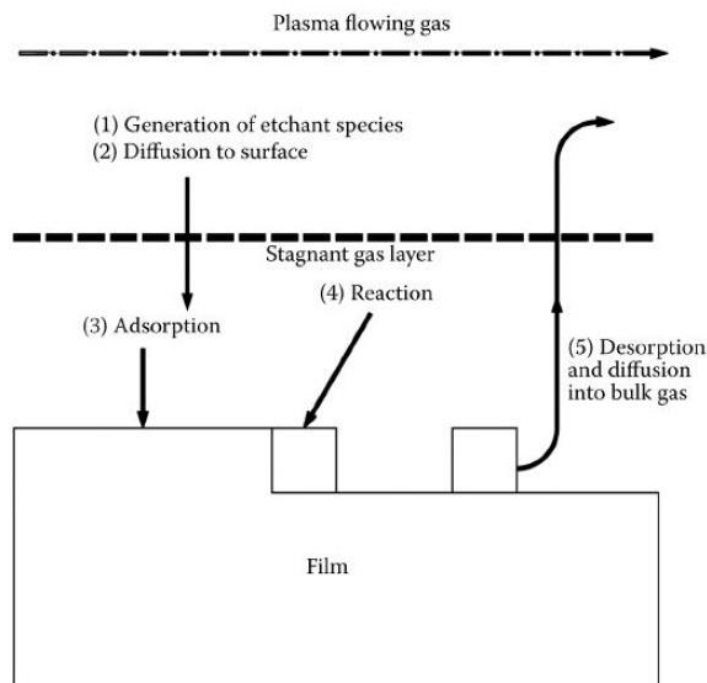


Figure 1.5 Major steps of plasma etching process. [1]

## CHAPTER 2 INDUCTIVELY COUPLED PLASMA REACTIVE ION ETCHING

Etching systems, such as reactive-ion etching (RIE), magnetron-ion etching (MIE), ion beam etching (IBE) and chemical-assisted ion beam etching (CAIBE) are routinely used in semiconductor or MEMS industries. For building high-aspect-ratio structures, a deep reactive ion etching technique is required. Until the 1990s, people faced at least three problems fabricating micro scales with high-aspect-ratio structures. [1] The first was the low etch rate: typical silicon etch rates require several hours to etch through a 550  $\mu\text{m}$  silicon wafer. The second was the micro loading effect. Ion and radical fluxes were reduced as aspect ratio increased, making it more difficult for them to diffuse to the bottom of the trench. Third, mask layers were often damaged during a long etch process. To address these issues, inductive coupled plasma reactive-ion etching, or ICP-RIE for short, is widely used for many applications today.

### 2.1 Advantages of ICP

In Chapter 1, we defined plasma as weakly ionized gas consisted of electrons, ions, radicals and gas molecules. To generate and sustain stable plasma, different approaches have been taken. Generally, the energy is transferred from an electromagnetic field to a low-pressure chamber filled with inert gas. Commonly used energy input methods for plasma generation include glow discharge plasma (GDP), capacitive coupled plasma (CCP) and inductively coupled plasma (ICP). [2]

Ideally, the etching process operates at high plasma density and low pressure. High plasma density increases the etching rate since more reactive species absorbed by the substrate. Low

pressure lengthens the mean free path for electrons and ions, increases anisotropy, and eases ionization for the gas molecules. However, typically, low pressure also means low plasma density since gas molecules density is reduced. The advantage of inductively coupled plasma (ICP) is the ability to generate high density plasma at lower pressure. The use of magnetic fields forces the electrons to travel a longer distance since they spin with a small gyroradius, increasing the chance that the electrons will collide with the molecules, ionize the gas and generate plasma. [1] Another advantage of ICP is the separate control of source power and bias power. The magnetic field controls the plasma ionization, determining the density of plasma and thus the etching rate of the process. The bias voltage controls the energy of the ions by different accelerating rates. High-speed ions bombard the substrate with higher energy, increasing anisotropy. For CCP, the electric field between anode and cathode are used for both plasma generation and ion acceleration, making it difficult to adjust the process parameters, which are coupled.

Some major types of ICP geometries include planar, cylindrical and half-toroidal, as shown in Figure 2.1 [3]. A more detailed structure for these cylindrical geometries, known as a helical resonator, is shown in Figure 2.2. Operated at the standard 13.56 MHz, a coil drives the plasma by coupling electrons to the RF magnetic field generated from the RF current. Electrons are forced to travel longer distances without colliding with the chamber wall, which increases the change of ionization at lower pressures, as previously described.

Using an ICP-RIE can increase the plasma etching rate due to high density plasma generated from the inductively coupled reactor. Klaassen et al. [4] successfully etched a 300  $\mu\text{m}$  deep trench in silicon at 5  $\mu\text{m}/\text{min}$  using a thin layer of photoresist around 6  $\mu\text{m}$  for protection.

The selectivity for the process is very good, about 50:1, since the ions' energy is kept at a lower value to reduce physical bombardment.

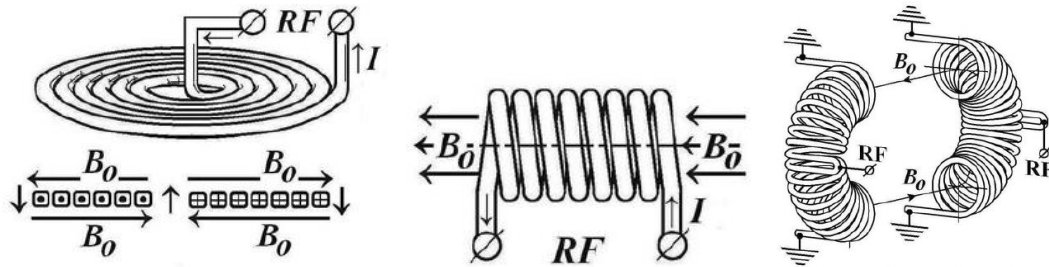


Figure 2.1 Major types of ICP geometries. [3]

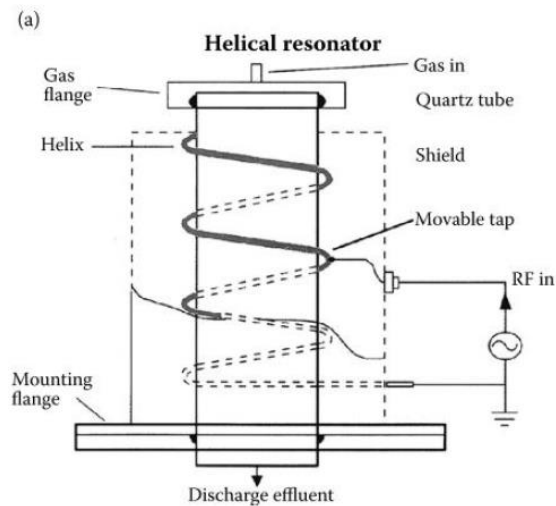


Figure 2.2 Cylindrical geometries. [3]

## 2.2 Major components of ICP system

Alcatel Vacuum Technology has supplied advanced plasma systems for more than 25 years. [8] Alcatel Model A601E is one of its classic ICP systems and delivers high density plasma ideal for deep reactive ion etching (DRIE). Since it is heavily used for the DRIE process implemented in the current research, understanding of this system is necessary for successful process development.

Similar to other common ICP systems, the Alcatel Model A601E consists of five major parts: a high density plasma source to generate active gas species, a bias power source to transport the active species to the surface, chambers with substrate holders, a high vacuum level pumping system, and a control system and GUI display. [9]

Images of the Alcatel Model A601E system from different sides showing some of its major components are given in reference paper. [10]

An inductively coupled plasma generator can provide up to 1800 W RF AC power supply. Substrate bias, as we mentioned before, is controlled separately and provided by the second RF power source with 200 volts maximum output. The system vacuum level is sustained by two paired pump systems. Each pumping system consists of a rough pump and a turbo pump. The rough pump provides a proper chamber pressure condition for turbo pump operating. High temperature sections of the system are cooled down by chiller water. The substrates holder temperature, also called reaction temperature, is controlled by a combination of liquid nitrogen and digital heater.

The load lock requires manual loading/unloading of a substrate. The following images show the load lock when not in use or open for loading.



Figure 2.3 Load lock. [11]

A robotic arm transfers the substrate into the reaction chamber. Unlike its counterpart in the load lock, the process chamber substrate holder consists of lifters, helium input port, a raised portion, and a clamp ring. The raised portion lifts the substrate and secures it with the mechanical ring clamp. Helium fills the space between the backside of the substrate and substrate holder to improve the thermal conductivity of the system, resulting in accurate temperature control of the reaction.

The substrate's backside needs to be cleaned before loading into the ICP system. Chemical residuals or surface scratches causing an uneven backside can lead to helium leakage, affecting the process of plasma flow. Even worse, any adhesive material on the backside can cause wafer drop during transfer.

After a substrate has been loaded into the load lock, all processing is controlled by a graphical user interface. If there is a safety hazard or serious system issue, an emergency machine off (EMO) button can be used to halt the entire process. [10]

### 2.3 Alcatel GUI and In Situ Monitoring

The control system provides video displays of the sensor and status information, process control information, and data input information through standard Alcatel GUI.

Each process is defined by a series of recipe steps, which can be customer designed and edited. The typical process starts from temperature control and stabilization steps, followed by selected etching or cleaning steps. As the process finishes, the system will automatically transfer the substrate and vent the chamber for unloading.

Monitoring the status of the system sensors and process parameters in real time not only helps to avoid fatal errors, but also provides more information for results analysis, benefit process development, and improvement. Detailed explanations for sensor displays and statuses can be found in the user manual [11]. However, some of the parameters requiring specific attention are introduced here since they may significantly affect the fabrication results:

1. *Source RF status displays* power delivered vs. power reflected. Ideally, the reflected power should be kept at zero, to ensure high efficiency energy transfer from the RF electric field to plasma output generation.
2. *Process chamber high vacuum sensor isolation valves and process chamber high vacuum sensor displays* indicate the vacuum condition of the process chamber in idle mode. This specific Alcatel model is capable of maintaining a low pressure environment at 2E-3mTorr level. For safety reasons, checking this system's base pressure before proceeding with any processes is necessary to ensure the pumping system is in proper working condition.

3. During the etching process, the high vacuum sensor display switches off, while the manometer sensor field displays process chamber pressure during process steps. The pressure or vacuum level depends on the experiment's parameters, especially the reaction gas flow rate. Typically, the DRIE etching process operates at a pressure level of a few mTorr. Lower pressure during the process may indicate the reaction gas source is running out and requires refilling.
4. The reaction chamber's pressure during the experiment can be controlled in two different ways: position control or flow rate control. By using the position control method, users control the reaction chamber's pressure during experiments by setting the position of the VAT (throttle valve) valve. Pumping speed reaches the maximum value when the VAT valve is set at 100%, or completely reduces to zero when the VAT valve is closed. On the other hand, the flow rate control method controls the pressure directly using a closed-loop control system. The signal from the manometer is used as system feedback to adjust the control parameters.
5. Reaction temperature control is achieved by applying both low temperature liquid nitrogen and a high temperature heater to the backside of the substrate. As mentioned before, helium is applied to fill the space between the backside of the substrate and the substrate holder to increase the thermal conductivity. The helium mass flow controller displays helium flow. Flow above 10 sccm indicates helium leakage, caused by substrate backside deformation or contamination, can significantly affect the uniformity of the experiment results.

## 2.4 Bosch process

Instead of a one-step plasma etching process, one widely used alternative to high-aspect-ratio silicon etching is called the “Bosch process”. Also known as pulsed or time-multiplexed etching, the Bosch process introduces a so-called blocking mechanism. It normally starts with a short-cycle etching process (no more than a few seconds), no different from ordinary isotropic plasma etching, with a polymer-based deposition layer introduced during the second pulse. The polymer covers the sidewall as well as the bottom of the trench to form a passivation layer a few nanometers thick. Then another etching process follows. This leads to anisotropic etching of the polymer as bias voltage accelerates the ions’ directionality. Ion bombardment mainly clears the polymer from horizontal surfaces, exposing the silicon substrate for the reaction radical chemical etching. The sidewall of the trench will be protected and the etch proceeds only in the vertical direction as Figure 2.4 shows. Passivation gases such as  $C_4F_8$ ,  $BCl_3$  and  $CF_2Cl_2$  are used as sources of a protection layer.

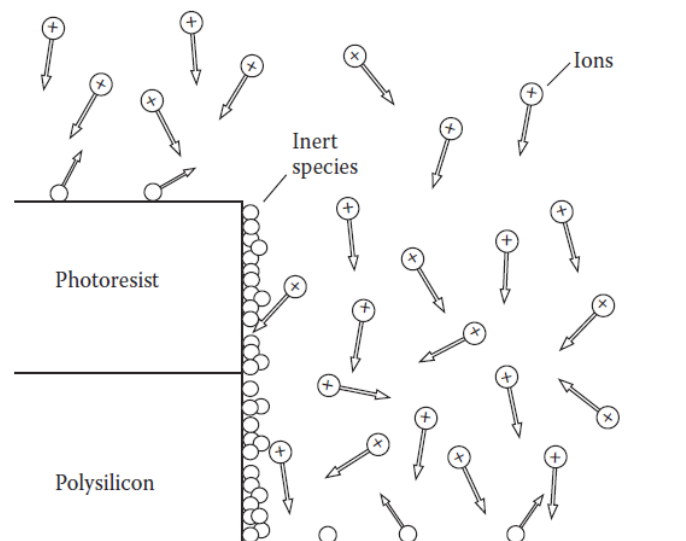


Figure 2.4 Blocking mechanism. [1]

An example of the etching process is introduced here to better understand the blocking mechanism. Manos et al. [1] discussed trench profile manipulation by introducing hydrogen to plasma as shown in Figure 2.5. The top image shows the etching rate varies with concentration changes of applied hydrogen. If hydrogen is added to  $CF_4$ , the fluorine-to-carbon ratio is reduced. Polymerization pulse introduces a thicker passivation layer. A higher ratio of etching gas is consumed to remove the polymer from the bottom of the trench, causing the etching rate to be reduced. When the ratio reaches a certain value, the etching rate decreases to zero. It also compares reactions proceeding at two different bias voltages. Ions have higher energy bias voltage is applied, increasing bombardment efficiency and etching speed.

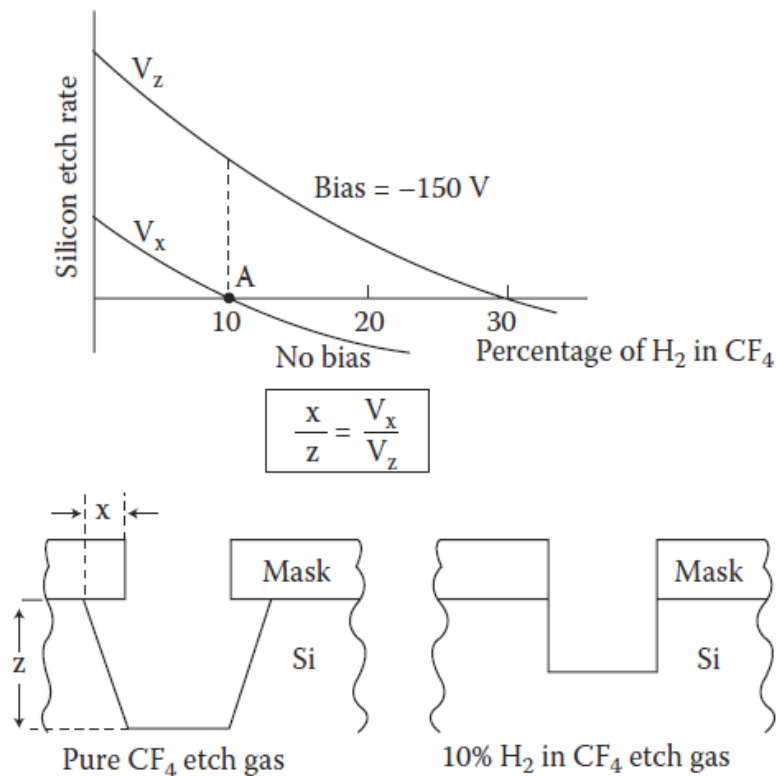


Figure 2.5 Trench profile change with the fluorine-to-carbon ratio [1]

Other materials may require different types of plasma based on the chemical reaction requirements. Take aluminum etching as an example. Fluorine-based plasma is not working since the aluminum fluoride is involatile. The reaction products cover and prevent the substrate from further etching. Chlorine-based gas, such as  $\text{CCl}_4$  and  $\text{Cl}_2$ , are good alternative gas sources for aluminum, which can afford high-aspect-ratio and near vertical sidewall profile.

The Bosch process typically can achieve aspect ratios of 20–30:1 if the micro loading effect is not dominant, and etching rates of higher than  $10 \mu\text{m}/\text{min}$  are standard for MEMS and semiconductor industries. As referenced, in a Plasma-Therm high-density system, some typical etching characteristics are listed in Table 2.1 for a two-pulse process switches alternatively between passivation and etching. By etching from both sides of the wafer, the aspect ratios can be further improved. Chow et al. etch through a  $400 \mu\text{m}$  wafer with  $10 \mu\text{m}$  opening holes. [13]

Table 2.1 Typical etching characteristics. [1]

$\text{SF}_6$ flow	30–150 sccm
$\text{C}_4\text{F}_8$ flow	20–100 sccm
Etch cycle	5–15 s
Deposition cycle	5–12 s
Pressure	0.25–10 Pa
Temperature	20–80°C
Etch rate	1.5–4 $\mu\text{m}/\text{min}$
Sidewall angle	$90^\circ \pm 2^\circ$
Selectivity to photoresist	~100 to 1
Selectivity to $\text{SiO}_2$	~200 to 1

## 2.5 Advanced Bosch process

High-aspect-ratio deep reactive ion etching (DRIE) using the Bosch process is very successful in enabling vertical trenches with aspect ratios as high as 20:1. However, as an aspect ratio further increases, the micro loading effect dominates the profile, especially for etching small features. Recent work to improve etching profiles has demonstrated that insufficient removal of passivation residue is the major reason for tapered profile sidewall. [5] To resolve this problem, Reza et al. [6] introduced a method to remove the polymer by applying an additional depassivation pulse in between the passivation pulse and etching pulse. This modification enables separate parameter control of depassivation and substrate etching, resulting in better sidewall profiles and higher aspect ratios.

The basic Bosch process consists of two separate steps, etching and passivation. A commonly used gas combination is  $\text{SF}_6$  and  $\text{C}_4\text{F}_8$ .  $\text{SF}_6$  is the source of high reactive fluorine radicals, used for the etching process, while the  $\text{C}_4\text{F}_8$  introduces a carbon-based passivation layer for sidewall protection, shown in Figure 2.6. During the etching process, the initial portion of  $\text{SF}_6$  flux is dedicated to removing the passivation layer from the bottom of the trench and exposing the silicon to fluorine radicals. For a basic Bosch process, the parameters for the etching process are constant for both depassivation part and etching. As the aspect ratio increases, ion flux is reduced at the bottom, since ions require higher energy to travel through the trench vertically without being absorbed by the sidewall. The ions' energy depends on the bias voltage at the ICP system. Increasing bias voltage during the etching process results in an

electric field near the cathode. The ions diffused to the cathode black space are accelerated to higher speed with higher energy. However, this approach may also increase the number of scattered ions due to high-energy ion bombardment, leading to sidewall damage and undercutting.

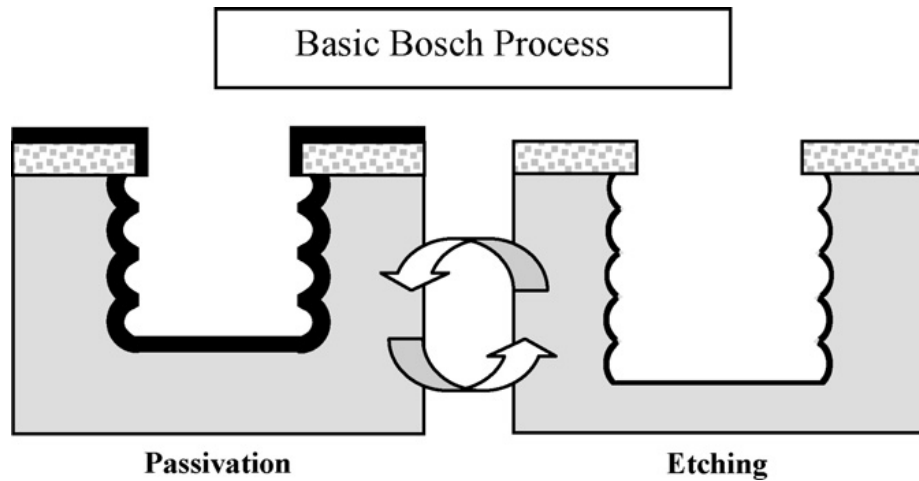


Figure 2.6 Basic Bosch process. [5]

To the extent the aspect ratio limitation without sidewall profile quality compromise, independent control of depassivation and etching is necessary. Modified Bosch process with separate pulse for depassivation or so-called three-pulse Bosch process is developed on a Plasma-Therm ICP system. [6]

The depassivation gas could be  $\text{SF}_6$ , argon, and oxygen. All the parameters are shown in Table 2.2. Pulse duration, gas flow rate, pressure, bias voltage, and coil power are kept constant for better understanding the effect of gas type. SEM images in Figure 2.7a and Figure 2.7b show an etched trench using  $\text{SF}_6$  and oxygen, respectively, as a depassivation gas. In the initial experiment, the bias voltage was set to be 50 V for  $\text{SF}_6$  depassivation. In the other experiment,

the bias was set to be 30 V and passivation time was increased to 8 s. Both images show successful fabrication of high-aspect-ratio features as high as 30:1.

Table 2.2 Three-pulse Bosch process [6]

Step/parameter	Period (s)	Gas flow (sccm)	Pressure (mTorr)	Bias voltage (V)	Coil power (W)
Passivation	5	C <sub>4</sub> F <sub>8</sub> (70), Ar (40)	15	0	800
Depassivation	3	Variable	15	Variable	800
Etching	4	SF <sub>6</sub> (75)	16	42	800

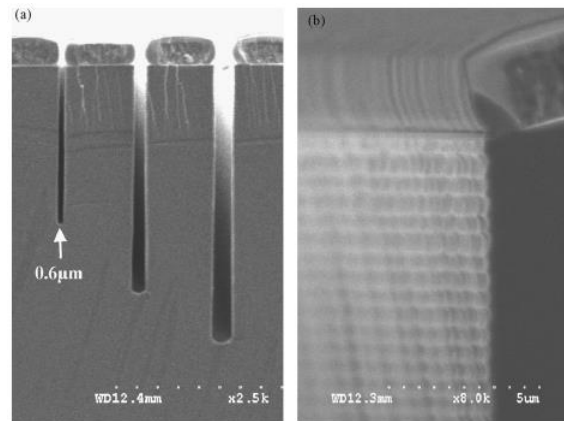


Figure 2.7a Profile and sidewall using SF<sub>6</sub> as the depassivation gas. [6]

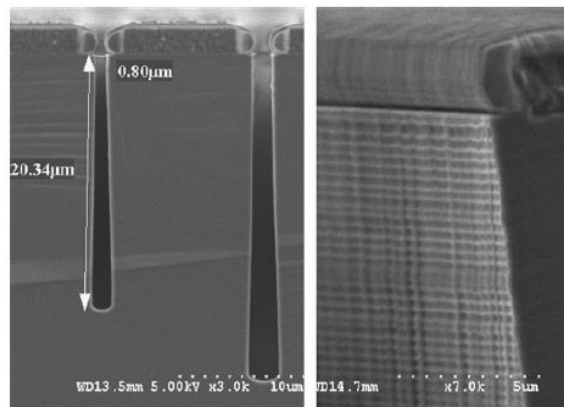


Figure 2.7b Profile and sidewall using oxygen as the depassivation gas. [6]

To further improve the profile and aspect ratio, an argon-based DRIE recipe was developed. Argon has the highest vertical-to-horizontal etching ratio among several commonly used chemicals. [7] Since argon is chemically inactive, argon depassivation is a pure physical process by sputtering passivation polymer away from the bottom of the trench. Compared with the chemical etching process, physical bombardment is more anisotropic and far slower, resulting in a better sidewall profile and improved process stability. However, the sputtered polymer material could re-deposit on the substrate or sidewall, introducing non-uniform trench profiles or causing black silicon issues. The four-pulse argon-based recipe provides a solution for this problem. After each cycle, a short oxygen pulse is applied to remove re-deposited polymer particles. Typical fabricated results are shown in Figure 2.8. The aspect ratio is further increased and the trench shows a smooth sidewall profile without scalloping or striation.

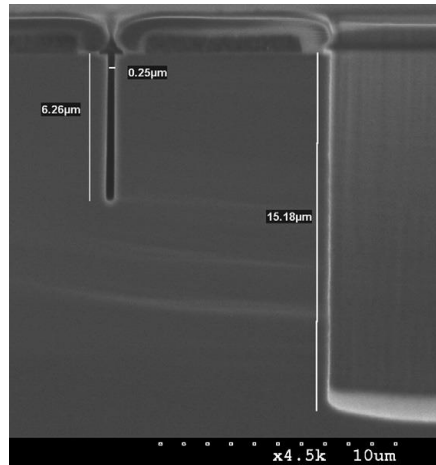


Figure 2.8 Profiles etched using the four-pulse argon-based recipe.[1]

## CHAPTER 3 CHARACTERIZATION OF THE SILICON NANOPILLAR-SURFACE FILLED WITH NANOMATERIALS

Modified from a paper published in *Materials Research Express*

Yuan He, Xiangchen Che and Long Que

### 3.1 Introduction to Nanopillar-surface Filled With Nanomaterials

In the past decades, nanopillars have been fabricated from different materials [13, 14], using either a bottom-up approach or a top-down approach [15, 16]. For the bottom-up approach, the nanopillars are usually grown by a vapor-liquid-solid method using metal catalysts [15]; for the top-down approach, the nanopillars are typically fabricated using nanolithography (i.e., electron-beam lithography). Electron-beam lithography can draw custom patterns with 10 nm resolution; nanosphere lithography (NSL), followed by a dry etching process [16, 17] can also be used for top-down, high-density nanopillar formation. In this chapter, a NSL-based silicon nanopillar-surface fabrication process will be used. These fabricated nanopillars will be filled and grafted with nanomaterial to form an antireflection surface as a demonstration of one potential application for this unique nanostructure.

Nanopillars have been utilized for various applications. Silicon-based nanopillars, mimicking moth-eyes [15, 20, 21], are a commonly-used technical platform, demonstrated as an efficient antireflective surface in solar cells. It has been demonstrated that reflectance can be as low as 0.5% from a silicon nanopillar-surface over a range of spectra from 550 nm to 870 nm [20]. How to further reduce or tailor Si nanopillar-surface reflectance across a broad spectral range is still a very important research topic, and particularly critical for further

enhancement of the conversion efficiency of silicon solar cells. Ideally, this type of nanopillar surface can offer zero reflectance across a broad spectral range of sunlight. As a result, all the incoming photons can be trapped by the nanopillar's surface and consequently be converted into electricity. It has been found that the material type, the diameter, and the length of nanopillars, as well as the spacing between them, are the main parameters to affect reflectance and photon trapping [15]. These parameters can be modified to tailor the absorption spectrum.

When the reflectance of a Si nanopillar surface reaches a certain level, nanopillar parameter optimization reaches its limit and cannot further increase optical absorption. As previously mentioned, the reflectance of an optimized Si nanopillar surface can be as low as 0.5% [20], but cannot continue to decrease to zero solely through optimizing the parameters of the nanopillar surface. Hence, once the optimization of these parameters is complete, new approaches are required if the photon trapping by the nanopillar surface needs further improvement. One approach is modification of the material composition of the nanopillar surface.

A Si nanopillar surface consists of two materials: arrayed Si nanopillars and the air surrounding them. Air is not a good medium for absorbing and trapping photons. Hence, the air should be replaced by another material in order to achieve improved performance. It has been found that some nanomaterials can absorb photons at significant rates [22–28], and the absorption capability of the nanomaterials can be tuned by changing their size, shape, and composition [22–28]. Therefore, it is possible that optical absorption or photon trapping can be further improved by replacing the air among the nanopillars with nanomaterials.

To this end, one simple and straightforward approach is to attach and/or add some nanomaterials directly to the nanopillar surface so that the air among nanopillars can be filled with nanomaterials; alternatively, the nanopillars can also be grafted with nanomaterials. In the present research, a Si nanopillar surface grafted with different nanomaterials has been fabricated and its properties have been studied. In this effort, the Si nanopillar-surface is not optimized for lowest reflectance; instead, the main focus is to demonstrate that the nanomaterials grafted with the Si nanopillar surface can improve its optical trapping compared to an identical bare Si nanopillar-surface. Specifically, two types of nanomaterials, CuS–Au core-shell nanostructures and silver nanoplates, are each used separately to replace the air in the nanopillar surface as technical demonstrations. It is anticipated that other types of nanomaterials can also be used to replace the air for enhancing optical absorption across a specific wavelength range.

## 3.2 Experimental details

### 3.2.1 Chemicals and materials

Polystyrene nanosphere beads of different sizes (500 nm, 1000 nm, 3000 nm) were purchased from Fisher Scientific Inc. Triton X-100 and methanol were both purchased from Sigma-Aldrich Inc. Deionized (DI) water was obtained from a DI water purification system (Millipore, FRANCE). Silicon wafers were obtained from Ultrasil Corp. Chemicals for surface cleaning and treatment including acetone, IPA, 98% sulfuric acid and 30% hydrogen peroxide were all obtained from Sigma-Aldrich Inc. The CuS–Au core-shell nanostructures (CuS–Au NSs) were synthesized as described in [29]. Silver nanoplates (Ag NPs) (diameter 150 nm) were purchased from nanoComposix, Inc.

### 3.2.2 Fabrication of silicon nanopillar-surface filled and grafted with nanomaterials

First, 4 inch silicon wafers are cut into 2 cm× 2 cm pieces. Then each piece is cleaned by acetone, IPA, DI water, with the help of ultrasonication for 20 mins in each solution in sequence. Then the silicon pieces are immersed into a fresh piranha solution (a mixture of sulfuric acid and hydrogen peroxide (3:1)) in a beaker, which is kept on a hot plate at 60 °C for half an hour. Thereafter the silicon pieces are taken out from the beaker and rinsed thoroughly by DI water. After the surface treatment, the silicon pieces can be used immediately; otherwise, they should be stored in DI water to avoid formation of native oxide for future use.

At this point, the polystyrene (PS) beads are dispersed uniformly in a solution containing Triton X-100 and methanol (1:400). Then a certain amount of the PS-bead solution is directly applied to each silicon piece by a micropipette. The solution is left to dry without any disturbance at room temperature for several hours. As shown in Figure 3.1, the PS nanosphere beads are self-assembled into a close-packed monolayer. The beads are then tailored by oxygen plasma to shrink their size. Specifically, 500 nm nanospheres are etched by reactive ion etching (RIE) at 60W and 50 sccm for 90 s, while 1000 nm and 3000 nm nanospheres are etched under the same conditions for 240 s and 600 s, respectively.

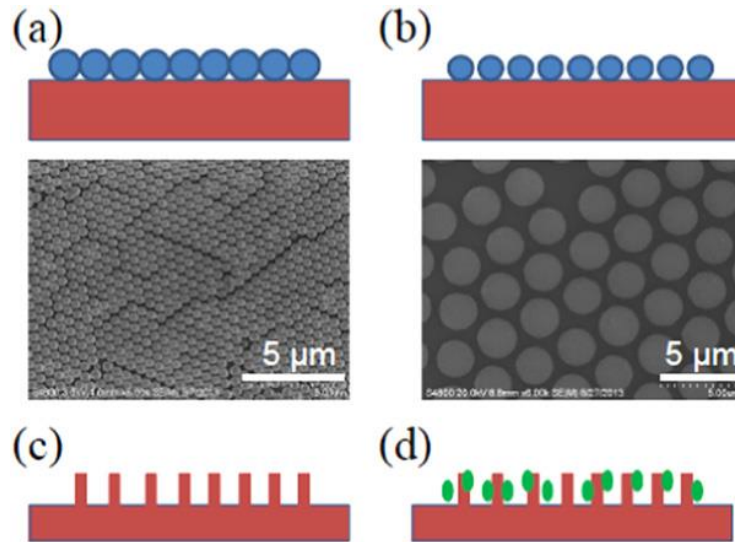


Figure 3.1. Process flow to fabricate the silicon nanopillar surface: (a) a self-assembled monolayer (SAM) of PS nanosphere beads formed on silicon substrate; (b) the size of the PS nanosphere beads is shrunk by a RIE process; (c) an ICP is carried out to form silicon nanopillars, followed by removing the remaining PS nanosphere beads; (d) nanomaterial solution is applied by dropper on the nanopillar surface.

Using the PS nanosphere beads as the mask, an inductively coupled plasma (ICP) Bosch process is applied for etching the unprotected silicon and forming the nanopillar structures. In this process, alternate cycles of etching in a flow of SF<sub>6</sub> (75 sccm, 3 s) and passivation in a flow of C<sub>4</sub>F<sub>8</sub> (60 sccm, 3 s) are used. The plasma is generated with an RF power of 800W and a platen power of 50 W. The temperature is kept at 20 °C by a stream of nitrogen gas. Nanopillar height can be controlled by adjusting the number of process cycles. In a typical experiment, the height of nanopillars is approximately 1 μm for a 3 min ICP process (30 cycles) using 1000 nm beads as the mask.

After the etching process, the samples are treated with oxygen plasma to remove the residual beads and improve the wetting performance. Then the nanomaterial solutions are deposited on the silicon nanopillar surface using a micropipette. In order to produce a uniform

deposit, the nanomaterial solution is ultrasonically stirred for a couple of hours, allowing the nanomaterials to be dispersed uniformly into the solution. After the nanomaterial solution coating is administered by a dropper, the silicon nanopillar surface is left to dry at room temperature.

### 3.2.3 Characterization

The solution of CuS–Au NSs or Ag NPs is used to fill and coat the silicon nanopillar surface. As mentioned, the silicon nanopillar surface can be rendered hydrophilic by carrying out oxygen plasma treatment and a piranha bath. Then the nanomaterial solution is applied on the surface. All the optical measurements are taken after the solution on the surface has dried. The detailed optical setup is illustrated in Section 3.

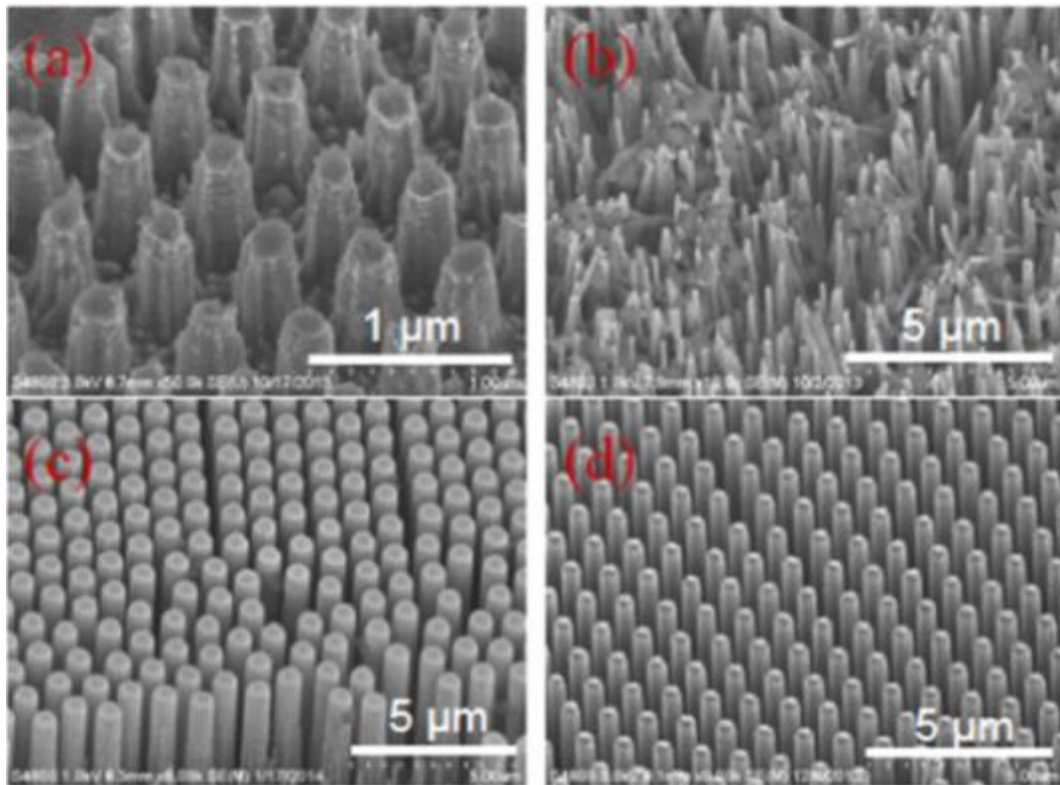
The reflectance of the nanomaterial-coated nanopillar surface is measured using an Ocean Optics USB4000 Spectrometer. The optical source is a tungsten halogen source (Ocean Optics, Inc.). The spectrometer is USB4000-VIS-NIR (Ocean Optics, Inc.), which can measure the spectrum from 350 nm to 1050 nm. The contact angle of the nanomaterial solution on the silicon nanopillar surface is measured using a Contact Angle System OCA (Dataphysics, Inc.). The surface morphology of the samples is characterized by a scanning electron microscopy (SEM, HITACHI S-4800). To analyze the antireflection properties at different incident angles, light reflection intensity at 0, 20, 30, 40, 50, 60 degree is recorded.

Each experiment discussed below has been performed at least three times to eliminate random errors. In order to obtain accurate results, reflectance measurements from bare flat silicon pieces were also taken at each incident angle as reference points.

### 3.3 Results and Discussion

#### 3.3.1 Fabricated Arrayed Nanopillars

Some representative SEM images of the fabricated Si nanopillars are given in Figure 3.2. In Figures 2(a) and (b), the nanopillars are fabricated using  $0.5\ \mu\text{m}$  beads as the mask. The size of the beads has shrunk to  $150\ \text{nm}$ ; at this size ICP etching was performed to form the beads into nanopillars. As a result, the typical diameter of the resulting nanopillars is  $100\text{--}150\ \text{nm}$  as shown in Figure 3.2(a). On the other hand, the nanopillars can collapse (Figure 3.2(b)) if the sidewalls of the nanopillars are over-etched. Hence, in order to obtain robust arrayed nanopillars, the lateral etching of the nanopillars should be minimized. This can be achieved by increasing the time of the depositing cycles during an ICP process.



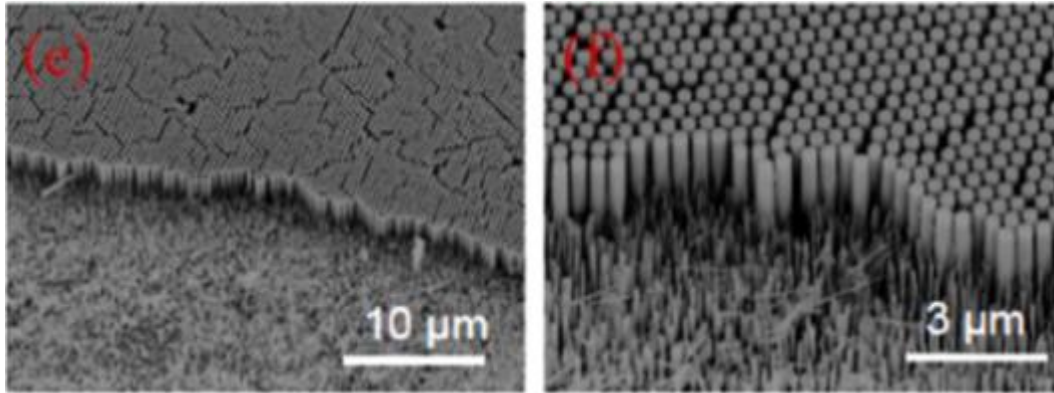


Figure 3.2. SEM images: Nanopillars fabricated by the nanosphere lithography (NSL) process using 500 nm beads [(a)–(b)]; 1000 nm beads [(c)–(d)]; 3000 nm beads[(e)–(f)].

When the bead size increases to 1  $\mu\text{m}$  or 3 $\mu\text{m}$ , after shrinking the size of the beads to 500 nm as the mask, the typical diameter of the nanopillars is in the range of 400 nm to 500 nm.

The resulting arrayed nanopillars are very robust, and few collapses have been observed as shown in Figures 3.2(c)–(f). The height of the nanopillars can be readily made as tall as 5–10  $\mu\text{m}$ . Usually, for the same height of the nanopillars, increasing the diameter of the nanopillars lowers the possibility of the collapse of the nanopillars. However, it has been found that very few nanopillars collapse even when their height-to-width ratio (HWR) is up to 20:1. In addition, the gap/space area among nanopillars can also be readily modified by reducing the size of the beads during the RIE etching step, shown in Figure 3.1(b). For instance, using the same beads as the mask, in Figures 2(c) and (d), the gaps among nanopillars can be easily changed from 250 nm to 500 nm, respectively.

### 3.3.2 Contact angle measurements and surface topology of the nanopillar surface

The hydrophobicity of the surface of the nanopillars is a very important characteristic. Ideally the nanopillars surface should be hydrophilic, in order to efficiently add solution-based nanomaterials and ensure they either coat the nanopillars or fill the spaces between them. It

has been found that a freshly fabricated nanopillar-surface always has some degree of hydrophobicity. The typical contact angle for this type of surface is 43 degrees, as shown in Figure 3.3(a). After oxygen plasma treatment and an ultrasonic wash in piranha solution, sample surfaces are rendered hydrophilic with a contact angle close to 16 degrees (Figure 3.3(b)). As a result, the nanomaterials in the solution can coat the nanopillars and fill the space among them very efficiently. The surface topology of the samples has been examined, and some SEM images are shown in Figures 3(c) and (d), before and after the nanomaterials have been applied. By adding the nanomaterial solution by dropper, the nanomaterials can uniformly coat the nanopillar surface and fill the spaces between them (upper left in Figure 3.3(d)).

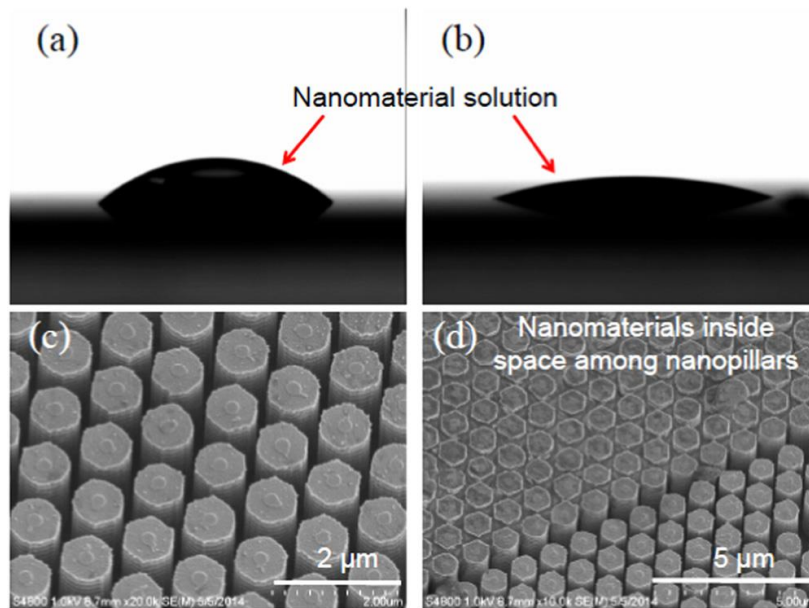


Figure 3.3. (a) Contact angle is  $42^\circ$  for nanomaterial solution on a fresh silicon nanopillar surface; (b) contact angle is  $16^\circ$  for silicon nanopillar surface after treatment; (c) SEM image of a fresh silicon nanopillar surface: air gaps among nanopillars; (d) SEM showing the air gap filled with nanomaterials in the upper portion of the nanopillar surface.

In contrast, it has been observed that aggregations of nanomaterials can be formed the tops of nanopillars if the surface is hydrophobic. In this case, the dried nanomaterials usually

are not uniformly distributed across the nanopillar surface and therefore cannot fill the space among them. Instead, some circular thin-layer strips of nanomaterial are formed. This is because the solution droplets cannot collapse and cover the hydrophobic surface uniformly. The nanomaterials inside the droplets tend to aggregate to the periphery of each droplet. After the droplets dry, the aggregated nanomaterials form circular strips on the surface, causing a lack of uniformity in the coating. This non-uniform coating is anticipated to affect the optical properties of the samples.

### **3.3.3 Reflectance from surface with and without nanopillars**

For comparison, two types of samples have been prepared. One sample (S1) is a flat silicon surface coated with CuS–Au NSs. The other sample (S2) is a silicon nanopillar surface filled and/or grafted with CuS–Au NSs. The average height of the nanopillars is 500 nm. For both samples, varying amounts (i.e., 4  $\mu\text{L}$ ) of nanomaterial solutions have been coated on their surfaces. The measurement process is shown in Figure 3.4(a), which is used to measure reflectance when the light is incident on the surface of the sample at a perpendicular angle. The optical fiber probe for the measurement is the Fiber Optic Reflection/Backscattering Probe (Ocean Optics, Inc.). This probe consists of a tight bundle of 7 optical fibers in a stainless steel ferrule with 6 illumination fibers around 1 read fiber. Specifically, for the reflectance measurement, the optical fiber probe delivers the optical light perpendicular to the surface of the sample, and at the same time the probe collects the reflected optical light from the sample surface, leading to a spectrometer.

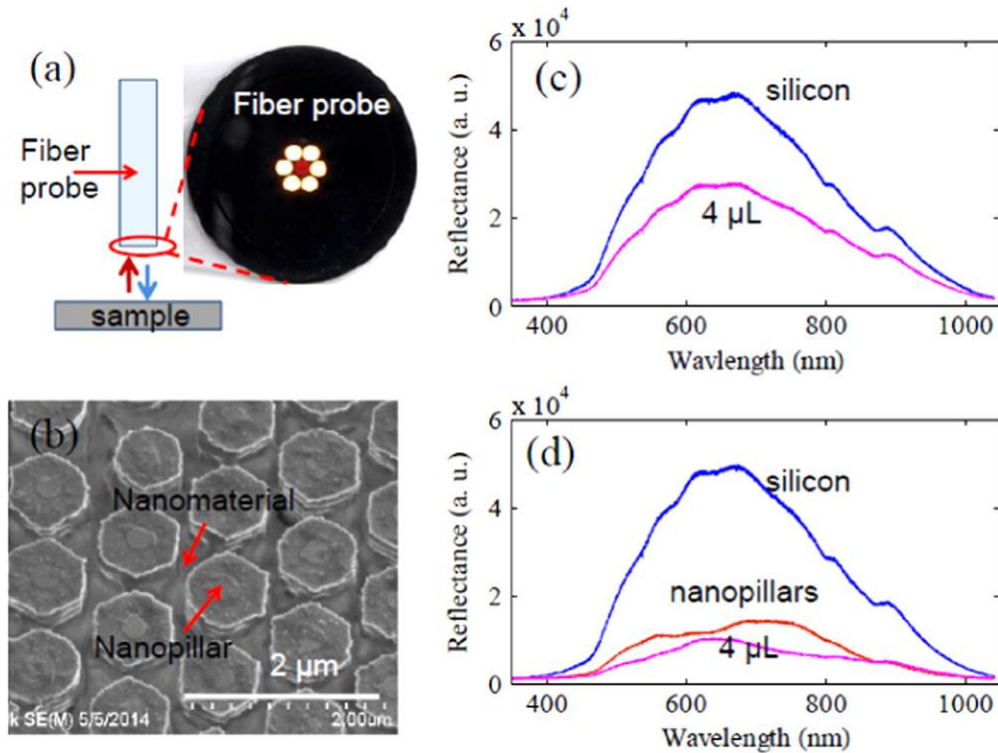


Figure 3.4. (a) Process for the normal reflectance measurement; (b) close-up image showing nanopillar surface filled/grafted with nanomaterials in the air gap; (c) reflectance from a flat silicon surface and a surface coated with 4  $\mu\text{L}$  CuS–Au NSs, respectively; (d) reflectance from a flat silicon surface; a Si nanopillar surface and a nanopillar surface coated with 4  $\mu\text{L}$  CuS–Au NSs.

A close-up SEM image showing the nanomaterial-filled nanopillar surface is given in Figure 3.4(b). The reflectance is shown in Figure 3.4(c) from Sample S1 coated with 4  $\mu\text{L}$  of nanomaterial solution. It has been found that reflectance decreases compared to that from a bare flat silicon surface. The reflectance from Sample S2 is shown in Figure 3.4(d). As shown, the reflectance from the bare nanopillar surface is reduced significantly compared to that from a flat silicon surface. Upon coating nanomaterials, reflectance can be further reduced. For instance, after being coated with 4  $\mu\text{L}$  nanomaterial solution, reflectance reduction is 20% on average. Experiments also find that by coating 8  $\mu\text{L}$  nanomaterial solution, reflectance

reduction is 50%. It should be noted that by optimizing the nanopillar alone, the reflectance from an optimum nanopillar surface can be as low as 0.5% compared to that of a flat silicon surface [20]. Since the proper coating of the nanomaterials to the nanopillar surface can further reduce the reflectance, it might be possible to render a reflectance approaching zero through optimization of the nanopillar surface and the addition of a coated nanomaterial.

### **3.3.4 Reflectance measurements under different incident angles**

The measured reflectance under normal conditions on the nanopillar surface filled/grafted with different amounts of CuS–Au NSs is given in Figure 3.5(a). The height of the nanopillars is 500 nm on average. All the measurements are normalized to the reflectance from a bare nanopillar surface. As shown, the reflectance always decreases across a spectrum from 350 nm to 1050 nm, which is the detection range of the spectrometer used in the current experiments, by increasing the amount of the CuS–Au NSs solution. When 8  $\mu\text{L}$  of CuS–Au NSs solution coats the nanopillar surface, reflectance reduction can be more than 50% compared to a bare nanopillar surface.

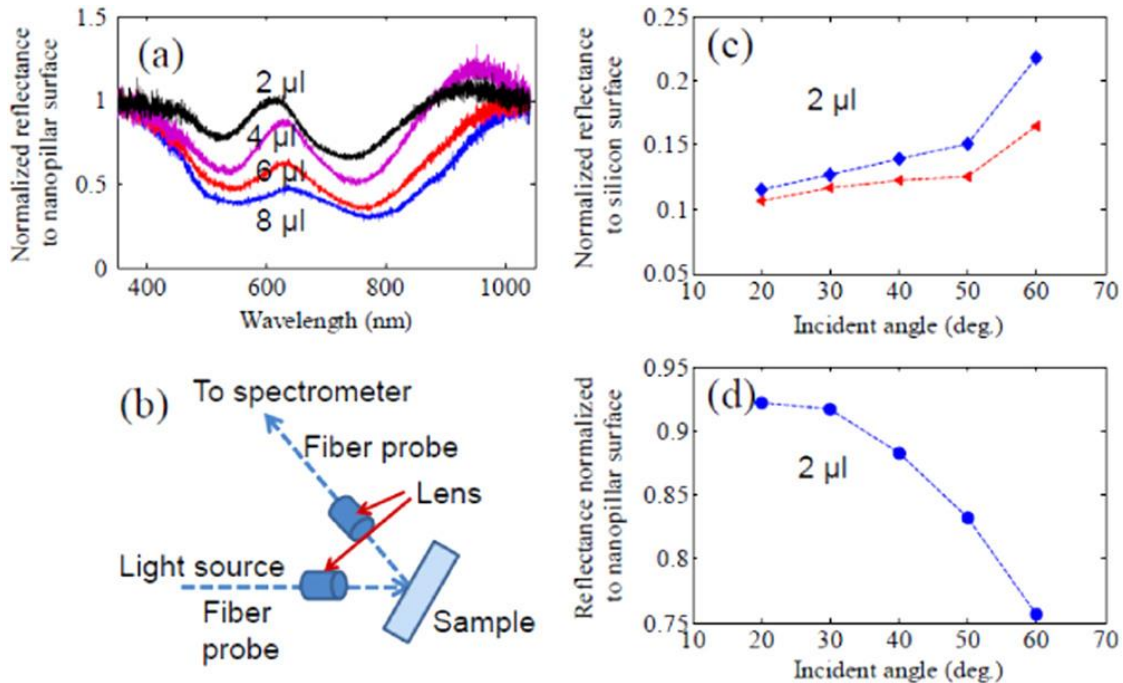


Figure 3.5. (a) Normal reflectance from Si nanopillar surface coated with 2  $\mu\text{L}$ , 4  $\mu\text{L}$ , 6  $\mu\text{L}$  and 8  $\mu\text{L}$  CuS–Au NSs, respectively; (b) process for measuring angled reflectance from the samples; (c) measured reflectance from a Si nanopillar surface (blue line), and a nanopillar surface coated with 2  $\mu\text{L}$  CuS–Au NSs (red line) at different incident angles. The reflectance is normalized to the reflectance from a flat silicon surface; (d) measured reflectance from a nanopillar surface coated with 2  $\mu\text{L}$  CuS–Au NSs, normalized to the reflectance from a bare nanopillar surface at different incident angles, respectively.

The process for reflectance measurement from other incidence angles on the sample is shown in Figure 3.5(b). The incident angle from the optical fiber to the samples is tuned from 20 degrees to 60 degrees, and corresponding adjustments are made to the receiving angle of the other optical fiber. As an example, the measured average reflectance results across the spectrum for the sample with 500 nm high nanopillars are given in Figure 3.5(c), which are normalized to that from a flat bare silicon surface. In this case, the amount of the applied CuS–Au NSs is 2  $\mu\text{L}$ . It has been found that reflectance is highly related to the incident angle for both the bare nanopillar surface and the nanopillar surface coated with CuS–Au NSs. Specifically, the

smaller the incident angle, the lower reflectance from the sample, thus the larger the amount of trapped photons by the sample. For the nanomaterial coated nanopillar surface, reflectance reduction under normal incidence (0 degree incident angle) is the largest compared to the bare silicon surface; this is due to the fact that the photons can enter and penetrate deep into nanomaterials filling the space among the nanopillars, and thus cannot easily escape [21]. The reflectance from the nanomaterial coated nanopillar surface normalized to that from a bare nanopillar surface is shown in Figure 3.5(d).

### **3.3.5 Reflectance measurements of the nanopillar surface filled and grafted with different nanomaterials**

The reflectance of the nanopillar surface filled and grafted with different nanomaterials has also been studied. In these experiments, the average height of the nanopillars is 1500 nm. The CuS–Au NSs and Ag NPs have been coated on the nanopillar surface, respectively.

The measured reflectance from the CuS–Au NSs coated nanopillar-surface is given in Figure 3.6(a). As expected, reflectance decreases with an increased amount of CuS–Au NSs. The reflectance can be reduced more than 50% compared to a bare nanopillar surface. It has also been observed that the overall average reduction in reflectance for nanopillar samples of different heights changes when the same amount of nanomaterials is coated on the nanopillar surface. In contrast, there is a distinct difference in the reflectance profile between a 1500 nm-high nanopillar surface (figure 3.6) and a 500 nm-high nanopillar surface (figure 3.5(a)).

Specifically, the reflectance profile for 1500 nm-high nanopillar surface shows little fluctuations compared to that for the 500 nm-high nanopillar surface across the measured spectrum from 350 nm to 1050 nm. Measurements on several samples of 500 nm-high

nanopillar surfaces show consistent large fluctuations in reflectance across the aforementioned spectral range. This is due to the reflectance fluctuations of the bare nanopillar surface of this type. In contrast, the reflectance from a bare 1500 nm-high nanopillar surface has small fluctuations, resulting in small fluctuations of the reflectance after being coated with nanomaterials. The uniform reduction of the reflectance across the spectrum indicates that the taller nanopillars can achieve more uniform photon trapping of different wavelengths, thereby benefiting solar energy harvesting.

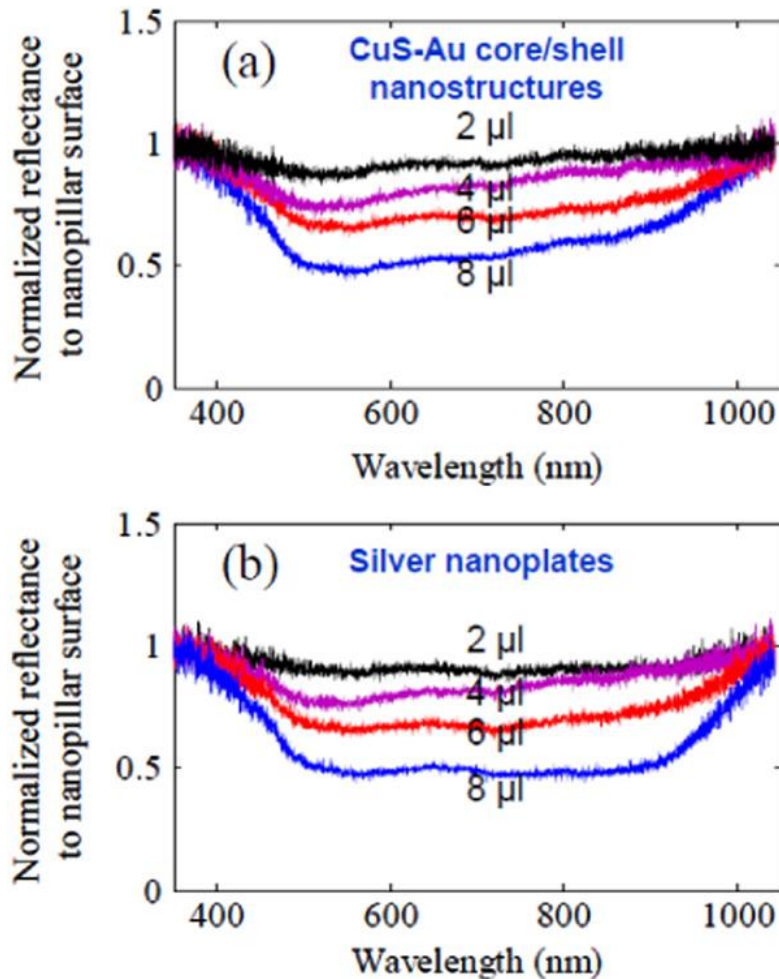


Figure 3.6. Measured normal reflectance from 1500 nm Si nanopillar surface. The reflectance is normalized to that from a bare Si nanopillar surface: (a) Si nanopillar surface coated with 2  $\mu\text{L}$ , 4  $\mu\text{L}$ , 6  $\mu\text{L}$ , 8  $\mu\text{L}$  CuS-Au NSs, respectively; (b) Si nanopillar surface coated with 2  $\mu\text{L}$ , 4  $\mu\text{L}$ , 6  $\mu\text{L}$ , 8  $\mu\text{L}$  Ag NPs, respectively.

The measured reflectance from the Ag NPs coated nanopillar surface is given in Figure 3.6(b). Again, the overall trend in the reflectance is similar to that of the CuS–Au NSs coated surface. But its reflectance profile has some difference, which is particularly clear when the amount of the Ag NPs increases. For instance, when 8  $\mu\text{L}$  of Ag NPs solution is applied and coated on the sample, the reflectance across the spectrum from 700 nm to 900 nm becomes smaller than that from the CuS–Au NSs coated sample, which is due to the increased optical absorption of the Ag NPs in this spectral range [30]. As a result, the improved optical absorption uniformity across the spectrum from 450 nm to 900 nm is achieved for the Ag NPs coated nanopillar surface. This observation suggests the possibility of reducing the reflectance from the nanopillar surface in a different spectral range by simply applying different types of nanomaterials. This characteristic could provide an ideal technical basis for a “smart” window by fabricating a nanomaterial-filled nanopillar surface on a transparent substrate (e.g., glass substrate). This type of window could be used as an efficient light absorber for solar energy harvesting while selectively changing the light transmission [31].

### 3.4 Conclusion

In this chapter, a Si nanopillar surface filled and grafted with nanomaterials was fabricated, and its optical absorption was characterized. The nanomaterials can fill the air gap among nanopillars and coat the nanopillar surface uniformly after the nanopillar-surface was rendered hydrophilic. By replacing the air with nanomaterials among the nanopillars, the reflectance from the nanopillar surface can be reduced by over 50% compared to that from a bare nanopillar surface. Using different nanomaterials, the absorption of the optical spectrum can be modified, offering a simple technique to tune the absorption of photons of different

wavelengths. This type of nanopillar surface could be very useful for increasing photon capturing, tuning and expanding the optical absorption spectral range of photons, thereby benefiting solar energy harvesting technology.

## CHAPTER 4 SURFACE ENHANCED RAMAN SPECTROSCOPY (SERS) SUBSTRATE BASED ON SILICON NANOFORREST

### 4.1 Introduction to Nanoforest Formation

A common issue of non-uniformity with deep RIE is nanoforest or black silicon structure formation. Silicon nanopillars, introduced in the last chapter, are one type of high-aspect-ratio nanostructure, with depth from a few to several micrometers. In this case, the etching process needs to be operated under specific conditions to ensure a vertical sidewall profile, since negative tapered sidewalls may cut off nanopillars, while positive tapered sidewalls will introduce a micro-loading effect. The process window for a vertical sidewall profile is normally narrow, especially for fabricating nanometer scale features. If the window is missed, carbon based polymer residual starts to integrate on the substrate and forms a nanoforest. More details considering the parameter effects for the fabricated features will be discussed in Chapter 6. The SEM image in Figure 4.1 shows fabricated nanopillars with a self-formed nanoforest using the aforementioned deep RIE process.

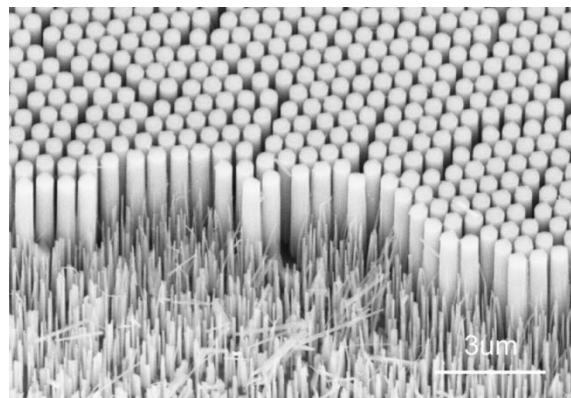


Figure 4.1 Fabricated nanopillars with self-formed nanoforest

Nanostructure self-formation, caused by non-uniformity, can be eliminated by tuning process parameters. However, this unique structure also has potential applications: this black silicon with its sharp tips is an ideal structure for SERS detection [35]. SERS is a technique that enhance molecules' Raman signal by attaching the molecules to rough metal surfaces or to metal nanostructures. It was first observed on roughened silver surface in 1970s and researches base on this technique have been reported extensively since then. This technique can be a powerful tool for chemical sensing, since it can significantly enhance the detection sensitivity of Raman spectroscopy, providing a detectable fingerprint to identify molecules. [33] Today the most commonly used method to prepare SERS surface is by coating a silicon or glass surface with nanostructured metal surface. Different processes have been developed for the substrate preparation, such as using electrochemically roughened silver or lithography patterned gold. [34]

In this chapter, SERS substrate were prepared by silicon deep etching through ICP to form nanoforests structure, or so called black silicon, and the nanoforests structure were covered by a gold layer through sputtering coating. Different approaches have been utilized for black silicon formation in the past decades. For example, I-Ming et al. created both nanopores and nanopillars through rough silicon surfaces, followed by thin masking layer deposition and DRIE [34], and Fang Ji et al. successfully fabricated a nanoforest array on a SOI wafer [36]. Most of these processes involve using  $\text{SF}_6$  and  $\text{O}_2$  as reactive gases [32][34][35]. In this chapter, a two-step DRIE process is developed using ICP for efficient black silicon formation using standard Bosch process reactants  $\text{SF}_6$  and  $\text{C}_4\text{F}_8$ . The fabrication process is suitable for large surfaces and relatively inexpensive. A standard analyte Rhodamine 6G (R6G) shows a significant

enhancement in SERS signals once R6G was applied to the fabricated SERS surface. In addition, a demonstration is presented for single-step detection of bacterial (E.coli) using SERS spectroscopic sensing.

## 4.2 Experimental Details

### 4.2.1 Chemicals and Materials

In this study, 4-inch single side polished silicon wafers were purchased from Ultrasil Corp. Deionized (DI) water was obtained from a DI water purification system (Millipore, FRANCE). Chemicals for surface cleaning and treatment including Acetone, IPA were all from Sigma-Aldrich Inc. Silver nanoplates (AgNPs) (diameter~150nm) were purchased from nanoComposix. Inc. Rhodamine 6G was obtained from Sigma-Aldrich Inc. The bacterial strain (Escherichia coli K12 ATCC 10798) was purchased from ATCC.

### 4.2.2 Fabrication of the Silicon Nanoforest Surface

The wafers were first diced into 2cm × 2cm pieces for mass production. Then each piece was washed with acetone, IPA, DI water, with the help of ultrasonication in sequence. Each cleaning step took 10 mins and the whole process was repeated three times. After cleaning, wafer slices were dried by nitrogen gun and dehydrated by hot plate baking at 100 C° for 20 mins.

The pre-cleaned silicon slice was first etched by exposure to ICP plasma for a standard Bosch process. The anisotropic plasma etch applied alternate cycles of etching in a flow of SF<sub>6</sub> (70 sccm, 3s) and passivation in a flow of C<sub>4</sub>F<sub>8</sub> (55 sccm, 3s) (figure 4.2 a-b). The plasma was generated with an RF power of 800 W and a platen power of 50 W, while the temperature was

kept at 20°C by a stream of nitrogen gas. As a consequence of the high density of passivation residues due to the excessive  $C_4F_8$  supply, a local passivation layer formed, acting as a mask and causing the surface to roughen [38]. This roughness can be controlled by adjusting the process operation time; in a typical experiment, the roughness peaks around 300nm for a 5 min process.

After the first DRIE process, the silicon slice was treated with oxygen plasma in the same chamber for 10s (300 sccm) with 1800 W RF power and 100 W platen power (Figure 4.2.c). The combination of local excessive deposition of reaction products from DRIE and the oxygen complex introduced from RIE oxidation formed masking spots at the peaks of the silicon roughness surface [38].

The sample surface was treated with another DRIE in the same ICP system. The second deep plasma etch applied alternate cycles of etching in a flow of  $SF_6$  (70 sccm, 3s) and passivation in a flow of  $C_4F_8$  (35 sccm, 3s) (Figure 4.2.d). The plasma was generated with an RF power of 800 W and a platen power of 50 W while the temperature is kept steady at 20°C. From a series of experiments, it showed the vertical growth of the needles highly depends on the roughness introduced from the first DRIE. Two extreme conditions were used, the  $SF_6$  etching precursor only or the  $C_4F_8$  deposition precursor only. The experimental consequences were a) a relatively smooth surface after the first DRIE process and b) no nanoforest formation from SEM examination for either condition.

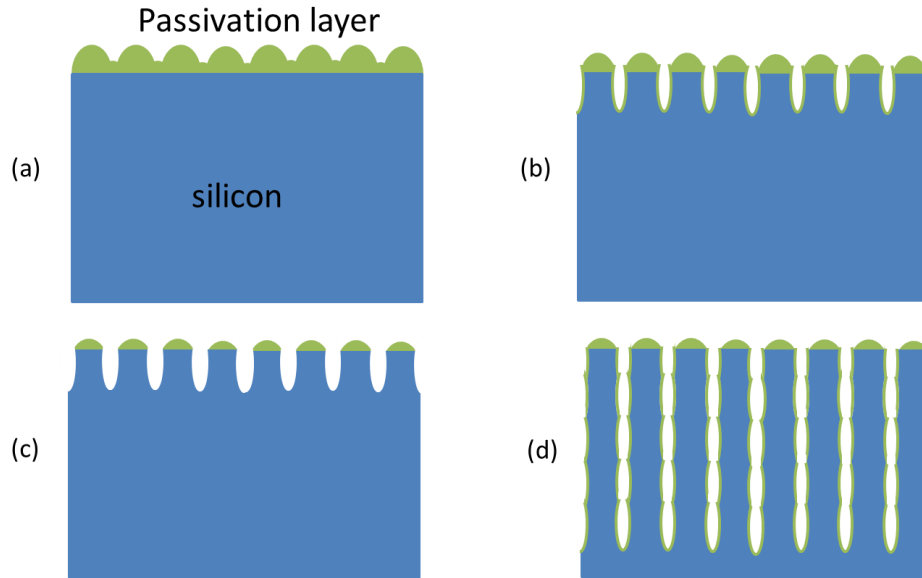


Figure 4.2 Nanoforest formation caused by integrated passivation residual polymer.

#### 4.2.3 Characterization

Au sputtering coating for nanoforest was introduced after the second DRIE. The thickness of the Au layer was set to 25 nm. The nanostructure surface can be rendered hydrophilic by carrying out oxygen plasma treatment.

After Au coating and surface treatment, two experiments were carried out. In the first demonstration, the SERS signal of Rhodamine 6G (R6G), a standard analyte, was detected when it was applied to the SERS surface. All the R6G testing silicon nanoforest samples were merged into the R6G solution overnight for saturated adsorption. The following silver particle deposition was carried out after the silicon nanoforest surface was removed from the R6G solution and dried at room temperature environment without direct light exposure. 2 $\mu$ l silver particle solution was dropped directly onto the substrate and left to dry for 60 mins.

Following this, the second experiment was carried out to detect the enhanced fingerprint signal of a bacterial cell. The bacteria were grown in LB medium at 37 °C for 18 h. Then the bacterial cells were centrifuged and washed with distilled water (18.2 MΩ). Cell damage was implemented by boiling (100 °C) the washed solution for 15 min. The chip was immersed into and incubated in the cell-damaged bacteria solution for 4-5 hours at room temperature. The SERS measurements were operated after the chip was air-dried.

The surface morphology of the silicon nanoforest was characterized by SEM (HITACHI S-4800). A DXR Raman microscope (Thermo Scientific, Waltham, MA, USA) was used for Raman spectra acquisition with 780 nm excitation at 10 mW, 10× objective. The laser exposure time was 60 s and spectral resolution was 2.4–4.4 cm<sup>-1</sup>. The OMNIC™ suite (Thermo Scientific, Waltham, MA, USA) was used for data processing.

## 4.3 Results and Discussion

### 4.3.1 Fabricated Nanoforest

SEM images of the fabricated Si nanoforest are presented in Figure 4.3. As we mentioned before, the diameter and height of these nanoforests could be adjusted by changing the deposition residual amount and Bosch process cycles. A typical diameter of the resulting nanoforest is 10-20 nm on the tip and 50-100 nm on the button while the height-to-width ratio can be as much as 10:1, as shown in Figure 4.3.a. The fabricated nanoforests are robust enough for routine bio-chemistry experiments such as drug loading, hot plate baking, water solution rinses, etc. However, since the silicon-based nanostructures are on the scale of nanometers, these needles are easy to collapse under microsonicator cleaning conditions, making the structure difficult to clean once drugs or nanoparticles have been introduced into and absorbed

by the sample surface. Hence, the bare silicon nanoforest can't be reused and is not compatible with some certain multistep experiments where heavy duty cleaning is required. When the nanoforests are coated by gold layers through sputtering, the needles' sidewalls become smoother, reducing the roughness caused by the alternative cycles of Bosch process through gold layer coating and localized defusion. Meanwhile, the resulting gold-coated nanoforests, shown in Figure 4.3.b, c, d, are very robust comparing with the silicon-only nanoforest. The enhancements in hardness & toughness are caused by not only increasing the diameter of nanoforests but also strengthening their structure through high-density gold layer coating.

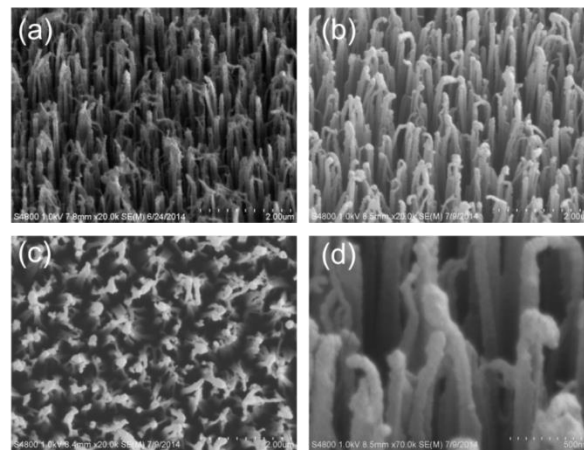


Figure 4.3. SEM images of the fabricated Si nanoforest

#### 4.3.2 R6G SERS Measurement on Nanoforest

First of all, we studied the SERS activity of the nanoforest versus bare silicon. A standard analyte, Rhodamine 6G (R6G) was used with a concentration of  $10\mu\text{M}$ . The average height of the nanoforest is  $\sim 2\mu\text{m}$ . All of the testing samples were fully emerged into a R6G solution for 24 hours to assure saturation adsorption. Since it is difficult to identify the specific deposited R6G molecules that scatter the light, the concentration of the R6G solution used for molecule

loading is used here as a relevant concentration for analysis. All of the following signal enhancement calculations and analysis are based on this definition. For the control experiment, approximately 0.1mm thick of R6G powder layer was placed on a bare silicon wafer surface for SERS detection. The results showed no Raman bands in these two testing sample surfaces after R6G adsorption, while the control experiment showed strong signals at -600, 800, 1200, 1300, 1350, and 1500  $\text{cm}^{-1}$  (Figure 4.4). One possible explanation is that Raman signals for R6G on testing samples are too weak for detection due to the low R6G concentration. However, it conflicts with the measurement results for the Au sputtering-coated nanoforest, which showed a strong Raman signal under the same concentration (Figure 4.5). Based on the analysis above, the results indicate that neither nanoforest nor bare silicon shows SERS activities. The Raman band for silicon is shown at -520  $\text{cm}^{-1}$  and dominates the spectrum for both nanoforest and bare silicon surfaces. However, the silicon nanoforest has a much stronger Raman signal for silicon under the same experimental environment, as Figure 4.4 shows. One reasonable proposition is that the integration of R6G forms a thin layer of polymer on the bare silicon surface and blocks the excitation of a Raman signal of silicon. In contrast, the nanoforest sample has a complicated surface structure and the spaces between those peaks are quite deep, making it difficult to form a continuous thin layer of R6G, minimizing possible effects on the Raman signal.

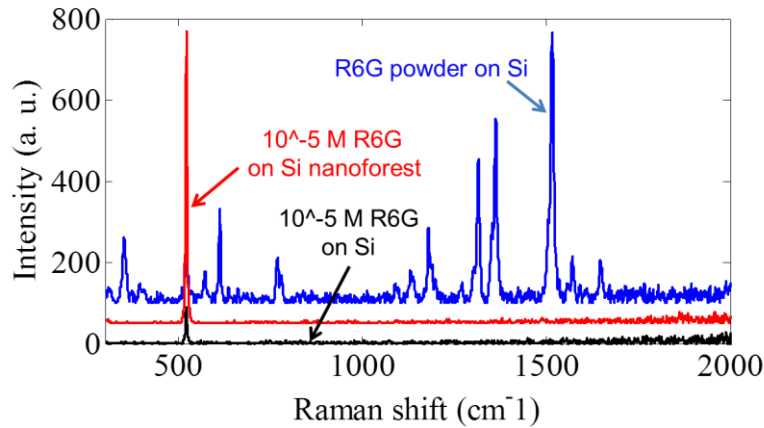


Figure 4.4 Raman signal of R6G on inactive SERS substrates.

### 4.3.3 SERS Measurement on Gold-coated Nanoforest

Since Au is essential for SERS signal enhancement, an additional 25nm Au thin layer was sputter-coated onto the nanoforest surface. Raman spectrums from silicon nanoforest and Au-coated silicon nanoforest are compared in Figure 4.5. SERS signals of R6G with 10  $\mu$ M concentration were reliably detected for Au-coated Si nanoforests. Bare silicon nanoforests with the same concentration of R6G, on the other hand, did not show any reproducible Raman signals. To further study the mechanism of Raman signal enhancement, a bare silicon surface and an Au-coated bare silicon surface were introduced for SERS signal detection in the same experimental environment. Weak R6G Raman signals are shown in Figure 4.5 for the gold-coated silicon surface, while no Raman signals appear for the bare silicon surface. The most significant SERS signal enhancement was achieved from the combination of an Au thin layer and the silicon nanoforest condition among all previously mentioned sample surfaces. It clearly demonstrates the contribution from both the Au thin layer and the nanoforest

nanostructure. The enhancement factor  $F_{en}$  of the Au-nanoforest surface could be achieved according to the following formula [32]:

$$F_{en} = \frac{C_{ref}}{C_{sample}} \times \frac{I_{sample}}{I_{ref}} \quad (4.1)$$

Here  $I_{sample}$  and  $I_{ref}$  are the signal intensity of the sample and reference surface, while  $C_{ref}$  and  $C_{sample}$  are the relevant concentration of R6G as previously defined. Since the Raman signals of 10  $\mu$ M R6G are too weak for detection, a bare silicon surface is coated by 40 mM R6G. At this concentration level, the Raman signal of R6G can be detected (as Figure 4.6 shows) and the enhancement factor can be achieved from Formula 4.1. Calculated results are listed in Table 4.1. Comparing these results with other groups' work [32-33], the enhancement factor achieved in this type of substrate is in the same range.

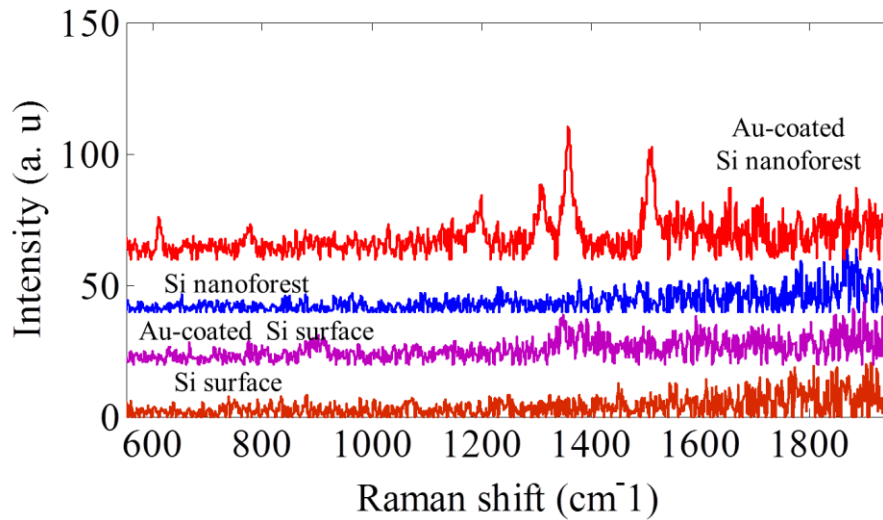


Figure 4.5 Raman spectrum of R6G on difference substrates.

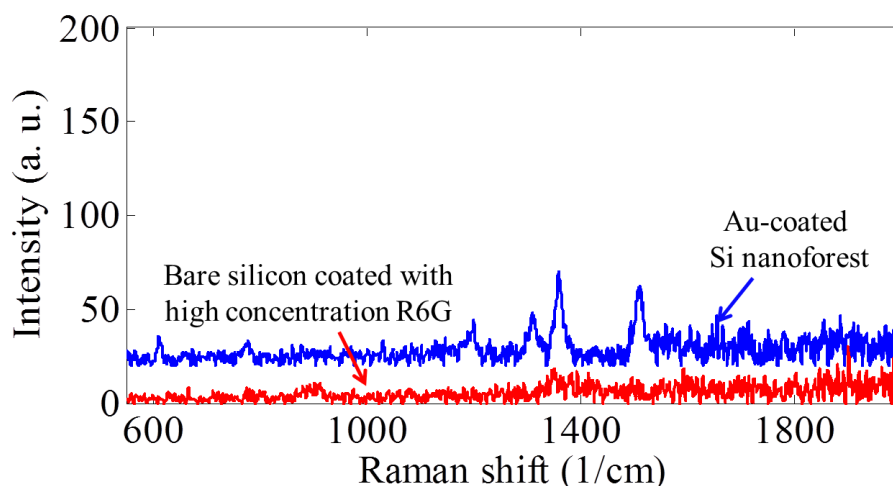


Figure 4.6 Reference Raman signal of silicon coated with high-concentration R6G

Table 4.1 Signal enhancement for peaks at 1308  $\text{cm}^{-1}$ , 1361  $\text{cm}^{-1}$  and 1507  $\text{cm}^{-1}$  referenced to a plain silicon surface

Raman shift (1/cm)	1308	1361	1507
Intensity (a.u)	25	49.3	40
Reference intensity (a.u)	7	9.5	11
Enhancement	1.4E+04	2.1 E+04	1.5 E+04

#### 4.3.4 SERS Measurement on Ag Particles Decorated Au-coated Silicon Nanoforest

To achieve stronger SERS signal enhancement of R6G, we also applied silver nanoparticles to the sample surface. The Au-coated silicon nanoforest samples were merged into the R6G solution overnight and left to dry at room temperature condition. Then silver plate nanoparticle dispersion (diameter~150nm) purchased from nanoComposix Inc. was diluted 10 times and directly dropped onto the nanoforest using a micropipette. Since the contact angle of the silver nanoparticle dispersion was relatively small ( $\sim 20^\circ\text{C}$ ),  $2\mu\text{l}$  solution was used for surface decoration to avoid overflowing. The measured Raman signal is given in Figure 4.7. As shown,

S1 is a reference signal measured from a bare Au-nanoforest surface, while S2 is from the second Au-nanoforest sample surface with and without decorated Ag particles. As expected, SERS signals of Au-coated silicon nanoforests with or without silver application are reliably detected with 10 $\mu$ M concentration of R6G. These results also indicate the intensity of Raman signals are further enhanced after introducing silver particles.

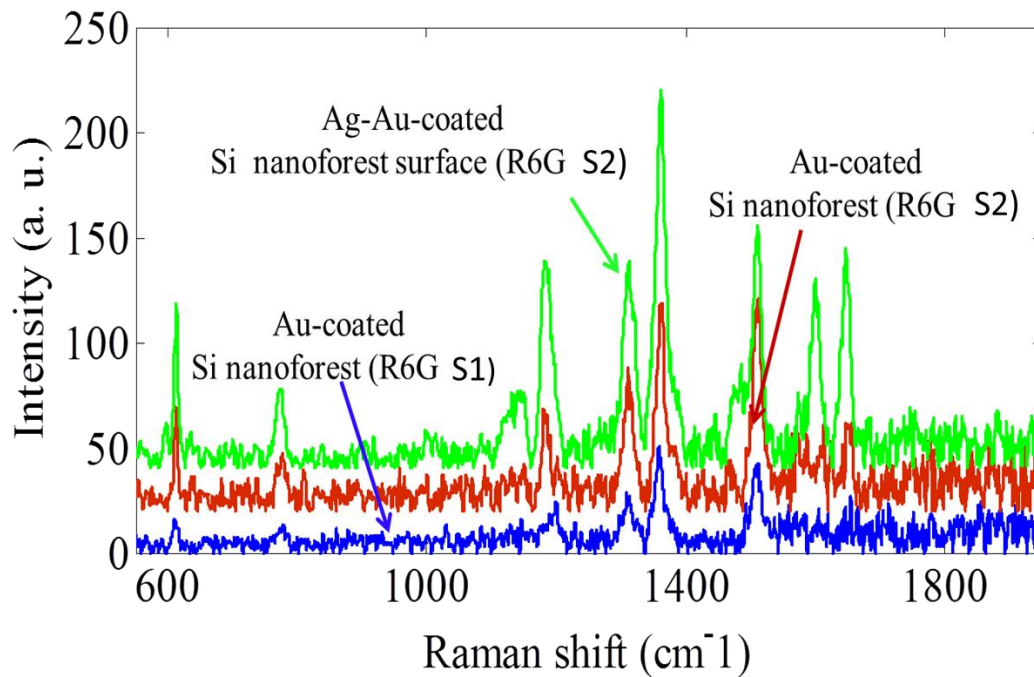


Figure 4.7 SERS measurement on Ag particles decorated Au-coated silicon nanoforest

#### 4.3.5 Cell SERS Measurement on Au-coated Silicon Nanoforest

More practical experiments were performed to demonstrate to detect Raman signals from bacterial cells. Initial tests directly merged Au-coated glass or Au-coated silicon nanoforest substrate surfaces into a bacterial cell (*E. coli*) solution. However, the target Raman spectral signal cannot be detected even for the highest concentration *E. coli* available in the lab (10<sup>8</sup> colony-forming units per milliliter (CFU/mL)). The measurement results are not listed here since

only noise can be observed. One reasonable proposition is the nanoscale nanoforests are only in direct contact with a fraction of the bacterial cell, since the normal range for an E. coli bacterial cell is approximately two to three micrometers, which is several hundred times bigger in dimension compared with nanoforest tips. Besides, SERS decays exponentially away from the surface of nanoforests, resulting in very little Raman spectral signal enhancement from the majority of the bacterial cells. To address this issue, we broke bacterial cells into small fractions to increase the contact area with the nanoforest tips. Cell damage was implemented by boiling (100°C) the washed solution for 15 min. Then the sample was immersed into and incubated in the cell-damaged bacteria solution for 4-5 hours at room temperature. The SERS measurements were operated after the chip was air-dried. E. coli (with concentrations of  $10^6$  and  $10^7$  (CFU/mL)) was detected using the nanoforest-based SERS substrate; all spectra are averaged by 15–20 spectra in each treatment for reliable results. As shown in Figure 4.8, the fingerprints of E. coli are clearly visible. The fingerprints cannot be observed for the same concentration of E. coli applied on Au-coated silicon surface. The estimated enhancement factor of the SERS substrate is several orders of magnitude [32-33]. The standard E.coli signature peak assignments without damage are provided by Dr. Chao Wang from Iowa State University and listed in Table 4.2. Compared with the measurement results from damaged E.coli, these band assignments are very similar, indicating that measurements can be taken by breaking bacterial cells without changing the band assignments.

Table 4.2 E.coli signature peak assignments without damage (provided by Dr. Chao Wang from Iowa State University)

Wavenumber (cm-1)	Band assignment
2938	C-H vibration
2921	C-H vibration
2885	C-H vibration
1660	Amide 1 vibration
1594	DNA vibration
1450	$\delta(\text{CH}_2)$ in Lipid
1331	$\gamma(\text{NH}_2)$ adenine, polyadenine, DNA
1032	Adenine, polyadenine, DNA
1002	Phenylalanine in protein
954	CN stretching
855	Tyrosine
733	adenine, polyadenine, glycosidic ring mode, DNA

To demonstrate the multiplexed detection, E. coli and R6G are both uniformly applied to the same nanoforest-based SERS substrate. As shown in Figure 4.9, both fingerprints of E. coli and R6G can be observed clearly.

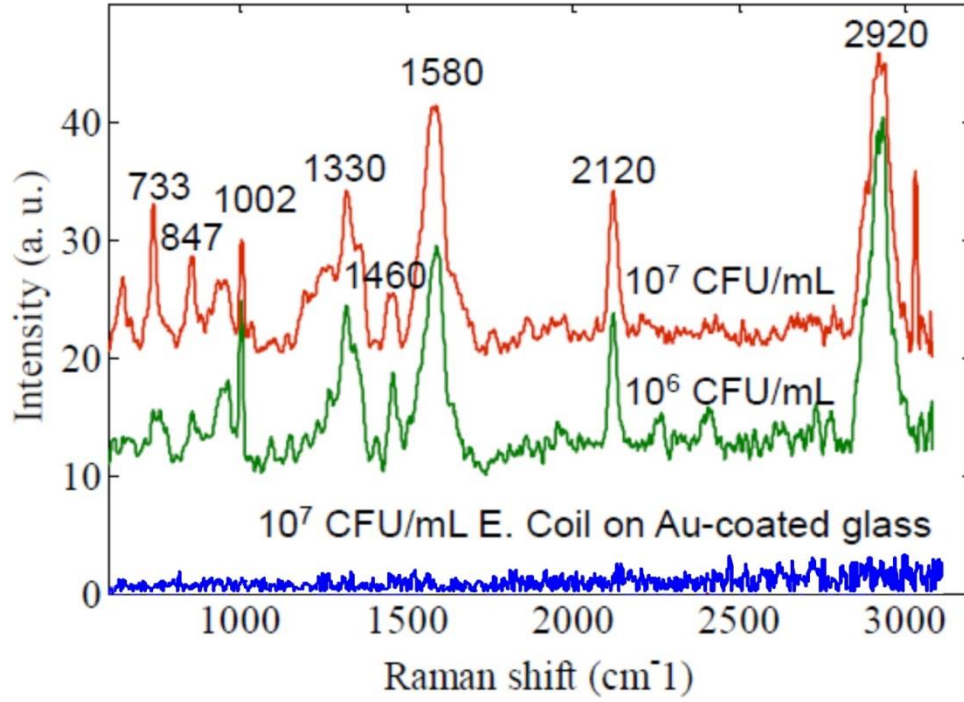


Figure 4.8 *E. coli* Raman signal measurements on Au-coated silicon nanoforest

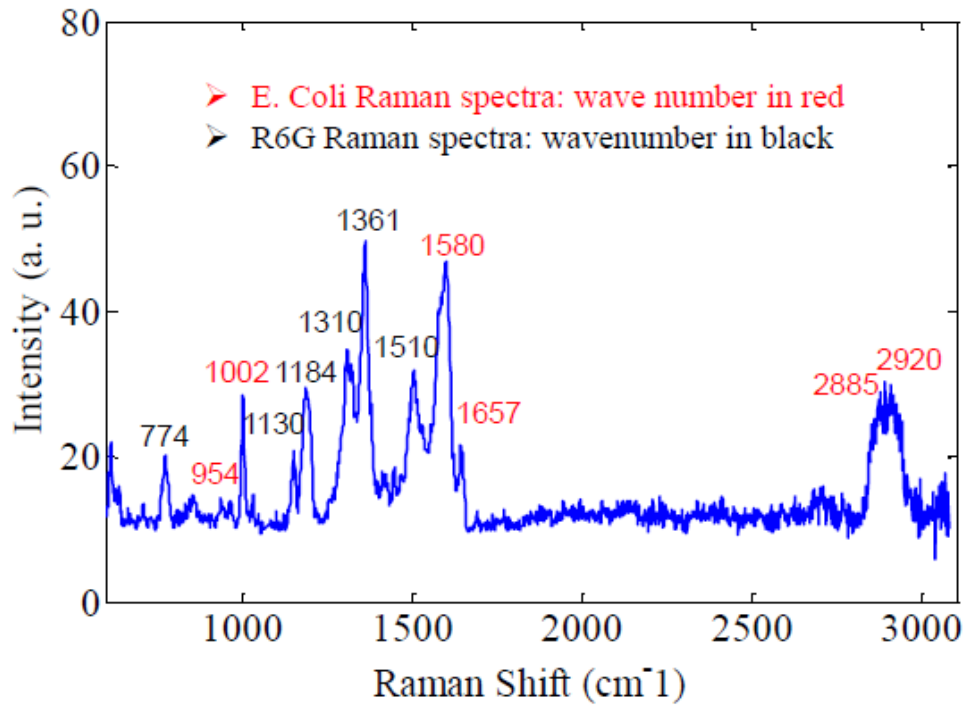


Figure 4.8 *E. coli* and R6G Raman signal measurements on Au-coated silicon nanoforest

#### 4.4 Conclusions

In summary, a maskless two-step ICP-based dry etching process has been developed to fabricate silicon nanoforests from bare silicon wafer. By coating the nanoforest with a thin layer of Au and decorated by Au nanoparticles, the standard analyte Rhodamine 6G (R6G) demonstrates a significant enhancement in SERS signals under the same experimental environment. In addition, SERS enhancement of the fingerprinting peaks of bacterial targets is demonstrated. This type of nanoforest-based SERS platform could be very useful for label-free detection and the multiplexed detection.

## CHAPTER 5 A TOP-DOWN FABRICATION PROCESS FOR VERTICAL SILICON

### NANOTUBES

#### 5.1 Introduction to nanotube fabrication

The nanotube is one of the most important and widely used nanostructures in the nanoscience and nanotechnology fields. One example of its uses is the carbon nanotube (CNT), usually vertically aligned and synthesized using a bottom-up approach [39–40]. Nanotubes can also be fabricated using a top-down approach [41–42]. The advantages of the top-down approach include a lower temperature process, controlled locations of the nanotubes on a substrate, and compatibility with well-established silicon process technology, providing for easy integration with microdevices and microfluidic devices.

Some representative examples of nanotubes fabricated from different materials are summarized in the following. Silicon nanotubes have been fabricated by combining electron-beam lithography (EBL) and a dry etching process [41]. Silica nanotubes have been fabricated using nanowire templates [42]. Using anodic aluminum oxide (AAO) as a template, carbon nanosyringes have been formed by carbon deposition, ion milling, and chemically etching the AAO [43]. Alumina nanostraws have been fabricated by a conformal alumina atomic layer deposition (ALD), then an alumina-specific directional reactive ion etch (RIE), followed by a polycarbonate specific directional RIE [44]. CVD-based Ge-nanowire-template synthesis of silicon nanotubes has also been reported previously with high crystallinity and precise control over morphologies [45–47]. Recently, Duan et al. have reported a new process to fabricate SiO<sub>2</sub> nanotubes [48]. In the process, Ge nanowire (GeNW), grown through an Au nanodot catalyzed

VLS process, is used as a template. The nanotubes are formed by an ALD  $\text{SiO}_2$  conformal coating of the GeNWs, then photoresist is applied with a thickness smaller than that of GeNWs. The  $\text{SiO}_2$  at the tip of the GeNW is etched by buffered HF (BHF). The  $\text{SiO}_2$  nanotubes are finally formed by selectively etching GeNWs.

Nanotubes can provide a unique platform for multiple applications, such as drug delivery [49], cell transfection [42], and advanced patch-clamp technique [50–51]. Specifically, by using nanotubes as drug containers, smaller and more accurate amounts of drugs can be delivered and administered to the target. This could be very critical to control dosage delivery and release, thereby achieving optimal therapeutic effect and mitigating toxicity. Moreover, by taking advantage of the nanoscale size of the nanotube to load biological cargos, negligible damage on the cell would be introduced when the nanotubes penetrate the cell membrane during a transfection procedure, thus improving the viability of the cells. Using a nanotube with a nanoscale-size tip as a pipette in a patch-clamp technique, high resolution monitoring of the cell ion channel can be achieved, benefiting studies of the cell ion channel and drug discovery related to ion channel diseases. In addition to the those mentioned above, nanotubes can also be explored for the following important applications: (i) enhanced optical absorption or trapping for harvesting solar energy, due to their large surface/volume ratio and zigzag reflectance of incident photons, similar to the properties of CNTs and nanopillars [52–54]; (ii) an anti-fouling surface resulting from the nanostructured or nanotextured surface of the arrayed nanotubes, resulting in super hydrophobicity [55]; and (iii) many other potential bio/chemical sensing and detection applications such as single DNA stretching and sequencing [56–57]. However, some of the aforementioned fabrication processes usually involves one or multiple

expensive steps, such as EBL. The EBL step in these reported processes might be a barrier for preventing the rapid and cost-effective high-volume production of this type of nanostructure.

Herein, a simple, template-free, rapid and low-temperature (i.e., room temperature) top-down process for fabricating silicon nanotube from a single crystal silicon wafer is reported. The basic process flow is illustrated in Fig.5.1, and utilizes a Bosch process twice with polystyrene nanosphere beads as the masks. The Bosch process consists of two alternate and repeated deposition/etching steps to achieve nearly vertical micro or nanostructures [58]. During the Bosch process (Fig.5.1c–f), the deposition precursor  $C_4F_8$  gas is first dissociated by the plasma, then undergoes polymerization reactions upon deposition on the top surface and the sidewall of the nanopillars, resulting in a perfluorocarbon polymeric layer on the top surface and the sidewall as the chemically inert passivation layer [36]. The  $SF_6$  gas for the etching provides directional ions that bombard the substrate, removing the passivation layer at the bottom of the trench, but not along the sidewall. The ions collide with the passivation layer and sputter off the passivation layer, exposing the surface in the trench to the chemical etchant  $SF_6$ . As a result, the nanopillars (Fig.5.1c) and the silicon nanotubes (Fig.5.1f) are formed sequentially. To the best of our knowledge, this is the first effort to fabricate silicon nanotubes by using a series of standard top-down microfabrication processes. This process could be adapted or modified to fabricate nanotube from a class of different materials.

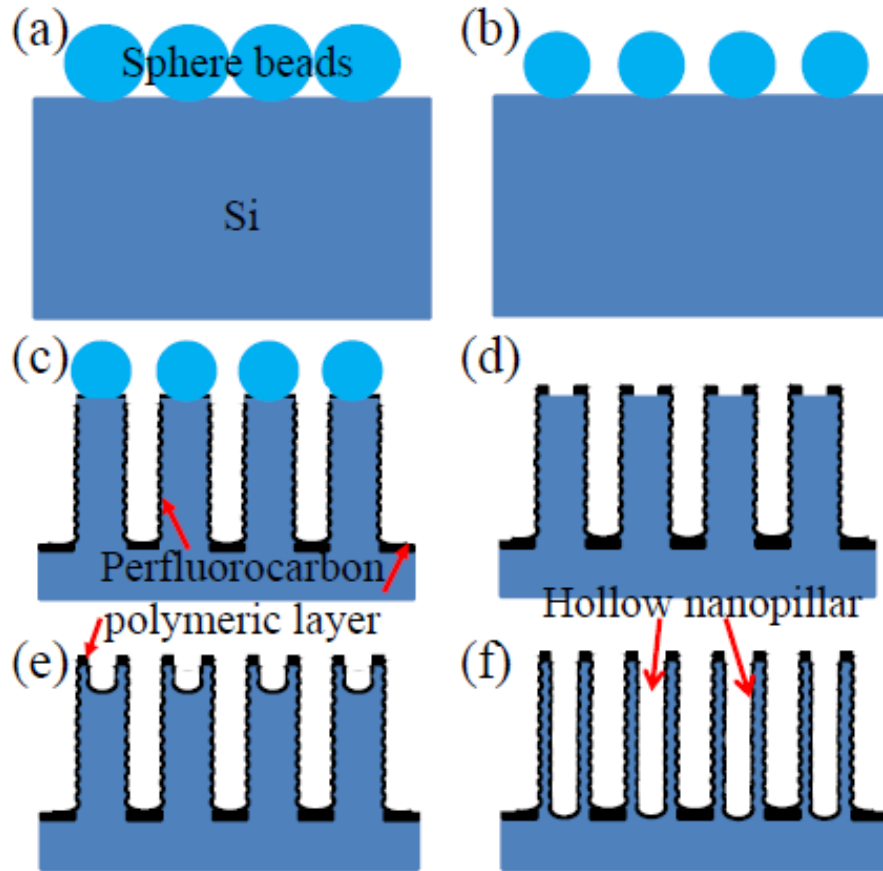


Figure 5.1. The process flow for fabricating silicon nanotubes: (a–b) Self-assembled nanosphere beads on the silicon wafer, followed by first oxygen plasma RIE to shrink the beads' size; (c) First Bosch process carried out to fabrication nanopillars; (d) Second oxygen plasma RIE carried out to remove the beads; (e–f) Second Bosch process carried out to fabricate nanotubes.

## 5.2 Experimental details

### 5.2.1 Chemicals and Materials

The polystyrene nanosphere beads of different sizes (500 nm, 1000 nm, 3000 nm) were purchased from Fisher Scientific Inc. Triton X-100 and methanol were both purchased from Sigma-Aldrich Inc. Deionized (DI) water was obtained from a DI water purification system (Millipore, FRANCE). Silicon wafers were obtained from Ultrasil Corp. Chemicals for surface

cleaning and treatment including Acetone, IPA, 98% Sulfuric acid, and 30% Hydrogen peroxide were all obtained from Sigma-Aldrich Inc.

### 5.2.2 Fabrication of silicon nanotubes

First, single side polished p-type 4 inch silicon wafers (Ultrasil Corp) are cut into 2 cm × 2 cm pieces. Then each piece is cleaned by acetone, IPA, and DI water, with ultrasonication for 20 mins in each solution in sequence. Then the silicon pieces are immersed in a fresh piranha solution (a mixture of sulfuric acid and hydrogen peroxide (3:1)) in a beaker, which is kept on a hot plate at 60 °C for half an hour. Thereafter the silicon pieces are taken out from the beaker and rinsed thoroughly by DI water. After the surface treatment, the silicon pieces can be used immediately or stored in DI water to avoid formation of native oxide for future use.

Polystyrene (PS) nanosphere beads are dispersed uniformly in a solution containing Triton X-100 and methanol (1:400). Then a certain amount of PS bead solution is directly applied to each silicon piece by a micropipette. The solution is left to dry without any disturbance at room temperature for several hours. As shown in Fig.5.1a, PS nanosphere beads are self-assembled into a close-packed monolayer. The beads are then tailored by oxygen plasma to shrink their size (Fig. 5.1b).

Using the PS beads as the mask, the first inductively coupled plasma (ICP) Bosch process (Fig. 5.1c) is applied for fabricating the nanopillars. In the process, alternate cycles of etching in a flow of SF<sub>6</sub> and passivation in a flow of C<sub>4</sub>F<sub>8</sub> are used. Unless otherwise stated, the plasma is always generated with an RF power of 800 W. The temperature is kept at 20 °C by a stream of nitrogen gas. The height of the nanopillars can be controlled by adjusting the number of process cycles. After the etching process, the samples are washed in the piranha solution for

half an hour, then ashed with oxygen plasma (Fig.5.1d) to remove the residual beads. Then the second ICP Bosch process (Fig.5.1e–f) is carried out to form the silicon nanotubes.

### 5.2.3 Characterization

The images and surface morphology of the samples are obtained and characterized by a scanning electron microscope (SEM, HITACHI S-4800). The composition of the silicon nanotubes is analyzed using Energy Dispersive X-ray Spectrometry (EDS) on the same SEM.

## 5.3 Results and discussion

In Fig.5.2a and Fig.5.2b, the scanning electron microscope (SEM) images of silicon nanopillars before and after removing the nanosphere beads are given, which corresponds to step *c* and step *d* in Fig.5.1, respectively. As aforementioned, the Bosch process consists of alternate passivation ( $C_4F_8$ ) and etching ( $SF_6$ ) steps to fabricate nearly vertical micro or nanostructures. After removing the nanosphere beads, the shadow area (bare silicon surface) occupied by the nanosphere bead in the top center of each nanopillar appears different from other areas, resulting from the deposition of the passivation layer as shown in Fig.5.2b and its inset. The formation of the shadow area underneath the bead is the key to fabricate the silicon nanotubes.

In order to fabricate the silicon nanotubes successfully, the formation of a single layer of nanosphere beads on the silicon surface is critical. Namely, the nanopillars cannot be fabricated properly if multiple layers of nanosphere beads are formed. Another critical parameter is the adhesion of the beads to the silicon surface from steps *a* to *c* in Fig.5.1. In these steps, the nanosphere beads should remain firmly on the silicon surface. If any beads are detached from

the silicon wafer during these steps, nanopillars in those locations cannot be formed; as a result, the passivation layer cannot be deposited on the surface of the nanopillar properly with a shadow area underneath each nanosphere bead. In addition, the dimensions of the silicon nanotubes such as diameter (inner diameter and outer diameter), wall thickness, and interspacing are essentially determined by the size of the nanosphere beads, especially in step *b* in Fig.5.1 after being tailored by oxygen plasma etching. The second Bosch process (step *e* to *f* in Fig.5.1) is another critical step for fabricating the silicon nanotubes. SEM images in Fig.5.2c and Fig.5.2d give two representative fabricated results after the second step Bosch process. As can be seen in Fig.5.2c and its inset, the outer diameter of the upper portion of the silicon nanotubes is smaller than that of the lower portion of the silicon nanotubes; tapered silicon nanotubes are thus formed. In this case, alternate cycles of etching in a flow of  $\text{SF}_6$  (flow rate: 150 sccm; time: 2 s) and passivation in a flow of  $\text{C}_4\text{F}_8$  (flow rate: 100 sccm; time: 2.5 s) are used. The plasma is generated with an RF power of 800 W. The relatively large passivation ( $\text{C}_4\text{F}_8$ : 100 sccm, 2.5 s) causes increased difficulty for etching silicon ( $\text{SF}_6$ : 150 sccm, 2 s) from the upper portion to the lower portion of the silicon nanopillar, resulting in the tapered silicon nanotubes. In contrast, as shown in Fig.5.2d, the silicon nanotubes are not tapered, but significantly increased openings in the walls are clearly visible. In this case, alternate cycles of etching in a flow of  $\text{SF}_6$  (flow rate: 150 sccm; time: 4 s) and passivation in a flow of  $\text{C}_4\text{F}_8$  (flow rate: 90 sccm; time: 5 s) are used. These process parameters can minimize the formation of the tapered silicon nanotubes, but under this condition, the walls of the nanopillars are not protected effectively by the passivation layer, and large-sized scallops are formed in the walls during the passivation/etching cycle [58], resulting in openings in the walls and the formation of *skeletons*

of the nanotubes. Hence, in order to fabricate silicon nanotubes robustly, the selection of the time for passivation and etching in each cycle and the corresponding gas flow rates during the Bosch process is crucial.

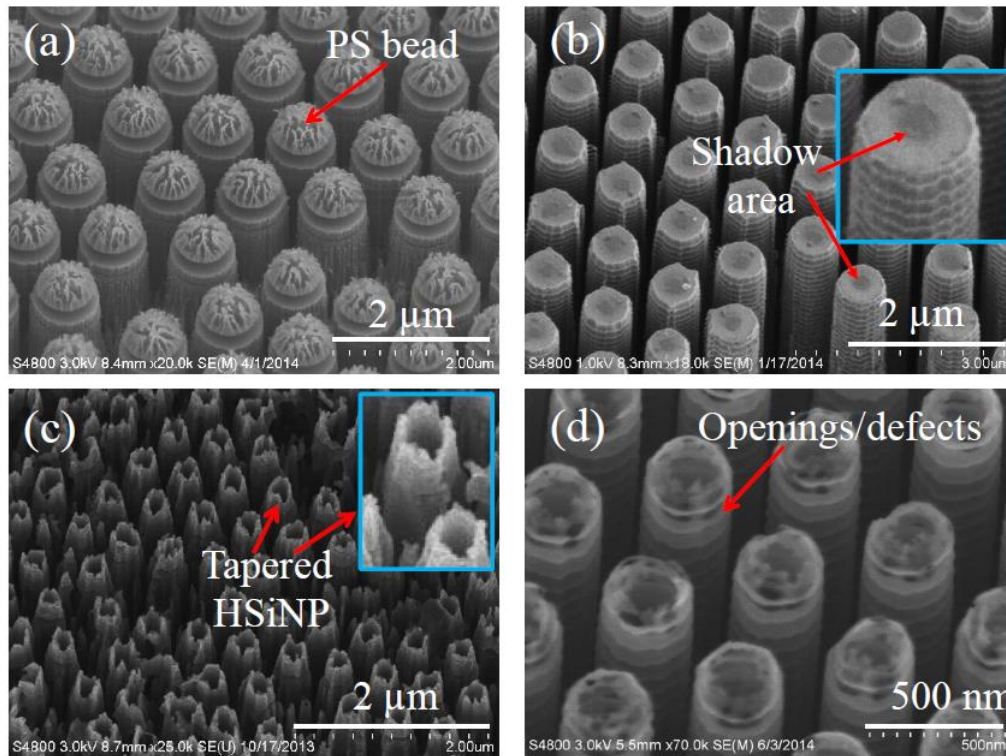


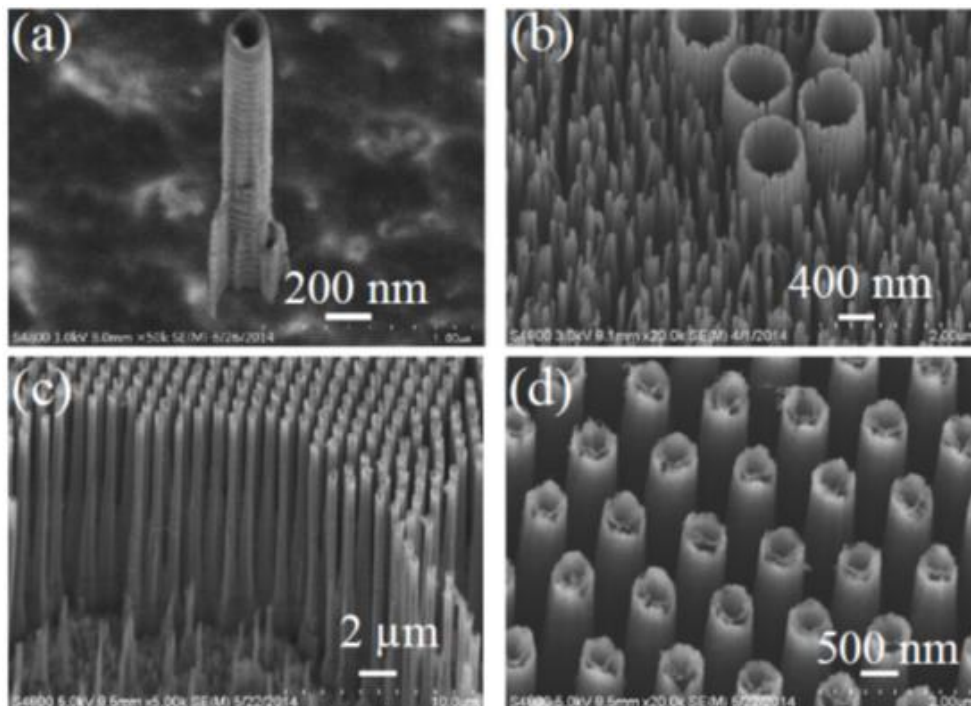
Figure 5.2. SEM images: (a) Bead-capped Si nanopillars; (b) After removing the beads, a shadow area in the center of the top of nanopillar is clearly visible, indicating that the center of the top of Si nanopillar is bare silicon, while other parts of the Si nanopillar (including the sidewall) are covered by a passivation layer (perfluorocarbon polymer); (c) Tapered silicon nanotubes; (d) Openings/defects in the wall of the silicon nanotubes.

To this end, the process parameters have been modified and optimized for fabricating the silicon nanotubes. Some representative SEM images of the fabricated silicon nanotubes are given in Fig. 5.3. A single silicon nanotube was fabricated on a silicon substrate in Fig. 5.3a. The wall thickness is  $\sim 35$  nm without any openings or cracks in the wall. Its outer and inner diameters are  $\sim 210$  nm and 140 nm, respectively. The scallops on the wall of the silicon

nanotubes are clearly visible. Some randomly distributed silicon nanotubes on a silicon substrate, shown in Fig.5.3b, were fabricated when nanosphere beads were sparsely and randomly distributed on the substrate as the mask during the nanopillar formation step. Another distinct feature is that these silicon nanotubes are distributed among a silicon nanoforest. In this case, alternate cycles of etching in a flow of  $SF_6$  (flow rate: 150 sccm; time: 2 s) and passivation in a flow of  $C_4F_8$  (flow rate: 110 sccm; time: 2.5 s) caused the silicon nanoforest to form, due to the perfluorocarbon polymer-based nanomasks created during the Bosch process; this is similar to the formation of the black silicon reported in previous research [60]. In addition, it has also been found that if the process chamber is not cleaned after each Bosch process, the possibility for nanoforest formation increases due to the re-deposition of the polymer-based nanomasks on the silicon wafer from polymer residuals on the inner surface of the process chamber [36]. Hence, the cleanliness of the process chamber is another important factor to mitigate or eliminate nanoforests.

By modifying process parameters, the density of the silicon nanoforest around the silicon nanotubes can be significantly mitigated or eliminated as shown in Fig.5.3a and Fig.5.3c–f. In these cases, alternate cycles of etching in a flow of  $SF_6$  (flow rate: 150 sccm; time: 2 s) and passivation in a flow of  $C_4F_8$  (flow rate: 90 sccm; time: 2.5 s) are used. The basic idea is to mitigate or eliminate the perfluorocarbon polymer-based nanomasks formed on the silicon surface. Once this is achieved, the formation of nanomasks becomes negligible since the deposited polymer can be efficiently removed during etching. It has been found that the surface of the sample appears dark when there is significant nanoforest density, as shown in Fig.5.3b, in which the height of the nanoforest is almost equal to that of the silicon nanotubes.

In contrast, the surface of the sample appears grey/white when the density of the silicon nanotubes is low, such as in the samples shown in in Fig.5.3a and Fig.5.3c–f, which have relatively clean floors without clearly visible nanoforest. This is because the height of the nanoforest is much lower than that of the silicon nanotubes, and the density of the nanoforest is also very low. As can be seen, the scallops on the wall of the silicon nanotubes in Fig.5.3b–f also become much smaller, and thus the surface of walls are smoother than that in Fig.5.3a. In Fig.5.3c–f, the silicon nanotubes of different dimensions are fabricated using 500 nm beads as the mask. Since the time used for oxygen plasma RIE to shrink the size of the beads varies, as does the time used for the Bosch process to fabricate the silicon nanotubes, the dimensions and density of silicon nanotubes are different. Arrayed silicon nanotubes are found to be well-aligned vertically and uniformly distributed on the substrate. The density of the silicon nanotubes can be as high as  $1.3 \times 10^8 / \text{cm}^2$  and the height-to-width aspect ratio (HWAR) can be as high as 20.



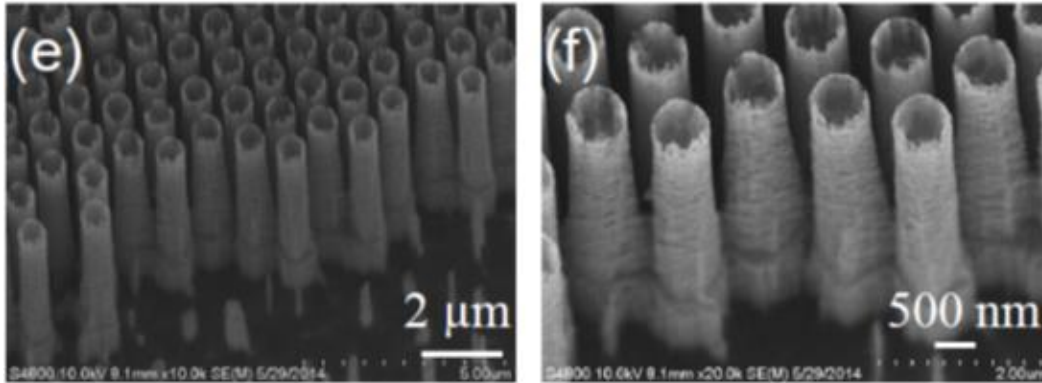


Figure 5.3. SEM images: (a) A single silicon nanotube; (b) Several silicon nanotubes randomly formed among a silicon nanoforest; (c–d) Arrayed silicon nanotubes fabricated by a 10-minute Bosch process; (e–f) Arrayed silicon nanotubes fabricated by a 2-minute Bosch process. All images were taken at a 30° SEM stage tilt.

To confirm the formation of perfluorocarbon on the wall of the silicon nanotubes, the composition of the fabricated silicon nanotubes has been analyzed using energy dispersive X-ray spectrometry (EDS). The measured X-ray spectra of the fabricated silicon nanotubes and a set of quantitative data associated with the spectra are given in Fig.5.4a. As can be seen, the most abundant element is Si, which is 88.09 wt%. Other major elements present are carbon (8.69 wt%) and fluorine (1.13 wt%), which indicate the existence of the perfluorocarbon. The oxygen element (2.09 wt%) could be a combination of the native  $\text{SiO}_2$  of the silicon wafer and the formation of  $\text{SiO}_2$  due to some residual oxygen in the chamber during the ICP-Bosch process. In summary, it appears that the depth of the hollow core of the nanotube is determined by the total time used in the second Bosch process. As shown in the SEM images of the cross-sections of two nanotubes in Fig.5.4b–c, the hollow core clearly formed inside the walls and continues to the bottom of the nanotube. It should be noted that the hollow cores may not continue to the bottom for nanotubes with large HWAR due to the microloading effect [61].

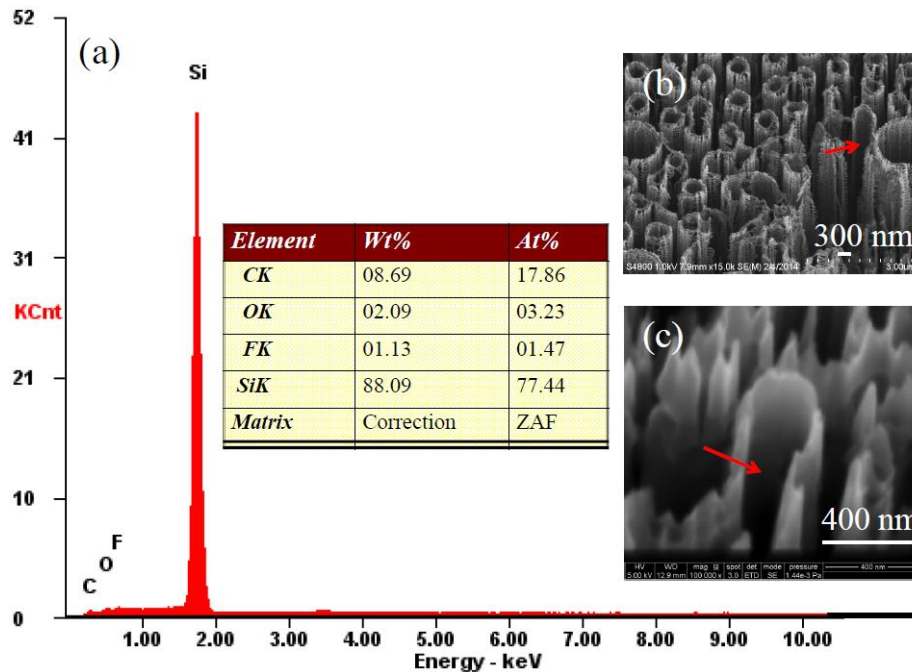


Figure 5.4. (a) The measured X-ray spectra of the nanotubes; (b–c) cross-section SEM images of two nanotubes, showing the hollow cores formed inside their walls and extending to their bottoms (pointed by the red arrows). All the images were taken at a 30° SEM stage tilt.

As demonstrated, the dimensions of the silicon nanotubes such as diameter, density, and height can be controlled by adjusting bead and process parameters. Herein, tailoring of the ratio of the wall thickness to the diameter of the silicon nanotubes has also been demonstrated by modifying bead size and process parameters. For the fabricated silicon nanotubes in Fig.5.5a–b, the wall thickness of the silicon nanotubes is ~50 nm, the outer diameter of the silicon nanotubes is ~800 nm, and the inner diameter of the silicon nanotubes is ~700 nm. The ratio of wall thickness to the outer diameter of the silicon nanotubes is ~1/16. In this case, alternate cycles of etching in a flow of SF<sub>6</sub> (flow rate: 150 sccm; time: 2 s) and passivation in a flow of C<sub>4</sub>F<sub>8</sub> (flow rate: 90 sccm; time: 2.5 s) are used. The large inner and outer diameters are formed due to the large size of the beads. The ratio of wall thickness to the outer diameter of

the silicon nanotubes can be increased by changing bead size and process parameters. For the fabricated silicon nanotubes in Fig.5.5c–d, the wall thickness is  $\sim 70$  nm, the outer diameter is  $\sim 210$  nm and the inner diameter is  $\sim 70$  nm. The ratio of wall thickness to the outer diameter of the silicon nanotubes becomes  $\sim 1/3$ , and the wall thickness itself is nearly the same as the inner diameter of the silicon nanotubes. In this case, alternate cycles of etching in a flow of  $\text{SF}_6$  (flow rate: 130 sccm; time: 2 s) and passivation in a flow of  $\text{C}_4\text{F}_8$  (flow rate: 90 sccm; time: 2.5 s) are used. These results indicate the flexibility of the process for fabricating silicon nanotubes with variable dimensions.

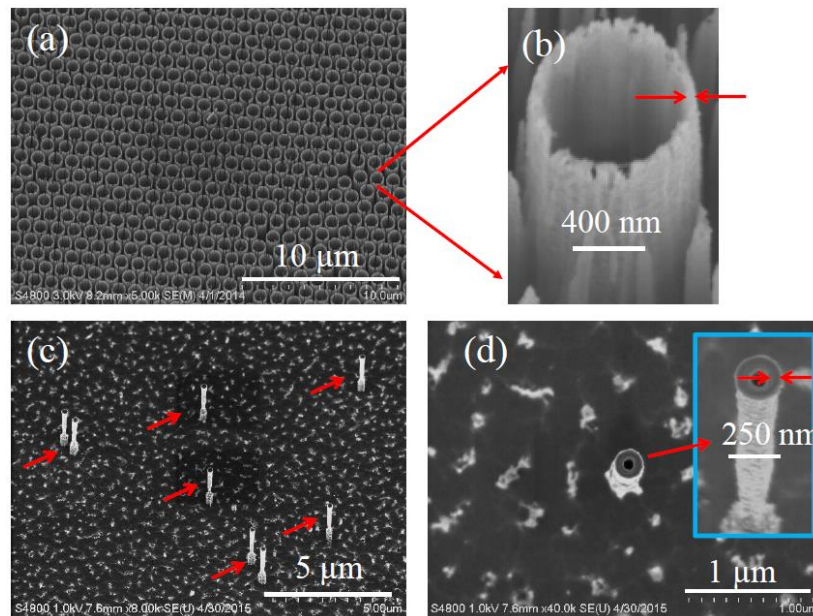


Figure 5.5. SEM images: (a) Arrayed silicon nanotubes fabricated on silicon substrate; (b) Close-up of one single silicon nanotube: ratio of wall thickness to the outer diameter is  $\sim 1/16$ ; (c) Silicon nanotubes (indicated by red arrows) fabricated on silicon substrate; (d) Top-down view of a single silicon nanotube with inset showing a close-up side view of a silicon nanotube ratio of wall thickness to the outer diameter is  $\sim 1/3$ .

At the current stage, the smallest outer diameter at which silicon nanotubes can be fabricated robustly is around 200 nm; this could be further reduced after further research and

development. The big challenge to forming silicon nanotubes with smaller outer diameters is control of the lateral etching/undercut to reduce the scallop size on sidewalls. It has been found that the diameter of nanopillars can be fabricated as small as tens of nanometers. However, due to pronounced scallops on their walls, it becomes very challenging to fabricate silicon nanotubes from these nanopillars. Similarly, the wall thickness of silicon nanotubes is also limited by the scallop effect. Finally, it should be noted that the process could be adapted to fabricate nanotubes from different types of materials, including metals, oxides (i.e., SiO<sub>2</sub>), and other semiconductors, providing a generic technical method to fabricate a variety of nanotubes for many potential applications. For instance, by conformal coating of Al on the wall of a silicon nanopillar (Fig.5.1c), followed by selective silicon etching, Al nanotubes can be fabricated. Similarly, SiO<sub>2</sub> nanotubes can be fabricated by conformal coating of SiO<sub>2</sub> on the walls of silicon nanopillars using ALD [62].

The nanotextured surfaces usually have a superhydrophobic characteristic. The hydrophobicity of the surface of the as-fabricated Si nanotubes has been evaluated. It has been found that the surface of the freshly fabricated nanotubes assume super-hydrophobicity with a typical water contact angle of  $170^{\circ} \pm 1^{\circ}$  (Fig. 5.6A). Hence, the nanotube-based surface offers a new type of platform for water protection from surface erosion, anti-fouling applications in both industrial and biological processes. On the other hand, the superhydrophobic characteristic of the nanotubes is not a favorable property for loading various solution-based materials into the nanotubes for drug delivery or cell transfection. In order to efficiently load the solution-based materials (e.g., drug, biological molecules, etc) into and thus fill nanotubes, ideally the surface of the nanotubes should be hydrophilic. It has been found that after oxygen

plasma treatment and/or being washed ultrasonically in piranha, the surface of samples is rendered to be superhydrophilic with a water contact angle of  $5^{\circ} \pm 1^{\circ}$  (Fig. 5.6B). This property indicates the feasibility to use Si nanotubes to load biological samples or drugs, which is under research for drug delivery and cell-transfection in our lab.

The nanotextured surface also can enhance the optical trapping. It has been demonstrated that optimized nanopillar surface can achieve 0.5% reflectance. The reflectance can be further reduced up to 50% by adding nanomaterials to fill the air space among the nanopillars as aforementioned in chapter 3. The optical trapping properties of the as-fabricated Si nanotube surface have been evaluated. For comparison, three types of the samples have been prepared. One sample (S1) is a flat silicon surface. The second sample (S2) is a silicon nanopillar-surface. The third sample (S3) is a silicon nanotube surface. The average diameter and height for both the nanopillars and nanotubes are the same for meaningful comparison, which are  $\sim 400$  nm and  $\sim 500$  nm, respectively. The measurement setup is schematically shown in the inset of Fig. 5.6C, which is used to measure the reflectance when the light is incident on the surface of the sample perpendicularly. The measured reflectance for all the three samples is shown in Fig. 5.6C. As shown, the reflectance from sample S2 (Si nanopillar-surface) is reduced significantly compared to that from a flat silicon surface. For the sample S3 (Si nanotube-surface), the reflectance has been further reduced dramatically. Specifically, the reduction of the reflectance for sample S3 is  $\sim 94.9\%$  compared to sample S1,  $\sim 81.3\%$  compared to sample S2. These measurements indicate that the Si nanotube surface is an excellent optical trapping nanostructure, which could improve the solar energy conversion efficiency if it could be integrated with solar cells. It should be noted that by optimizing the nanopillar alone, the

reflectance from an optimum nanopillar-surface can be as low as 0.5% compared to that of a flat silicon surface. Since the nanotube surface can further reduce the reflectance dramatically, hence, it might be possible to render the reflectance approaching zero by optimizing the nanotube surface on top of the optimized nanopillar surface.

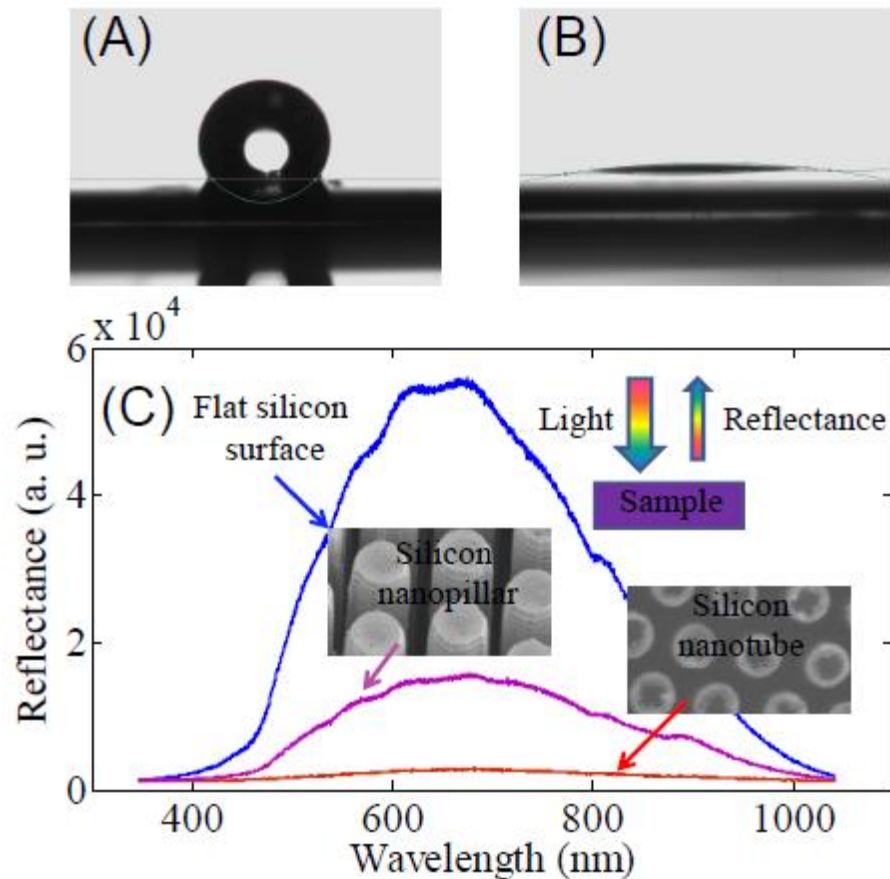


Figure 5.6 (A) the measured water contact angle is  $170 \pm 1^\circ$  for the as-fabricated Si nanotube surface; (B) the measured water contact angle is  $5 \pm 1^\circ$  after oxygen plasma treatment and/or being washed by piranha solution; (C) the measured optical reflectance from flat silicon, Si nanopillar surface, and Si nanotube surface

#### 5.4 Conclusions

In summary, fabrication of silicon nanotubes has been demonstrated by a room temperature Bosch process using nanosphere beads as the mask. The dimensions of the silicon

nanotubes can be tuned by modifying the process parameters. Besides its compatibility with the well-established semiconductor process, the simplicity and cost-effectiveness of this technique may offer a new inexpensive technical approach to fabricate nanotubes of different dimensions from a variety of materials such as semiconductors, oxides and metals. These nanotubes could be used for many different applications in life science, biomedical engineering, nanomedicine, and renewable energy.

## CHAPTER 6 ICP ETCHING TECHNOLOGY: GENERAL ANALYSIS AND DISCUSSION

In the first two chapters, the physics of plasma and the mechanisms of ICP etching were introduced in detail. In Chapters 2 through 5, modified Bosch processes were developed to fabricate a series of high aspect ratio silicon nanostructures. Based on these experiments, the results suggest that one small change of plasma conditions may cause totally different experimental results since the process highly depends on different characteristics of ions and radicals. In general, radical and ion concentration controls the reaction rate, and ion energy controls the degree of anisotropy. However, engineers prefer to understand how these features change within separated parameters, such as the reaction chemicals used, reaction temperature, chamber pressure, F/C ratio, duration of each cycle, etc. Unfortunately, one simple rule for all experiments does not exist as results may vary depending on different substrate features, chemical types, or even ICP facilities. General guidelines for certain types of experiments, however, can be suggested.

The following analysis is based on the multi-pulse DRIE, or, more specifically, the two-pulse Bosch process operated on the Alcatel ICP system. Feature size varies from 300 nm to 3  $\mu\text{m}$ . The aspect ratio of the silicon nanostructure is up to 30:1.

### 6.1 Physical Parameters

1. The pressure of the reaction: Chamber pressure is controlled by setting the position of the VAT valve and changing the reaction gas flow rate. The detailed mechanical structure of the chosen facility was introduced in Chapter 2. Reducing the pressure

lowers the density of the ions and electrons, causes longer mean free path length, and increases vertical ions bombardment. Hence, the DRIE process is more anisotropic. More obviously, lower density of the ions and electrons means fewer reaction species arrive at the substrate surface at a certain period of time, causing lower reaction speed for the etching process. In addition, the reaction byproducts are more volatile and easier to remove from the substrate surface at lower pressure. Since re-deposition of byproducts (passivation material) in the Bosch process has a larger risk of introducing polymer contamination, experiments operated at lower pressure normally show relatively clean results. The tendency to reduce polymerization can reduce selectivity as well, which may cause mask damage or introduce undercutting issues.

2. Substrate bias/platen power: Increasing bias voltage generates a higher electric field near the substrate surface. The ions diffused to this area accelerate faster and bombard the substrate with higher energy, creating a more reactive substrate surface for a high-efficiency chemical reaction and increasing the etching rate. The etching process becomes more anisotropic as the ions approach the substrate from a more vertical angle, due to the high electric field attraction. Ions with higher energy also sputter away passivation layers more efficiently, reducing the polymerization for Bosch process and leading to a less selective etching process. Even though high-energy bombardment benefits experimental results through removing passivation layers efficiently, it also introduces potential difficulties. Increased ion energy may introduce high-energy passivation material particles during bombardment. For the high aspect ratio Bosch

process, the sputtered high-energy particles may attach to the sidewall and reduce uniformity.

3. ICP source power: One large advantage of ICP over CCP is separate control of bias voltage and ICP source voltage. Engineers have more freedom to adjust ions' energy and plasma density, since these two parameters are not coupled on an ICP system. An increase of ICP power produces a large number of electrons with higher energy for ionization, which can create higher density ions, electrons, and radicals. More reactive species are applied to the substrate surface, which leads to a higher etching speed.
4. Temperature: Process temperature is controlled by liquid nitrogen and a digital heater, as mentioned in Chapter 2. Helium flow is used to improve the thermal transfer between substrate holds and process samples to ensure efficient temperature control. Furthermore, passivation material is less volatile at lower temperatures, leading to a tendency to increase polymerization. Thus the etching process turns out to be more selective at lower temperatures. The cryogenic process is a practical example of a low-temperature process application. Operating at -120 centigrade, the products from chemical reactions are involatile. These products can be served as self-formed passivation layers to protect sidewalls, leading to high aspect ratio silicon etching.

## 6.2 Chemical Composition

1. F/C ratio: The two-pulse Bosch process was introduced to achieve a vertical sidewall and high aspect ratio features by alternatively applying passivation pulses and etching pulses. The passivation-to-etching ratio is a critical parameter for the Bosch process and is easy to control by varying the cycle time. Fluorine-based deep RIE normally uses gases

containing fluorine during etching and use gas containing carbon during passivation. The fluorine-to-carbon ratio in the Bosch process is a key parameter. Since the value of this ratio can dominate the process in many ways, it should always be considered first when engineers design an experiment utilizing the Bosch process.

First of all, failure to choose the proper F/C ratio may cause etching to cease. Generally, with an F/C ratio above 3, a Bosch process etches silicon efficiently. With an F/C ratio lower than 2, passivation polymers start to integrate on the substrate surface. Genis, Turon, et al. show the F/C ratio for different etchant gases on different applied voltages in Figure 6.1. Bias power affects the etching/polymerization tendency by increasing ion bombardment energy, leading to polymer sputtering. Second, reducing F/C ratio increases process selectivity. Take Photoresist 1813s mask as an example: the PR consumption can be supplemented by the polymer re-deposition. Generally, a process operating in the etching region, but close to the polymerization region, is preferred. Third, a relatively low F/C ratio is the reason for black silicon formation, discussed in Chapter 4. Last but not least, the sidewall profile highly depends on the F/C ratio. As carbon ratio increases, the thickness of the passivation layer on the sidewall increases. The following etching cycle cannot provide enough fluorine radicals to completely remove the polymer on the sidewall, leading to a positive tapered profile.

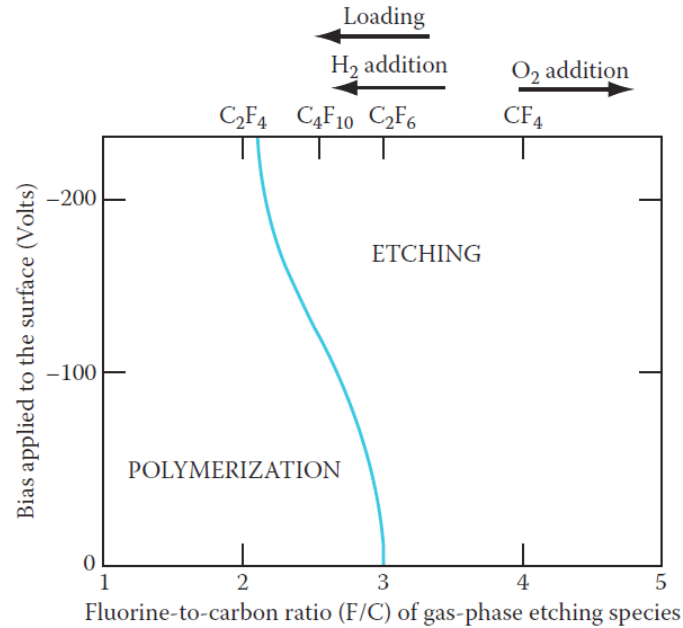


Figure 6.1 F/C ratio for different etchant gases on different applied voltages. [1]

2. Cycle time: Increasing the cycle time, while keeping the passivation-to-etching ratio at a constant value affects the etching profile as well. Since fluorine radicals react to silicon and remove silicon atoms from both vertical and horizontal directions, each single etching cycle can be treated as an isotropic etching process. Increasing the cycle time will significantly increase the etching depth for each cycle in both vertical and horizontal directions, leading to a rough sidewall or so-called “scalloping”. [12] The scalloping effect is difficult to avoid, but can be reduced by using short cycle times. However, compromises must be made since etching rates will be reduced as well. ICP systems also require a certain period of time to switch between two cycles, known as “process overlap” [12]. Typically, it can take up to one second to pump out one type of gas and flow into the other. Further reducing pulse time for each cycle may cause issues of instability for the entire process since overlap may dominate the process.

3. Additives: Two types of additives are normally used to adjust the reaction process. The first type of gas is chemically reactive, such as oxygen or hydrogen. This kind of gas affects the reaction by changing the F/C ratio due to its reaction with fluorine or carbon. For instance, adding oxygen to a carbon- based gas leads to the formation of CO and CO<sub>2</sub>, increasing the F/C ratio, and thus the etching rate. The other type of additive used is inert gas. Some inert gases with low ionization potential, such as argon (15.7ev) and helium (25ev), can help stabilize plasma since they are easy to ionize. Inert gas also affects the reaction process by introducing more high-energy ions for physical bombardment. For certain experiments, engineers prefer to etch silicon slowly since it can be difficult to control the high-speed etching process for small. By adding inert gas, the etching rate is reduced; this is referred to as inert gas dilution.

### 6.3 Conclusion

Starting with plasma physics analysis, we introduced the ICP etching system's working principles and reaction mechanisms in detail. Using modified DRIE etching processes integrated with NSL technology, a series of high aspect ratio silicon nanostructures, such as silicon pillars, silicon forests and silicon nanotubes, were successfully fabricated. Nanomaterial grafted-nanopillar antireflection surfaces and a nanoforest-based SERS substrate have been demonstrated. Furthermore, a new simple process, developed for fabricating silicon nanotubes at room temperature, based on the Bosch process, has been documented, offering a unique platform for many potential innovative applications.

## CHAPTER 7 INTRODUCTION TO PATTERNED ANODIC ALUMINUM OXIDE (AAO) BASED BIOSENSOR

### 7.1 Introduction to AAO Biosensor

Micro- and nanotechnologies enabling optical techniques for label-free biodetection have been developed extensively over the past decades and show great promise for a variety of applications, spanning from biomedical engineering, security, and environmental monitoring, to point-of-care diagnostics [63–65]. Some widely used optical techniques include surface plasmon resonance (SPR)[66], surface enhanced Raman spectroscopy (SERS) [67], localized SPR [68], light scattering [69–70] photonic crystals [71], nanoholes [72], opto-fluidic ring resonators [73], and microring resonators [74].

One category of label-free bionanosensors is enabled by nanopore structures as thin film reflective interferometric devices [75–76]. Recently, white-light source operated polymer-based Fabry-Perot interferometer (FPI) chips and polymer-based nanostructured Fabry-Perot interferometer (FPI) chips were developed for biodetection [77–78], offering potentially powerful label-free technical platforms for the detection of protein/cancer biomarkers. For instance, nanostructured FPI chips have been demonstrated to detect the prostate cancer biomarkers' free prostate-specific antigen (f -PSA) at a femtomolar concentration of 140, indicating its great potential for early stage detection of various diseases.

If a large scale of nanostructure FPI devices can be batch-fabricated on a single chip, multiplex biodetection can be readily achieved. This feature is particularly attractive for identifying an unknown disease from biofluids and screening tests, and finding a drug from

many different candidates. However, it is quite challenging for all the reported nanopore-based (both thin film devices and FPI chips) interferometric biosensors to fulfill these requirements. For instance, porous silicon is fabricated from p-type silicon using an electrochemical etching process [82]. Similarly, anodized aluminum oxide (AAO) nanopores are fabricated from Al foil thin film (typically 1.0 mm thick, purity 99.998%) using two-step anodization process. The fabrication processes of both types of nanopores are not compatible with the batch-fabrication process offered by the standard microfabrication process. Hence, it is difficult to fabricate many separated and arrayed, but still densely arranged nanopore-based devices and nanostructured FPI devices on a single chip, since the nanopores can be only fabricated on a larger piece of Al foil thin film or a silicon wafer.

Another very important issue related to current technologies is that both silicon and AAO nanopore layers for thin-film devices, or nanopore layers anchored inside the FPI cavity, are not optically transparent [75 – 80]. As a result, the transducing signals from these devices or microchips are the reflected interference fringes. While it is not too inconvenient or problematic for measurements on one single device, it is becoming increasingly challenging for measurements on large-scale arrayed devices, which are key for achieving multiplex detection with high throughput. This is due to the fact that the specifically designed optical probes for reflected signals measurement are not only expensive, but also difficult to arrange for simultaneous optical testing of a large number of devices [75–80]. In contrast, if the nanopore-based (both thin film and FPI devices) interferometric biosensors can be made transparent, meaning the transducing signals are the transmitted interference fringes, all aforementioned issues can potentially be resolved.

## 7.2 Introduction to AAO Pattern Fabrication

To address these issues, a batch-fabrication process to enable a microfabrication process for arrayed optically transparent nanostructures on a chip should be developed. Recently techniques have been developed to fabricate AAO patterns by utilizing a dry etching or an ion-milling process after the AAO has been fabricated [83]. However, this kind of approach is relatively expensive and difficult to scale up for high-volume production. Other work has been reported to fabricate the AAO from Al thin film deposited on a variety of solid substrates [84–98], which indicates the possibility to render an AAO fabrication process compatible with a standard top-down lithography-based micro- or nanofabrication process. However, to the best of our knowledge, most of the reported efforts have been only focused on wafer-scale level AAO fabrication, and very little work has been reported to fabricate AAO nanostructures from lithographically patterned Al thin film on a substrate. This is a crucial step to allow AAO nanostructures to be integrated with microdevices or microfluidic devices, thus constructing a variety of integrated micro- or nanodevices and systems for some specific applications. In addition, the thickness of the AAO nanostructure layer, which will determine the numbers of optical interference fringes, is one of the key parameters to fabricate an AAO nanostructure-based Fabry-Perot interferometer (FPI). However, essentially no work has been done to evaluate the effect of the thickness of the AAO nanostructure layer, especially for the AAO nanostructures fabricated from a lithographically-patterned Al thin film on a substrate.

In this article, we report for the first time the fabrication of a lithographically patterned and optically transparent AAO nanostructures on ITO glass substrates, which can be easily scaled up and integrated with other microdevices or microfluidic devices. We also analyze the

effects of the thickness of the AAO nanostructure layer, and the size of and interspacing among nanopores on its optical properties.

## CHAPTER 8 FABRICATION AND CHARACTERIZATION OF LITHOGRAPHICALLY PATTERNED AND OPTICALLY TRANSPARENT ANODIC ALUMINUM OXIDE (AAO) NANOSTRUCTURE THIN FILM

Modified from a paper published in  
*The Journal of Nanoscience and Nanotechnology*

Yuan He, Xiang Li and Long Que

Optically transparent anodic aluminum oxide (AAO) nanostructure thin film has been successfully fabricated from lithographically patterned aluminum on indium tin oxide (ITO) glass substrates for the first time. This indicates the feasibility to integrate AAO nanostructures with microdevices or microfluidics for a variety of applications. Both one-step and two-step anodization processes using sulfuric acid and oxalic acid have been utilized for fabricating AAO nanostructure thin film.

### 8.1 Fabrication Process Introduction

ITO glasses (Nanocs, Inc.) were used as the substrates to fabricate AAO nanostructure thin film. The measured sheet resistance of ITO is 100  $\Omega$ /sq and its surface roughness is less than 5 nm. Two acids, sulfuric acid and oxalic acid, were used for the anodization.

The proposed fabrication process flow is illustrated in Figure 8.1. This process starts from an ITO glass substrate. It is cleaned by DI water, acetone, ethanol, and DI water again for a period of 20 minutes per solution. Then a lift-off process is used to form the Al patterns. Specifically, a layer of LOR7b (Microchem, Inc.) followed by a layer Shipley PR1813, is spun on the substrate, then patterned using optical lithography. Using electron-beam evaporation, 0.5 to 2.2  $\mu$ m Al is deposited on the substrate with 10 nm Ti as an adhesion layer. Thereafter, the

photoresist is removed by immersing the whole wafer into an EBR PG (Positive Radiation Resist Edge Bead Remover) solution. As a result, Al patterns are formed and connected with each other with Al lines as shown in Step 2 in Figure 8.1. It should be noted that the Al lines connecting Al patterns are crucial for fabricating lithographically patterned AAO nanostructures, since the Al lines can warrant sufficient current flow inside the Al patterns during the anodization steps. Experiments found that the width of the Al lines of 100  $\mu\text{m}$  is sufficient to completely anodize Al patterns with a size of 6 mm  $\times$  6 mm. Otherwise, if the width of the Al line is too small, the Al lines will themselves anodize, and the current will not flow through them before the anodization of Al patterns is complete. Note that if the size of Al patterns to be anodized is scaled down, the width of the Al lines connecting them should be scaled down as well. However, the exact scaling ratio still needs further study. The measured surface roughness of the lithographically patterned Al thin film is in the range of 6–12 nm, which is smooth enough for carrying out the anodization process and forming AAO nanostructures. In contrast, surface mechanical and chemical polishing steps are usually required and necessary for fabricating AAO from an Al foil [89–102].

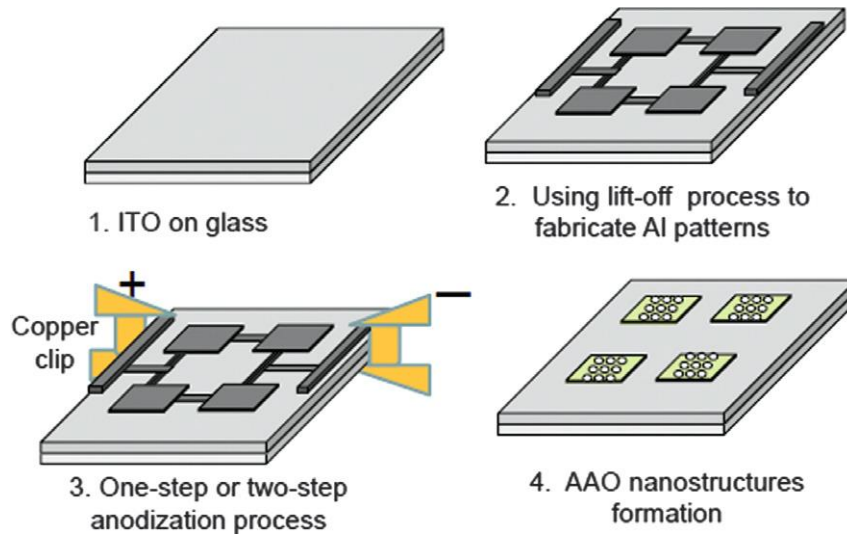


Figure 8.1. Fabrication process flow of arrayed optically transparent AAO patterns on an ITO glass substrate: (1) A clean ITO glass substrate; (2) Al patterns fabricated using a lift-off process; (3) AAO nanostructure thin film formed using a one- or two-step anodization process; (4) Al lines removed and AAO nanostructure thin film cleaned by acetone and DI water.

Once the Al patterns have been fabricated and cleaned with acetone, ethanol, and DI water, one-step and/or two-step anodization has been carried out to form AAO nanostructures as shown in Step 3 in Figure 8.1. For this study, the samples were anodized in an acid solution (either 0.3 M Oxalic acid at 2 °C at 50 V, or 0.3 M Sulfuric acid at 2 °C at 17 V) for 10–15 minutes (the first step of anodization) through copper clips. Then the anodized oxide layer alumina was etched by immersing the samples into a mixture of phosphoric acid (0.4 M) and chromic oxide (0.2 M) at 65 °C for 10 minutes or 60 minutes. Then the second anodization step was carried out for 30–45 minutes under the same conditions as the first anodization step. Thereafter, all the samples are rinsed rigorously using DI water before measurements.

## 8.2 Results and Discussion

### 8.2.1 Fabricated AAO Nanostructure

Some photos of the lithographically patterned and optically transparent AAO nanostructures are shown in Figure 8.2. In Figure 8.2(a), the AAO nanostructure thin film is fabricated, using only a one-step anodization process on a wafer-scale ITO glass substrate and oxalic acid for anodization. The AAO nanostructure thin film is optically transparent, as demonstrated by the visible sentence underneath the film, indicating that the 10 nm Ti layer has also been anodized and oxidized as transparent TiO<sub>2</sub> [85–98]. Figure 8.2(b) provides an image of AAO nanostructure thin film fabricated from lithographically patterned aluminum thin film, using a two-step anodization process and sulfuric acid for anodization. The printed numbers and letters can be clearly seen through the AAO nanostructure thin film, indicating its optical transparency, even though the degree of transparency is lower than that of ITO glass on the same substrate. For comparison, the Al thin film which is not anodized on the same substrate and totally opaque is shown in Figures 8.2(a) – (b).

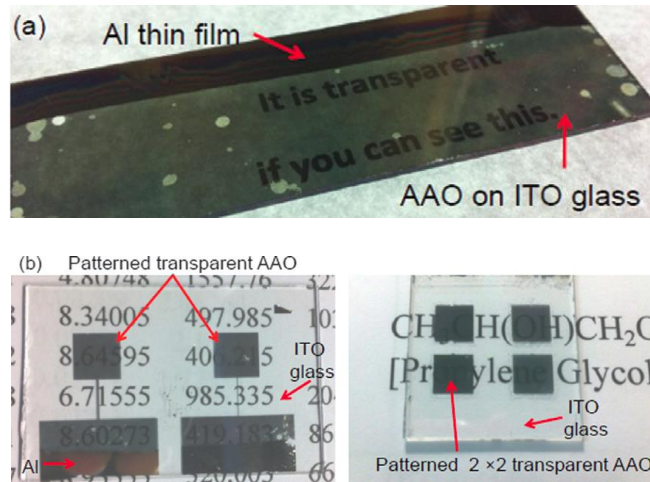
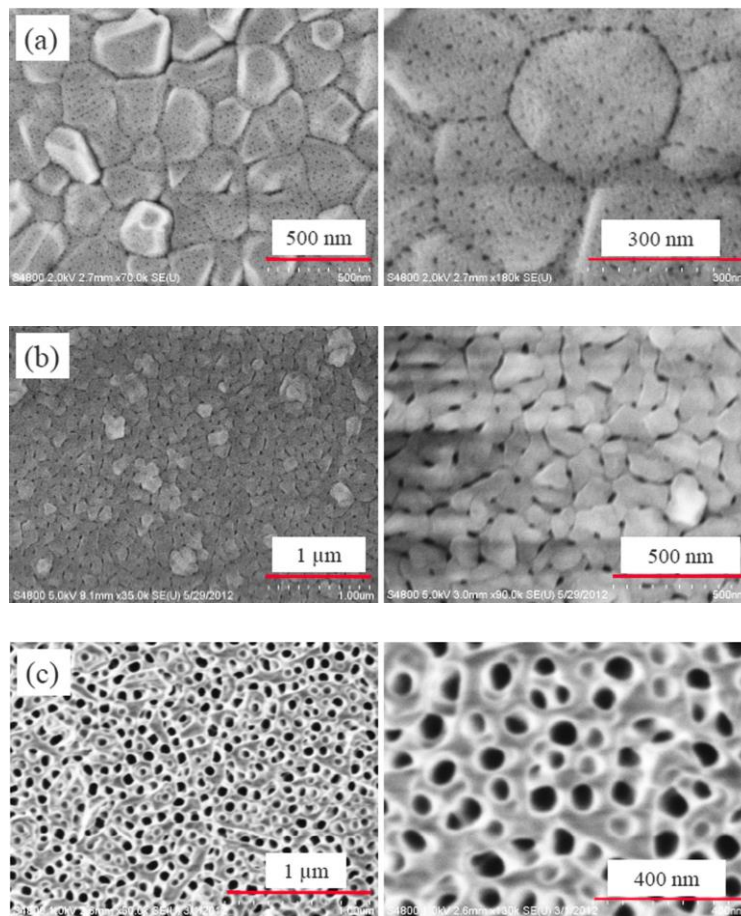


Figure 8.2. Photos showing (a) wafer-scale AAO nanostructure thin film fabricated on ITO glass; (b) transparent AAO patterns fabricated from lithographically patterned Al thin film. Non-anodized Al thin film is completely opaque on the same substrate. The size of each patterned  $2 \times 2$  transparent AAO nanostructure thin film is  $6 \text{ mm} \times 6 \text{ mm}$ , which can be readily scaled down to 10 s or 100 s of micrometers lithographically before anodization.

A scanning electron microscope (SEM, HITACHI, S-4800) was used to examine all the fabricated samples. The SEM images of the fabricated AAO nanostructure thin film on ITO glass substrates under different process conditions are given in Figure 8.3. Figure 8.3(a) gives the image of AAO nanostructures formed by a one-step anodization process using sulfuric acid. In this case, the alumina nanoscale grains in the film can still be clearly observed. In other words, the Al thin film is actually not an extended and continuous thin film; rather, it contains many Al nanoscale grains with sizes in the range of 100 nm to 500 nm before anodization. Figure 8.3(b) provides an image of AAO nanostructures formed by a one-step anodization process using oxalic acid. The nanopores are even more sparsely distributed in the alumina nanoscale grains than those in Figure 8.3(a). As shown in Figures 8.3(a) and (b), the nanopores after one-step anodization are rather sparsely distributed in the alumina nanoscale grains and do not have a high degree of periodicity. In order to obtain the average nanopore size, the interspacing and

related standard deviation of the AAO nanopores fabricated under different experimental conditions, and the nanopore size of 100 nanopores and the interspacing among them have been measured based on the scale bars shown in the SEM images. The average nanopore size and interspacing are relatively larger for AAO nanostructures anodized by oxalic acid ( $30 \pm 5$  nm for nanopore size, and  $125 \pm 5$  nm for the interspacing) than those anodized by sulfuric acid ( $10 \pm 2$  nm for nanopore size, and  $35 \pm 2$  nm for the interspacing). The SEM images of AAO nanostructures fabricated using a two-step anodization process and oxalic acid for anodization are shown in Figures 8.3(c)–(d). Under this condition, the alumina nanoscale-grain domains essentially become invisible. In Figure 8.3(c), the time to remove the alumina layer after the one-step anodization process is 10 minutes, while in Figure 8.3(d), the time is 60 minutes. As can be seen, the nanopore size, the interspacing among nanopores, and overall periodicity are different for these two cases, which are summarized in Table 8.1, confirming that nanopore size and periodicity of the AAO can be tuned by using different fabrication parameters and acids as extensively reported in previous research [83–98]. Specifically, for the case in Figure 8.3(c), the alumina layer formed in the first step of anodization was only partly etched away after 10 minutes, and the nanopores formed in the second step of anodization are simply the continuation and widening of the nanopores formed in the first step. Hence, the positions of nanopores are essentially the same as those in the first step of the anodization process. But because the size of the nanopores increases, the interspacing among them decreases [94–105]. In contrast, for the case in Figure 8.3(d), the alumina layer formed in the first step of anodization was totally removed. Then hemispherical nano-patterns developed on top of the lower aluminum layer, due to the self-assembly characteristics of the anodizing process. Hence,

the nanopores formed in the second step of anodization are essentially new nanopores initiated from existing hemispherical nano-patterns, and thus are more uniform than those in Figure 8.3(c), as expected [94–105]. Thereafter, the nanopore size can be further widened if the samples are immersed in phosphoric acid ( $H_3PO_4$ ) for several to tens of minutes [94, 106]. It should be noted that the diameter of the hemispherical nano-patterns can be easily controlled from tens to hundreds of nanometers by applying a different anodization voltage and changing the composition and temperature of the anodization acids, which have been studied extensively for the past decades. Therefore the size and interspacing among nanopores can be tuned, and the AAO quality and uniformity of the nanopores can be optimized using the two-step anodization process [94–106].



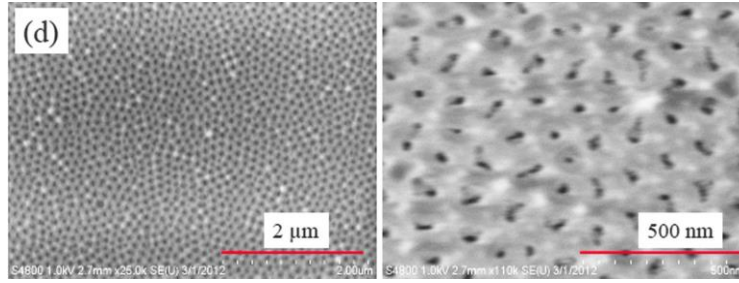


Figure 8.3. SEMs of AAO nanostructure thin film (a) fabricated using a one-step anodization process with sulfuric acid; (b) fabricated using a one-step anodization process with oxalic acid; (c) fabricated using a two-step anodization process with oxalic acid. The time to remove the alumina between the two anodization steps is 10 minutes; (d) fabricated using a two-step anodization process with oxalic acid. The time to remove the alumina between the two anodization steps is 60 minutes.

Table 8.1 The size of nanopores and the interspacing among nanopores fabricated from 2.2  $\mu\text{m}$  thick Al

One or two-step anodization	Electrolyte	Etching alumina time prior to the second step anodization (minutes)	Anodization voltage/temperature	Average pore size (nm)	Average interspacing among pores (nm)
One-step	Sulfuric acid		17 V/2 $^{\circ}\text{C}$	10 $\pm$ 2	35 $\pm$ 2
One-step	Oxalic acid		50 V/2 $^{\circ}\text{C}$	30 $\pm$ 5	125 $\pm$ 5
Two-step	Oxalic acid	10	50 V/2 $^{\circ}\text{C}$	50 $\pm$ 5	50 $\pm$ 5
Two-step	Oxalic acid	60	50 V/2 $^{\circ}\text{C}$	25 $\pm$ 2	125 $\pm$ 5

### 8.2.2 Optical Property Measurement of AAO Nanostructure

For optical property measurement, such as transmittance and reflectance measurement, of the fabricated AAO nanostructure thin film, the optical source is a tungsten halogen source (Ocean Optics, Inc.) with a spectrum covering 350 nm to 1050 nm; the spectrometer is USB4000-VIS-NIR (Ocean Optics, Inc.); and the optical fiber probe for the reflectance measurement is the Fiber Optic Reflection/Backscattering Probes (Ocean Optics, Inc.). The reflectance measurement setup on the AAO nanostructure thin film is the same as that reported in references 8, 9 and 21. For the transmittance measurement, the setup is shown in Figure 8.4 (left). The incident light beam is collimated and normally incident to the surface of

the AAO nanostructure thin film; the other lens will be used to couple the transmitted signals into an optical fiber probe, leading to the spectrometer.

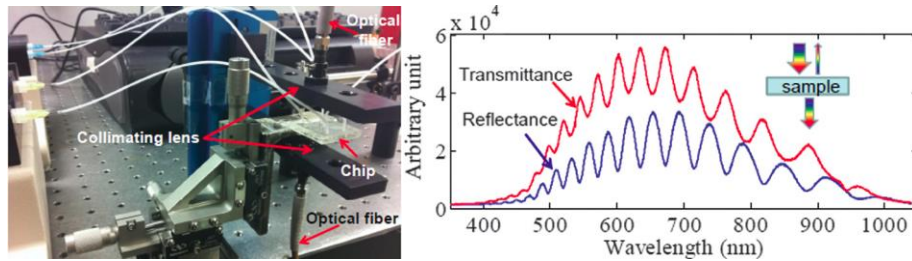


Figure 8.4. (Left) Optical setup for the measurement: a white light source is delivered to the chip through an optical fiber, the transmitted signal is collected by another optical fiber, leading to a spectrometer; (right) measurement of transmittance and reflectance signals of a 2.2  $\mu\text{m}$ -thick AAO nanostructure thin film.

Figure 8.4 (right) displays a measurement of transmittance and reflectance of one 2.2  $\mu\text{m}$  thick AAO nanostructure thin film fabricated by a one-step anodization process. As expected, the profiles of the transmittance and reflectance signals are complementary to each other in terms of the interference fringes. In other words, the interference peaks of the transmission signal always correspond to the interference valleys of the reflectance signal. Similarly, the interference valleys of the transmission signal always correspond to the interference peaks of the reflectance signal. Hence, the optical performance (e.g., finesse) of the AAO-based thin film interferometer can be evaluated by analyzing either the transmission signals or the reflection signals [97].

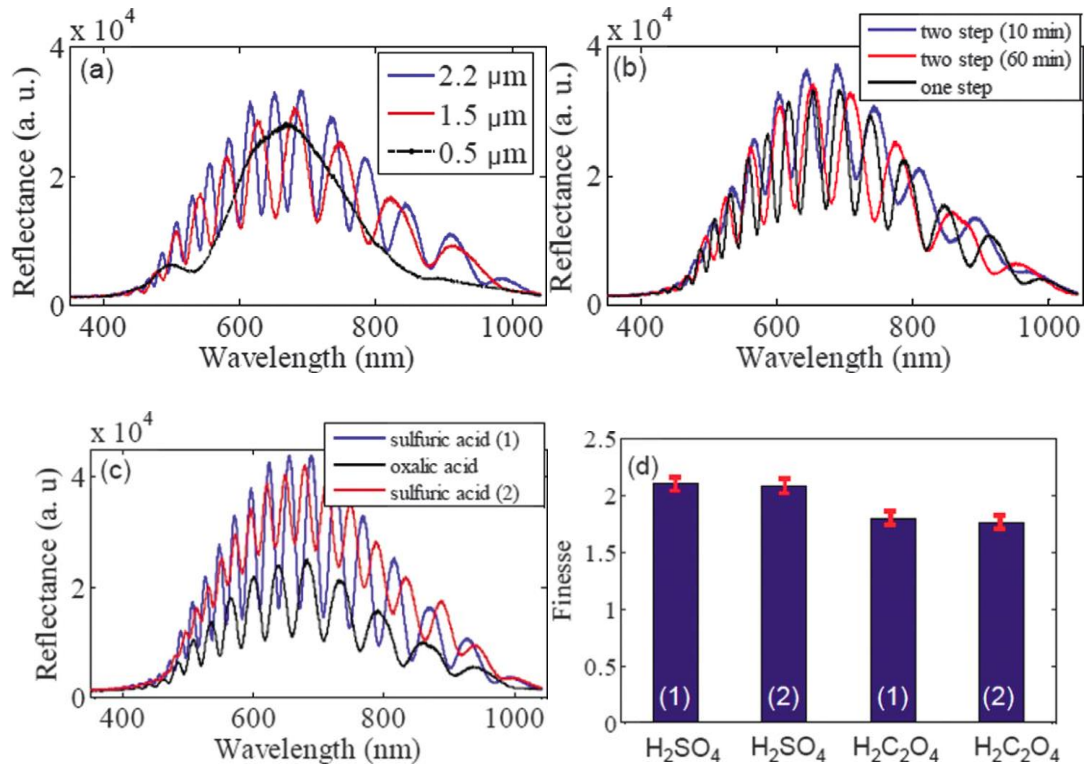


Figure 8.5. (a) Measured reflectance signals from AAO nanostructure thin film with different thicknesses of 0.5  $\mu\text{m}$ , 1.5  $\mu\text{m}$  and 2.2  $\mu\text{m}$  using a one-step anodization process in 0.3 M oxalic at 2  $^{\circ}\text{C}$  at 50 V for 15 minutes; (b) Measured reflectance signals from AAO nanostructure thin film fabricated with 1) a one-step anodization process in 0.3 M oxalic at 2 $^{\circ}$  C at 50 V for 15 minutes, 2) alumina layer etched by immersing the AAO substrate in a mixture solution of phosphoric acid (0.4 M) and chromic acid (0.2 M) at 65 $^{\circ}$  C for 10 minutes or 60 minutes, 3) a two-step anodization process in 0.3 M oxalic at 2  $^{\circ}\text{C}$  at 50 V for 45 minutes. In the plot, two-step (10 min): the alumina layer etching time is 10 minutes; or, two-step (60 min): the alumina layer etching time is 60 minutes; (c) Measured reflectance signals from AAO nanostructure thin film fabricated from Al with the same thickness of 2.2  $\mu\text{m}$ , but fabricated with different acids in a one-step anodization process. In the plot, sulfuric acid (1): 0.3 M sulfuric acid at 2  $^{\circ}\text{C}$  at 17 V for 15 minutes; sulfuric acid (2): 0.3 M sulfuric acid at 2  $^{\circ}\text{C}$  at 30 V for 15 minutes; oxalic acid: 0.3 M oxalic at 2  $^{\circ}\text{C}$  at 50 V for 15 minutes; (d) Summary of finesse of the AAO nanostructure thin film in (c) fabricated and anodized by sulfuric acid and oxalic acid.

In order to construct an AAO-based thin film interferometer, the numbers of the interference fringes of the reflectance and transmittance signals are important parameters, highly related to the thickness of the AAO nanostructure thin film. In Figure 8.5(a), the

measured reflectance signals from AAO nanostructure thin films using one-step anodization processes with different thicknesses are plotted. It should be noted that based on a series of experiments, it was found that when the thickness of AAO nanostructure thin film is 0.5  $\mu\text{m}$  or lower, no interference fringes can be observed regardless of whether the AAO nanostructure thin film is fabricated by a one-step or two-step anodization process. In contrast, the interference fringes are clearly observed by increasing the thickness of AAO thin film to 1.5  $\mu\text{m}$  (8 interference peaks) and 2.2  $\mu\text{m}$  (12 interference peaks). In other words, the number of interference peaks increases with thickness (e.g., at least in the range of 0.5  $\mu\text{m}$  to 2.2  $\mu\text{m}$ ) of AAO nanostructure thin film. Even though we have not determined the exact thickness (e.g., the threshold thickness) of AAO nanostructure thin film for the emergence of interference fringes, which should be between 0.5  $\mu\text{m}$  and 1.5  $\mu\text{m}$ , it is clear that the thickness cannot be below or equal to 0.5  $\mu\text{m}$ , but should be large enough (e.g., 1.5  $\mu\text{m}$ ) to construct an AAO nanostructure thin film interferometer.

As shown in Figure 8.3 and in Table 8.1 and previous research [83–98], by changing the anodization process parameters (e.g., anodization voltage, acids) or using one- or two-step anodization processes, the pore size and interspacing among pores will change. Figure 8.5(b) gives the measured reflectance signals of AAO nanostructure thin films fabricated with one-step and two-step anodization processes. For these three samples, the thicknesses of the lithographically patterned Al thin film are the same, 2.2  $\mu\text{m}$  before anodization. After one-step anodization, the thickness has little change and is still 2.2  $\mu\text{m}$  but is reduced to 1.9  $\mu\text{m}$  after two-step anodization. In this case, measurements found that the reflectance signals have similar basic profiles (e.g., reflectance intensity) even though the pore sizes, the interspacing

among them and the thickness of the nanostructure thin film have some variations. One consistent difference was found: for samples with one-step anodization, the number of interference peaks is 12. After two-step anodization, the number of interference peaks is reduced to 9, since the thickness of AAO nanostructure thin film is reduced from 2.2  $\mu\text{m}$  to 1.9  $\mu\text{m}$ .

In Figure 8.5(c), the reflectance signals of AAO nanostructure thin film fabricated from Al using a one-step anodization process with the same 2.2  $\mu\text{m}$  thickness and sulfuric and oxalic acid are plotted. During oxalic acid anodization, the temperature is 2° C and voltage is 50 V. During sulfuric acid anodization, the temperature is 2° C and the voltage is 17 V and 30 V, respectively.

It is well known that finesse is a critical parameter to determine the resolving power of a Fabry-Perot interferometer, which is defined as:  $F = \text{FSR}/\delta\lambda$ , [20] where FSR is the free spectral range, and  $\delta\lambda$  is the full-width half maximum. By examining the optical signals (e.g., interference fringes) in Figure 8.5(c), it is clear that the average finesse of the AAO nanostructure thin film fabricated by sulfuric acid is bigger than that fabricated by oxalic acid. The finesse measurements on several samples are averaged and summarized in Figure 8.5(d). The average finesse is  $2.09 \pm 0.05$  for AAO thin film samples fabricated by sulfuric acid, and the finesse is  $1.79 \pm 0.05$  for AAO thin film samples fabricated by oxalic acid. As shown in Table 8.1, the nanopore size and interspacing among nanopores are different for AAO nanostructure thin film fabricated by one-step anodization using sulfuric and oxalic acid, thereby resulting in a different finesse. The bigger the finesse offered by the AAO nanostructure thin film, the higher the sensitivity for this type of thin film-based interferometer [96]. It should

be also noted that the size of the lithographically patterned AAO nanostructure thin film can be readily scaled down to 10 s or 100 s of micrometers from those shown in Figure 8.2. Hence, this fabrication technology can be used to integrate AAO nanostructures within microdevices or microfluidic devices for a variety of applications, including applications in the emerging field of optofluidics.

### 8.3 Conclusion

In summary, optically transparent AAO nanostructure thin film has been fabricated successfully from lithographically patterned Al thin film, indicating the feasibility of integrating AAO nanostructures within microdevices or microfluidic devices for a variety of specific applications. The nanopore size and the interspacing among nanopores of AAO nanostructures can be tuned by changing the anodization parameters. Experiments found that the thickness of AAO nanostructure thin film is critical to construct an AAO thin film-based interferometer, and changing both nanopore size and interspacing can optimize its optical sensitivity. Since the size of patterned AAO thin film can be easily scaled down to 10 s and 100 s of micrometers, large-scale arrayed and patterned AAO nanostructure thin film can be fabricated on a single chip, thereby enabling the feasibility for large-scale arrayed label-free biosensing platforms for high throughput applications. More systematic studies need to be carried out in order to optimize the design of an AAO nanostructure thin film sensor with higher sensitivity and resolution.

## CHAPTER 9 A TRANSPARENT AAO NANOSTRUCTURED OPTICAL BIOSENSOR

Modified from a paper published in  
*The Journal of Biomedical Nanotechnology*

Yuan He, Xiang Li and Long Que

Herein we report a new transparent nanostructured Fabry-Perot interferometer (FPI) device. The unique features of the nanostructured optical device can be summarized as the following: (i) optically transparent; (ii) simple and inexpensive for fabrication; (iii) easy to produce and scale up as an arrayed format. These features overcome existing barriers for the current nanopore-based interferometric optical biosensors by measuring transmitted optical signals rather than reflected optical signals, thereby facilitating optical testing for the arrayed biosensors and thus paving the way for their potential for high throughput biodetection applications. The optically transparent nanostructures (i.e., anodic aluminum oxide nanopores) inside the FPI devices are fabricated from 2.2  $\mu\text{m}$  thick lithographically patterned Al thin film on an indium tin oxide (ITO) glass substrate using a two-step anodization process. A bio-reaction between biomolecules was facilitated utilizing the binding between Protein A and porcine immunoglobulin G (IgG) as a model. Experiments found that the lowest detectable concentration of proteins using current devices is at the picomolar level, which can be tuned to the femtomolar level by optimizing the performance of the FPI device.

## 9.1 Device and Experiment Design

### 9.1.1 Device Fabrication

The fabrication processes of the new FPI devices are as outlined below. The first step, fabrication of the transparent nanostructures (AAO nanopores) from the patterned Al thin film, has been discussed in detail in Chapter 8. The second step, fabrication of a PDMS microfluidic chip using soft lithography, is as follows. A 50  $\mu\text{m}$  thick SU-8 mold of the device is formed on a silicon substrate using optical lithography. PDMS is casted on the mold, followed by 1.5 hour curing at the temperature of 65°C. Then the PDMS microfluidic layer is bonded with the ITO glass with patterned AAO layer after oxygen plasma treatment for 10 seconds. The sample input and output holes are made in the PDMS layer thereafter for the delivery of the chemical samples to the nanostructured-FPI devices, followed by assembling input and output tubing (Upchurch Scientific, Inc.), which is connected with a syringe controlled by a syringe pump (KD Scientific, Inc.). It should be noted that the AAO nanopore patterns should be totally covered by the FPI cavity in order to ensure that the PDMS microfluidic layer can directly be bonded to the ITO glass substrate, thus avoiding any liquid leakage during the operation of the nanostructured FPI chip.

### 9.1.2 Experiment Design

Figures 9.1(a)–(b) illustrate the schematic and operational principles of the transparent nanostructured FPI chip. Each device consists of a PDMS plate and a nanopore layer, which is fabricated on an indium tin oxide (ITO) glass substrate. The average size of nanopores is in the range of 20 nm to 50 nm in diameter, which can be varied by changing the parameters of the process, and the gap size of the  $\mu\text{FP}$  cavity is 50  $\mu\text{m}$ . The optical transducing signal is the

transmitted optical interference signal from the nanostructured FPI device when a collimated white light is normally incident. Each device on the chip is connected with an addressable microfluidic network, which can provide the samples to each device and can also be used to rinse the device. All devices on the same chip can share the same white light optical source, which will simplify the optical setup significantly compared to the reflective biosensor configuration [75–80]. The close-up of one nanostructured FPI device is shown in Figure 9.1(b).

When the biomolecules are immobilized on the nanostructures and the binding between biomolecules occurs, the fringes of the transmitted signals will shift, due to the change of the effective refractive index inside the cavity. The nanostructures inside the FPI cavity will increase the binding sites of the biomolecules, and, therefore, the sensing surface area will increase up to at least two orders of magnitude larger than that of a conventional FPI with a planar surface inside its cavity. In this case, the sensing surface area includes the top and bottom surfaces of the nanopore layer and the nanopore sidewalls. In the experiments, the optical source is the same tungsten halogen lamp as in Chapter 8. The transmitted optical signals from the nanostructured FPI device are coupled to a spectrometer, which is connected to a laptop computer for data acquisition and processing. The samples are transported to the device through the assembled plastic tubing by syringe pumps.

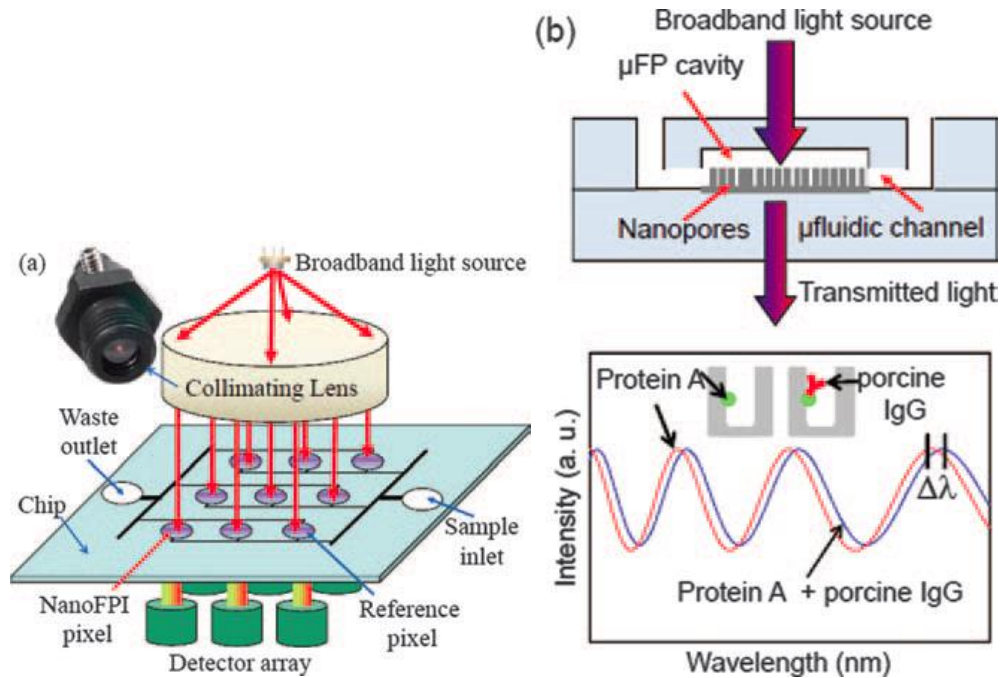


Figure 9.1. (a) Schematic of a transparent nanostructured FPI microchip, consisting of arrayed nanostructured FPI devices; each device is addressable by the integrated microfluidic channels for sample delivery; all the devices can share the same expanded white light source as the input light, and the transducing signals from the devices are the transmitted interference signals from each device; (b) Close-up of a nanostructure FPI device showing the nanostructures (i.e., nanopores) inside the cavity of a FPI: the immobilization of biomolecules (i.e., protein A) on the surface of the nanostructures and the binding between biomolecules (i.e., protein A and porcine IgG) change the effective index of refraction, thus causing a shift of the transmitted interference fringes.

## 9.2 MATERIALS AND METHODS

### 9.2.1 Chemicals and Materials

Protein A and Sea Block have been purchased from Pierce Biotechnology (USA). Buffer solution phosphate buffered saline (PBS) and porcine immunoglobulin G (IgG) have been obtained from Sigma-Aldrich (USA). Specifically, Protein A is prepared in PBS (pH = 7.2) solution at a concentration of 500  $\mu\text{g/ml}$  [80], which can be diluted accordingly for different concentrations if needed. The blocking buffer, Sea Block, used to minimize the nonspecific

binding, is mixed with PBS solution with a ratio of 1:4. Similarly, the porcine IgG anti-sera are diluted with PBS to achieve final concentrations of 100000, 10000, 1000, 100, 10 and 1 ng/ml, respectively, for the technical demonstrations.

### 9.2.2 Biodetection Procedure

The experimental procedure for the binding between Protein A and porcine IgG is schematically illustrated in Figure 9.2. This bioassay is very selective and only specific between Protein A and porcine IgG, and hence has typically been used as a simple model for biodetection [79]. The experimental procedure is carried out as follows. The concentration of Protein A is fixed at 500 $\mu$ g/ml in the experiments. Before applying any chemicals to each device, transmission signals are obtained for each of them as a reference. Through the input, PBS is flowed into each device and the corresponding transmission signals are obtained. Then Protein A is flowed into each device and the incubation time is 30 minutes at room temperature to ensure that the AAO nanostructure surface is covered with Protein A as much as possible. As a result, Protein A binds to the AAO nanostructure and thus serves as a probe. The unbound or loosely bound Protein A is washed away using PBS for at least 3 cycles. The measurement is taken at each interval and checked for measurement repeatability. Then Sea Block is flowed into each device and incubated for 15 minutes at room temperature, again followed by three cycles of PBS rinsing. Thereafter, the concentrations of porcine IgG to be flowed into the device are 1, 10, 100, 1000, 10000 and 100000 ng/ml in a PBS solution. The experiments take place in the following order: The porcine IgG is flowed into device sequentially, from lower to higher concentrations. For instance, the porcine IgG at concentration of 1 ng/ml is flowed into the device first; after a 30-minute incubation, PBS is flowed to rinse the device three times and

measurements are carried out accordingly. Thereafter, the porcine IgG at concentration of 10ng/ml is flowed into the device for the testing. After a 30-minute incubation, rinsing and measurement are conducted. Similarly, the experiments are performed for porcine IgG at concentrations of 100, 1000, 10000 and 100000 ng/ml in sequence, respectively. All these results are obtained by averaging multiple measurements on four devices. It should be noted that all the experimental steps have been performed at room temperature, and the measurements are carried out after the devices have dried.

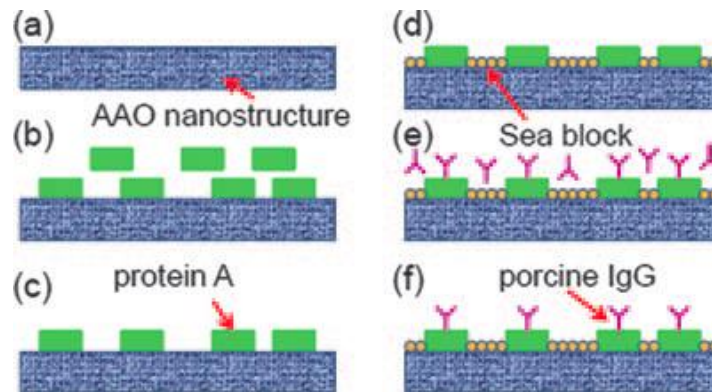


Figure 9.2. The procedure for achieving the binding between Protein A and porcine IgG: (a) PBS is flowed to rinse the AAO nanostructure; (b)–(c) Protein A is applied and incubated for 30 minutes, followed by PBS rinsing; (d) Sea block is applied to occupy the sites without Protein A, followed by PBS rinsing; (e)–(f) Porcine IgG is applied to bind with Protein A, followed by PBS rinsing. The optical measurements are carried out at each step when the device has dried.

### 9.2.3 Experimental Data Analysis

First, the optical signal (i.e., interference fringes) with the buffer (PBS) is obtained, which is used as a reference for the optical signals obtained at each bioassay step. The fringes' shift contributed by the buffer thus can be canceled. Then, the fringes' shift of the measured optical signals at each bioassay step is obtained by using the interference fringes on immobilized Protein A on the nanostructure surface as reference points. Specifically, for each porcine IgG

concentration, (i) first the shift of each interference fringe's peak after porcine IgG has been applied relative to that of the Protein A coated AAO nanostructure is obtained; (ii) then the shift of all the peaks is averaged. Similarly, the averaged shift of the fringes for different porcine IgG concentrations is obtained.

### 9.3 Results and Discussion

Experiments have found that the Au-coated AAO remains optically transparent when the thickness of the coated Au is 5 nm or lower. In addition, measurements found that at this range of thickness of Au, the intensity of the transmitted signals shows negligible change as shown in Figure 9.3(a). It should be noted that the optical transparency of the Au-coated AAO nanopore layer is very important for most of the bioassay since an Au layer (typically several nanometers) is usually required for the chemical functionalization of the sensing surface [85]. In Figures 9.3 (a) and (b), the SEM images are given for the AAO surfaces, both uncoated and coated, with a layer of 5 nm Au, respectively. It is clearly shown in Figure 9.3 (b) that a surface of AAO coated with a layer of Au contains Au nanoscale grains with sizes in the range of 10 nm to 20 nm.

The SEM images of the AAO nanostructures before and after being coated with Protein A are shown in Figures 9.4(a) and (b), respectively. As shown, the surface of the AAO nanostructures has distinct changes with the immobilized Protein A. The measured transmission signals for each device to monitor the immobilization of Protein A and the binding between Protein A and porcine IgG have been carried out, and one representative result is given in Figure 9.4 (c). The redshift of the fringes with respect to those of Protein A has been observed if the porcine IgG is bound with Protein A. The more porcine IgG is applied and bound with Protein A, the larger the redshift, as far as a sufficient amount of Protein A is available for

binding. All these measurements can be monitored in real-time, which is particularly convenient to ensure that the unbound and loosely bound molecules have been completely rinsed away.

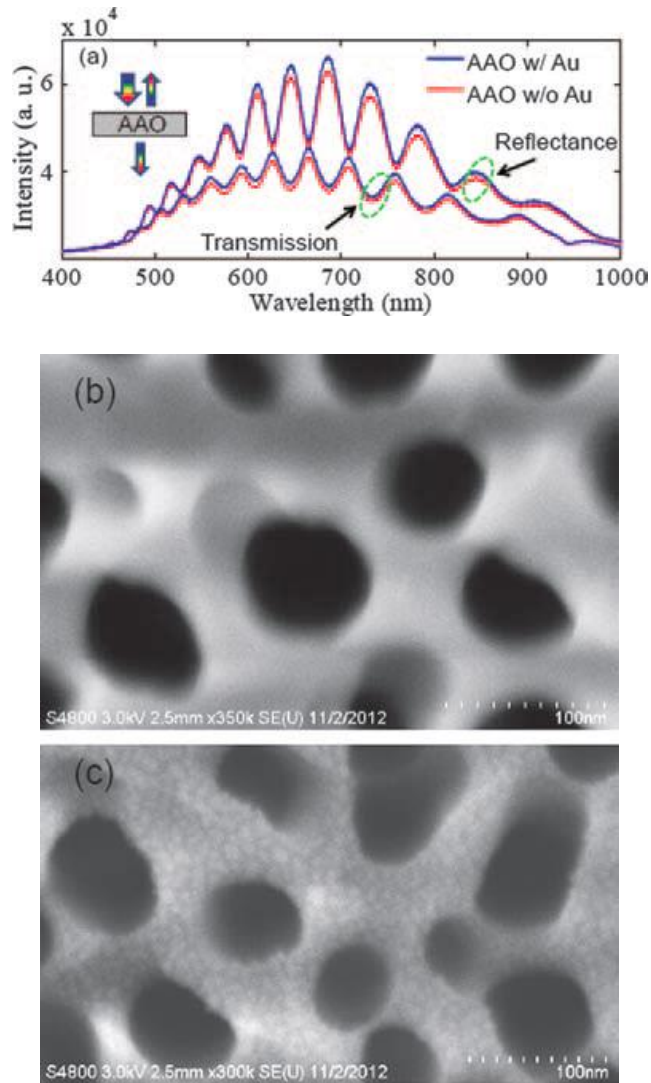
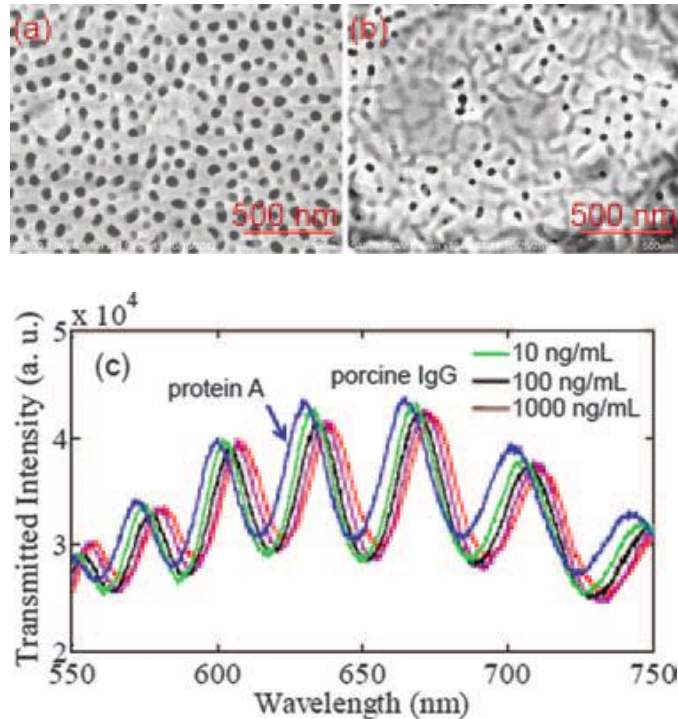


Figure 9.3. (a) A representative measured reflectance and transmission spectrum of the AAO sample fabricated with two-step anodization, with and without Au coating; SEM images show the AAO nanostructure before (b) and after (c) 5 nm Au (with 5 Å Ti as adhesion layer) coating has been applied. The Au nanoscale grains are clearly visible on the surface.

The average fringe shift under different concentrations of porcine IgG is summarized and the logarithm plot is given in Figure 9.4 (d). Error bars are standard deviation based on the

multiple measurements at each concentration of IgG. The fitting curve is created to allow the extrapolation of data points between the measured results. As expected, the lower the concentration of porcine IgG, the less porcine IgG is bound to the Protein A; hence the smaller the fringe's shift. For instance, the fringe shift is  $3.30 \pm 0.02$  nm for porcine IgG at a concentration of 10 ng/ml, which is 62.5 pM for porcine IgG. When the concentration of porcine IgG is reduced to 1 ng/ml, the fringe shift becomes  $0.80 \pm 0.02$  nm. Negligible shift is observed when the concentration becomes lower than this value. Hence, the lowest detectable concentration of current devices is  $\sim 1$  ng/ml ( $\sim 6.25$  pM), which is comparable to that of SPR-based biosensors [66]. Note that the detectable concentration can be further reduced if the thickness of the AAO layer can be increased to  $4 \mu\text{m}$  [78,79].



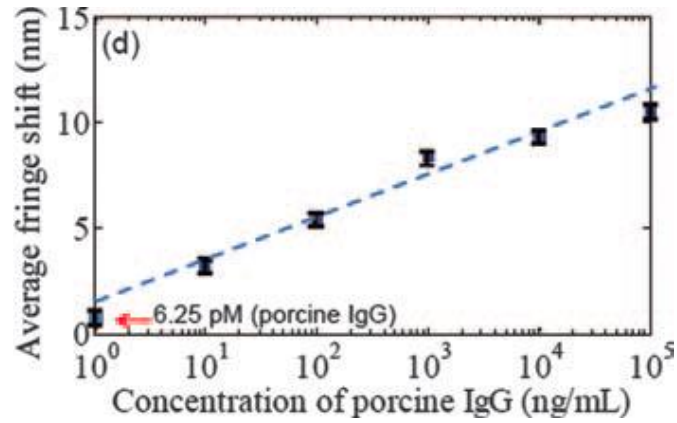


Figure 9.4. (a) SEM image of blank AAO nanostructures; (b) SEM image of AAO nanostructures with immobilized Protein A; (c) A representative measurement showing the shift of the transmitted optical fringes on the binding between Protein A and porcine IgG with different concentrations; (d) The averaging fringe shift of the optical signals on the binding between Protein A and porcine IgG of different concentrations.

## CHAPTER 10 AAO NANOSTRUCTURED OPTICAL SENSOR: CONCLUSIONS AND FUTURE WORK

### 10.1 Conclusions

The present research has successfully demonstrated fabrication of transparent patterned AAO nanostructures on an ITO glass substrate. Nanopore size and the interspacing among nanopores of AAO nanostructures can be tuned by changing anodization parameters. Experiments found that the thickness of AAO nanostructure thin film is critical to construct an AAO thin film-based interferometer and changing both nanopore size and interspacing can optimize its optical sensitivity. Since the size of patterned AAO thin film can be easily scaled down to tens and hundreds of micrometers, large-scale arrayed and patterned AAO nanostructure thin film can be fabricated on a single chip.

Utilizing this technology, arrayed transparent nanostructured FPI devices have been fabricated and tested, and their application for biosensing has been demonstrated. Specifically, using Protein A and porcine IgG as a model, the detection of the binding between Protein A and porcine IgG has been demonstrated using transparent nanostructured FPI devices. The lowest detectable concentration of porcine IgG is 6.25 pM for current devices. Finally, due to the capability to fabricate tens and hundreds of transparent nanostructured FPI microdevices on a single chip, as suggested in this paper, this new technology may provide a promising technical platform for multiplex, label-free biodetection with a highly simplified optical testing setup.

## 10.2 Future Work

The optimization of the performance of FPI devices requires systematic efforts and must overcome some fabrication technical barriers. For instance, experiments have found that the numbers of interference fringes of transmittance signals are highly related to the thickness of the AAO layer [81]. The number of interference peaks increases with the increasing thickness of the AAO layer for the same spectral range, thereby resulting in enhanced finesse [81]. However, it is challenging to routinely fabricate 3–4  $\mu\text{m}$  thick AAO layer due to the quality of Al deposited on the ITO glass using the E-Beam Evaporation System (CHA Industries, Inc.). Because of the extremely high evaporation temperature (1300–1600  $^{\circ}\text{C}$ ) of Al [98], when the crucible for holding Al target is damaged, it has to be replaced by a new crucible, hence multiple applications of the evaporation process are required in order to obtain 3–4  $\mu\text{m}$  Al. It has been found that the Al is easily partially oxidized or contaminated during this procedure. As a result, anodization cannot be carried out on the as-deposited Al successfully, and transparent AAO nanostructures of good quality cannot be formed. Finding a proper crucible may provide a solution for this. In addition, when the thickness of AAO layer becomes 4  $\mu\text{m}$  or more, the transparency of the AAO layer is reduced, and the intensity of the transmitted optical signals decreases. Increasing the size or reduce the interspacing of the nanopores may provide a solution, but this requires further analysis.

It should also be noted that even though herein only the detection of the binding between Protein A and porcine IgG as a model is reported, this platform can be easily adapted to the detection of many different biospecies, such as cancer biomarker proteins and circulating tumor cells (CTCs), by functionalizing the surface of the nanostructured FPI device with

different probes [80, 110, 111]. In addition, the lowest detectable concentration of this type of sensor is highly related to nanopore size and density, which can be optimized for further lowering the detection limit. Based on these measurements, transparent nanostructure FPI devices could offer sufficient sensitivity for the detection of clinically relevant cancer biomarkers, which are typically in the range of picomolar concentration levels or lower [63]. Furthermore, since arrayed transparent devices can be batch-fabricated in an inexpensive and efficient manner on a single chip, a disposable platform based on arrayed nanostructured FPI devices can be developed for multiplex biomolecular detection and analysis.

## REFERENCES

- [1] M. Madou, *Fundamentals of microfabrication and nanotechnology*. Boca Raton, FL: CRC Press, 2012.
- [2] J. Grym, *Semiconductor technologies*. [S.l.]: InTech, 2010.
- [3] E. Shunko, D. Stevenson and V. Belkin, 'Inductively Coupling Plasma Reactor With Plasma Electron Energy Controllable in the Range From 6 to 100 eV', *Plasma Science, IEEE Transactions on*, vol. 42, no. 3, pp. 774-785, 2014.
- [4] E. Klaassen, K. Petersen, J. Noworolski, J. Logan, N. Maluf, J. Brown, C. Storment, W. McCulley and G. Kovacs, 'Silicon fusion bonding and deep reactive ion etching: a new technology for microstructures', *Sensors and Actuators A: Physical*, vol. 52, no. 1-3, pp. 132-139, 1996.
- [5] M. Blauw, T. Zijlstra and E. van der Drift, 'Balancing the etching and passivation in time-multiplexed deep dry etching of silicon', *Journal of Vacuum Science & Technology B: Microelectronics and Nanometer Structures*, vol. 19, no. 6, p. 2930, 2001.
- [6] R. Abdolvand and F. Ayazi, 'An advanced reactive ion etching process for very high aspect-ratio sub-micron wide trenches in silicon', *Sensors and Actuators A: Physical*, vol. 144, no. 1, pp. 109-116, 2008.
- [7] J. Min, G. Lee, J. Lee, S. Moon and C. Kim, 'Dependences of bottom and sidewall etch rates on bias voltage and source power during the etching of poly-Si and fluorocarbon polymer using SF<sub>6</sub>, C<sub>4</sub>F<sub>8</sub>, and O<sub>2</sub> plasmas', *Journal of Vacuum Science & Technology B: Microelectronics and Nanometer Structures*, vol. 22, no. 3, p. 893, 2004.
- [8] Wikipedia, 'Alcatel Micro Machining Systems', 2015. [Online]. Available: [http://en.wikipedia.org/wiki/Alcatel\\_Micro\\_Machining\\_Systems](http://en.wikipedia.org/wiki/Alcatel_Micro_Machining_Systems). [Accessed: 15- Apr- 2015].
- [9] Plasmatherm.com, 'Plasma-Therm: Etch', 2015. [Online]. Available: <http://www.plasmatherm.com/etch.html>. [Accessed: 03- Jul- 2015].
- [10] Docstoc.com, 'Alcatel Model A601E Manual Substrate Handling Components and', 2010. [Online]. Available: <http://www.docstoc.com/docs/27379127/Alcatel-Model-A601E-Manual-Substrate-Handling-Components-and>. [Accessed: 06- Mar- 2011].
- [11] Cnm2.engineering.ucdavis.edu, 'Alcatel 601E DRIE Operation Manual', 2010. [Online]. Available: <http://cnm2.engineering.ucdavis.edu/>. [Accessed: 03- Apr- 2012].
- [12] E. Chow, V. Chandrasekaran, A. Partridge, T. Nishida, M. Sheplak, C. Quate and T. Kenny, 'Process compatible polysilicon-based electrical through-wafer interconnects in silicon substrates', *J. Microelectromech. Syst.*, vol. 11, no. 6, pp. 631-640, 2002.
- [13] S. Chang, J. Oh, S. Boles and C. Thompson, 'Fabrication of silicon nanopillar-based nanocapacitor arrays', *Applied Physics Letters*, vol. 96, no. 15, p. 153108, 2010.
- [14] G. Mariani, A. Scofield, C. Hung and D. Huffaker, 'GaAs nanopillar-array solar cells employing in situ surface passivation', *Nat Comms*, vol. 4, p. 1497, 2013.

- [15]E. Garnett and P. Yang, 'Silicon Nanowire Radial p–n Junction Solar Cells', *J. Am. Chem. Soc.*, vol. 130, no. 29, pp. 9224-9225, 2008.
- [16]C. Hsu, S. Connor, M. Tang and Y. Cui, 'Wafer-scale silicon nanopillars and nanocones by Langmuir–Blodgett assembly and etching', *Applied Physics Letters*, vol. 93, no. 13, p. 133109, 2008.
- [17]C. Cheung, R. Nikolić, C. Reinhardt and T. Wang, 'Fabrication of nanopillars by nanosphere lithography', *Nanotechnology*, vol. 17, no. 5, pp. 1339-1343, 2006.
- [18]A. Shalek, J. Robinson, E. Karp, J. Lee, D. Ahn, M. Yoon, A. Sutton, M. Jorgolli, R. Gertner, T. Gujral, G. MacBeath, E. Yang and H. Park, 'Vertical silicon nanowires as a universal platform for delivering biomolecules into living cells', *Proceedings of the National Academy of Sciences*, vol. 107, no. 5, pp. 1870-1875, 2010.
- [19]C. Xie, L. Hanson, Y. Cui and B. Cui, 'Vertical nanopillars for highly localized fluorescence imaging', *Proceedings of the National Academy of Sciences*, vol. 108, no. 10, pp. 3894-3899, 2011.
- [20]S. Boden and D. Bagnall, 'Bio-mimetic nanostructured surfaces for near-zero reflection sunrise to sunset', *Conference Record of the 2006 IEEE 4th World Conference on*, vol. 2, 2006.
- [21]Z. Fan, D. Ruebusch, A. Rathore, R. Kapadia, O. Ergen, P. Leu and A. Javey, 'Challenges and prospects of nanopillar-based solar cells', *Nano Research*, vol. 2, no. 11, pp. 829-843, 2009.
- [22]Z. Gong, Y. He, Y. Tseng, C. O'Neal and L. Que, 'A micromachined carbon nanotube film cantilever-based energy cell', *Nanotechnology*, vol. 23, no. 33, p. 335401, 2012.
- [23]Y. He, S. Vasiraju and L. Que, 'Hybrid nanomaterial-based nanofluids for micropower generation', *RSC Adv.*, vol. 4, no. 5, pp. 2433-2439, 2014.
- [24]Y. Tseng, Y. He and L. Que, 'Ultrasensitive thin film infrared sensors enabled by hybrid nanomaterials', *Analyst*, vol. 138, no. 10, p. 3053, 2013.
- [25]Y. Tseng, Y. He, S. Lakshmanan, C. Yang, W. Chen and L. Que, 'Optical and thermal response of single-walled carbon nanotube–copper sulfide nanoparticle hybrid nanomaterials', *Nanotechnology*, vol. 23, no. 45, p. 455708, 2012.
- [26]V. Kotipalli, Z. Gong, P. Pathak, T. Zhang, Y. He, S. Yadav and L. Que, 'Light and thermal energy cell based on carbon nanotube films', *Applied Physics Letters*, vol. 97, no. 12, p. 124102, 2010.
- [27]M. Seery, R. George, P. Floris and S. Pillai, 'Silver doped titanium dioxide nanomaterials for enhanced visible light photocatalysis', *Journal of Photochemistry and Photobiology A: Chemistry*, vol. 189, no. 2-3, pp. 258-263, 2007.
- [28]R. Yu, Q. Lin, S. Leung and Z. Fan, 'Nanomaterials and nanostructures for efficient light absorption and photovoltaics', *Nano Energy*, vol. 1, no. 1, pp. 57-72, 2012.
- [29]S. Lakshmanan, X. Zou, M. Hossu, L. Ma, C. Yang and W. Chen, 'Local Field Enhanced Au/CuS Nanocomposites as Efficient Photothermal Transducer Agents for Cancer Treatment', *Journal of Biomedical Nanotechnology*, vol. 8, no. 6, pp. 883-890, 2012.
- [30] nanoComposix, 'nanoComposix -Precisely engineered, highly characterized', 2015. [Online]. Available: <http://nanocomposix.com/>. [Accessed: 06- Mar- 2014].
- [31]J. Zhou, Y. Gao, Z. Zhang, H. Luo, C. Cao, Z. Chen, L. Dai and X. Liu, 'VO<sub>2</sub> thermochromic smart window for energy savings and generation', *Scientific Reports*, vol. 3, 2013.

- [32]I. Talian, K. Mogensen, A. Oriňák, D. Kaniansky and J. Hübner, 'Surface-enhanced Raman spectroscopy on novel black silicon-based nanostructured surfaces', *Journal of Raman Spectroscopy*, vol. 40, no. 8, pp. 982-986, 2009.
- [33]H. Jansen, M. Boer, R. Legtenberg and M. Elwenspoek, 'The black silicon method: a universal method for determining the parameter setting of a fluorine-based reactive ion etcher in deep silicon trench etching with profile control', *Journal of Micromechanics and Microengineering*, vol. 5, no. 2, pp. 115-120, 1995.
- [34]Z. Xiao, C. Feng, P. Chan and I. Hsing, 'Formation of Silicon Nanopores and Nanopillars by a Maskless Deep Reactive Ion Etching Process', *TRANSDUCERS 2007 - 2007 International Solid-State Sensors, Actuators and Microsystems Conference*, 2007.
- [35]Y. Deng and Y. Juang, 'Black silicon SERS substrate: Effect of surface morphology on SERS detection and application of single algal cell analysis', *Biosensors and Bioelectronics*, vol. 53, pp. 37-42, 2014.
- [36]Y. Tang, X. Xu, J. Fang, Y. Liang and H. Ji, 'The growth and superhydrophobicity of a perfluorocarbon nanoneedle array on an SiO<sub>2</sub> surface', *IEEE Trans. Nanotechnology*, vol. 5, no. 4, pp. 415-419, 2006.
- [37]H. Lo, H. Hsiung, S. Chattopadhyay, H. Han, C. Chen, J. Leu, K. Chen and L. Chen, 'Label free sub-picomole level DNA detection with Ag nanoparticle decorated Au nanotip arrays as surface enhanced Raman spectroscopy platform', *Biosensors and Bioelectronics*, vol. 26, no. 5, pp. 2413-2418, 2011.
- [38]M. fischer, T. kups, H. romanus, F. morales, G. ecke, M. hoffmann, C. knedlik, o. ambacher and j. pezoldt, 'Self organization and properties of Black Silicon', *Internationales Wissenschaftliches Kolloquium*, 2006.
- [39]S. Iijima, 'Helical microtubules of graphitic carbon', *Nature*, vol. 354, no. 6348, pp. 56-58, 1991.
- [40]Z. Ren, 'Synthesis of Large Arrays of Well-Aligned Carbon Nanotubes on Glass', *Science*, vol. 282, no. 5391, pp. 1105-1107, 1998.
- [41]E. Peer, A. Artzy-Schnirman, L. Gepstein and U. Sivan, 'Hollow Nanoneedle Array and Its Utilization for Repeated Administration of Biomolecules to the Same Cells', *ACS Nano*, vol. 6, no. 6, pp. 4940-4946, 2012.
- [42]R. Fan, Y. Wu, D. Li, M. Yue, A. Majumdar and P. Yang, 'Fabrication of Silica Nanotube Arrays from Vertical Silicon Nanowire Templates', *J. Am. Chem. Soc.*, vol. 125, no. 18, pp. 5254-5255, 2003.
- [43]S. Park, Y. Kim, W. Kim and S. Jon, 'Carbon Nanosyringe Array as a Platform for Intracellular Delivery', *Nano Letters*, vol. 9, no. 4, pp. 1325-1329, 2009.
- [44]J. VanDersarl, A. Xu and N. Melosh, 'Nanostraws for Direct Fluidic Intracellular Access', *Nano Letters*, vol. 12, no. 8, pp. 3881-3886, 2012.
- [45]L. Lauhon, M. Gudiksen, D. Wang and C. Lieber, 'Epitaxial core-shell and core-multishell nanowire heterostructures', *Nature*, vol. 420, no. 6911, pp. 57-61, 2002.
- [46]M. Ishai and F. Patolsky, 'Shape- and Dimension-Controlled Single-Crystalline Silicon and SiGe Nanotubes: Toward Nanofluidic FET Devices', *J. Am. Chem. Soc.*, vol. 131, no. 10, pp. 3679-3689, 2009.

- [47]R. Gao, S. Strehle, B. Tian, T. Cohen-Karni, P. Xie, X. Duan, Q. Qing and C. Lieber, 'Outside Looking In: Nanotube Transistor Intracellular Sensors', *Nano Letters*, vol. 12, no. 6, pp. 3329-3333, 2012.
- [48]X. Duan, R. Gao, P. Xie, T. Cohen-Karni, Q. Qing, H. Choe, B. Tian, X. Jiang and C. Lieber, 'Intracellular recordings of action potentials by an extracellular nanoscale field-effect transistor', *Nature Nanotech*, vol. 7, no. 3, pp. 174-179, 2011.
- [49]T. Hilder and J. Hill, 'Carbon nanotubes as drug delivery nanocapsules', *Current Applied Physics*, vol. 8, no. 3-4, pp. 258-261, 2008.
- [50]S. Penmetsa, K. Nagrajan, Z. Gong, D. Mills and L. Que, 'Biological cell controllable patch-clamp microchip', *Applied Physics Letters*, vol. 97, no. 26, p. 263702, 2010.
- [51]P. Pathak, H. Zhao, Z. Gong, F. Nie, T. Zhang, K. Cui, Z. Wang, S. Wong and L. Que, 'Real-time monitoring of cell viability using direct electrical measurement with a patch-clamp microchip', *Biomedical Microdevices*, vol. 13, no. 5, pp. 949-953, 2011.
- [52]J. Han, G. Paulus, R. Maruyama, D. Heller, W. Kim, P. Barone, C. Lee, J. Choi, M. Ham, C. Song, C. Fantini and M. Strano, 'Exciton antennas and concentrators from core-shell and corrugated carbon nanotube filaments of homogeneous composition', *Nat Mater*, vol. 9, no. 10, pp. 833-839, 2010.
- [53]Y. He, X. Che and L. Que, 'Characterization of the silicon nanopillar-surface filled and grafted with nanomaterials', *Mater. Res. Express*, vol. 1, no. 3, p. 035045, 2014.
- [54]Y. Tseng, Y. He, S. Lakshmanan, C. Yang, W. Chen and L. Que, 'Optical and thermal response of single-walled carbon nanotube-copper sulfide nanoparticle hybrid nanomaterials', *Nanotechnology*, vol. 23, no. 45, p. 455708, 2012.
- [55]K. Lau, J. Bico, K. Teo, M. Chhowalla, G. Amaratunga, W. Milne, G. McKinley and K. Gleason, 'Superhydrophobic Carbon Nanotube Forests', *Nano Letters*, vol. 3, no. 12, pp. 1701-1705, 2003.
- [56]F. Persson and J. Tegenfeldt, 'DNA in nanochannels—directly visualizing genomic information', *Chem. Soc. Rev.*, vol. 39, no. 3, p. 985, 2010.
- [57]S. Min, W. Kim, Y. Cho and K. Kim, 'Fast DNA sequencing with a graphene-based nanochannel device', *Nature Nanotech*, vol. 6, no. 3, pp. 162-165, 2011.
- [58] Wikipedia, 'Deep reactive-ion etching', 2015. [Online]. Available: [http://en.wikipedia.org/wiki/Bosch\\_process\\_%28microtechnology%29#Bosch\\_process](http://en.wikipedia.org/wiki/Bosch_process_%28microtechnology%29#Bosch_process). [Accessed: 02- Feb- 2015].
- [59]Y. Tang, X. Xu and J. Fang, 'Perfluorocarbon Nanofilament Array Formation on SiO<sub>2</sub> and the Hyperhydrophobicity of the Surface', *IEEE Transaction on Nanotechnology*, vol. 5, no. 4, pp. 415-419, 2006.
- [60]M. Mehran, S. Mohajerzadeh, Z. Sanaee and Y. Abdi, 'Nanograss and nanostructure formation on silicon using a modified deep reactive ion etching', *Applied Physics Letters*, vol. 96, no. 20, p. 203101, 2010.
- [61]C. Hedlund, 'Microloading effect in reactive ion etching', *Journal of Vacuum Science & Technology A: Vacuum, Surfaces, and Films*, vol. 12, no. 4, p. 1962, 1994.

- [62]A. Jones, M. Hitchman, M. Ritala, J. Niinisto, S. Krumdieck, P. Chalker, H. Aspinall, M. Pemble, W. Gladfelter and B. Leese, *Chemical vapour deposition*. Cambridge: Royal Society of Chemistry, 2008.
- [63]H. Lee, A. Wark and R. Corn, 'Microarray methods for protein biomarker detection', *Analyst*, vol. 133, no. 8, p. 975, 2008.
- [64]A. Qavi, A. Washburn, J. Byeon and R. Bailey, 'Label-free technologies for quantitative multiparameter biological analysis', *Analytical and Bioanalytical Chemistry*, vol. 394, no. 1, pp. 121-135, 2009.
- [65]S. Kingsmore, 'Multiplexed protein measurement: technologies and applications of protein and antibody arrays', *Nat Rev Drug Discov*, vol. 5, no. 4, pp. 310-321, 2006.
- [66]R. Karlsson, 'SPR for molecular interaction analysis: a review of emerging application areas', *Journal of Molecular Recognition*, vol. 17, no. 3, pp. 151-161, 2004.
- [67]S. Nie, 'Probing Single Molecules and Single Nanoparticles by Surface-Enhanced Raman Scattering', *Science*, vol. 275, no. 5303, pp. 1102-1106, 1997.
- [68]J. Zhao, X. Zhang, C. Yonzon, A. Haes and R. Van Duyne, 'Localized surface plasmon resonance biosensors', *Nanomedicine*, vol. 1, no. 2, pp. 219-228, 2006.
- [69]D. Georganopoulou, L. Chang, J. Nam, C. Thaxton, E. Mufson, W. Klein and C. Mirkin, 'From The Cover: Nanoparticle-based detection in cerebral spinal fluid of a soluble pathogenic biomarker for Alzheimer's disease', *Proceedings of the National Academy of Sciences*, vol. 102, no. 7, pp. 2273-2276, 2005.
- [70]X. Liu, Q. Dai, L. Austin, J. Coutts, G. Knowles, J. Zou, H. Chen and Q. Huo, 'A One-Step Homogeneous Immunoassay for Cancer Biomarker Detection Using Gold Nanoparticle Probes Coupled with Dynamic Light Scattering', *J. Am. Chem. Soc.*, vol. 130, no. 9, pp. 2780-2782, 2008.
- [71]S. Mandal and D. Erickson, 'Nanoscale optofluidic sensor arrays', *Opt. Express*, vol. 16, no. 3, p. 1623, 2008.
- [72]G. Hwang, L. Pang, E. Mullen and Y. Fainman, 'Plasmonic Sensing of Biological Analytes Through Nanoholes', *IEEE Sensors Journal*, vol. 8, no. 12, pp. 2074-2079, 2008.
- [73]I. White, H. Oveys, X. Fan, T. Smith and J. Zhang, 'Integrated multiplexed biosensors based on liquid core optical ring resonators and antiresonant reflecting optical waveguides', *Applied Physics Letters*, vol. 89, no. 19, p. 191106, 2006.
- [74]A. Ramachandran, S. Wang, J. Clarke, S. Ja, D. Goad, L. Wald, E. Flood, E. Knobbe, J. Hryniewicz, S. Chu, D. Gill, W. Chen, O. King and B. Little, 'A universal biosensing platform based on optical micro-ring resonators', *Biosensors and Bioelectronics*, vol. 23, no. 7, pp. 939-944, 2008.
- [75]V. Lin, 'A Porous Silicon-Based Optical Interferometric Biosensor', *Science*, vol. 278, no. 5339, pp. 840-843, 1997.
- [76]S. Pan and L. Rothberg, 'Interferometric Sensing of Biomolecular Binding Using Nanoporous Aluminum Oxide Templates', *Nano Letters*, vol. 3, no. 6, pp. 811-814, 2003.
- [77]T. Zhang, S. Talla, Z. Gong, S. Karandikar, R. Giorno and L. Que, 'Biochemical sensing with a polymer-based micromachined Fabry-Perot sensor', *Opt. Express*, vol. 18, no. 17, p. 18394, 2010.

- [78]T. Zhang, Z. Gong, R. Giorno and L. Que, 'A nanostructured Fabry-Perot interferometer', *Opt. Express*, vol. 18, no. 19, p. 20282, 2010.
- [79]T. Zhang, P. Pathak, S. Karandikar, R. Giorno and L. Que, 'A polymer nanostructured Fabry-Perot interferometer based biosensor', *Biosensors and Bioelectronics*, vol. 30, no. 1, pp. 128-132, 2011.
- [80]T. Zhang, Y. He, J. Wei and L. Que, 'Nanostructured optical microchips for cancer biomarker detection', *Biosensors and Bioelectronics*, vol. 38, no. 1, pp. 382-388, 2012.
- [81]Y. He, X. Li and L. Que, 'Fabrication and Characterization of Lithographically Patterned and Optically Transparent Anodic Aluminum Oxide (AAO) Nanostructure Thin Film', *J. nanosci. nanotech.*, vol. 12, no. 10, pp. 7915-7921, 2012.
- [82]V. Doan and M. Sailor, 'Luminescent Color Image Generation on Porous Silicon', *Science*, vol. 256, no. 5065, pp. 1791-1792, 1992.
- [83]S. Choi and M. Daughety, 'Growth and Engineering of High Aspect-Ratio AAO Templates Integrated on Silicon Substrates', *Technical Proceedings of the 2007 NSTI Nanotechnology Conference and Trade Show*, vol. 4, pp. 514-515, 2007.
- [84]M. Sander and L. Tan, 'Nanoparticle Arrays on Surfaces Fabricated Using Anodic Alumina Films as Templates', *Advanced Functional Materials*, vol. 13, no. 5, pp. 393-397, 2003.
- [85]L. Xiao and L. Duan, 'Fabrication of Large Area of Anodic Aluminum Oxide Ultrathin Film Directly onto an ITO Electrode with a Ti Buffer Layer', *Acta Physico-Chimica Sinica*, vol. 27, no. 3, pp. 749-753, 2011.
- [86]K. Musselman, G. Mulholland, A. Robinson, L. Schmidt-Mende and J. MacManus-Driscoll, 'Low-Temperature Synthesis of Large-Area, Free-Standing Nanorod Arrays on ITO/Glass and other Conducting Substrates', *Adv. Mater.*, vol. 20, no. 23, pp. 4470-4475, 2008.
- [87]X. Ren, T. Gershon, D. Iza, D. Muñoz-Rojas, K. Musselman and J. MacManus-Driscoll, 'The selective fabrication of large-area highly ordered TiO<sub>2</sub> nanorod and nanotube arrays on conductive transparent substrates via sol-gel electrophoresis', *Nanotechnology*, vol. 20, no. 36, p. 365604, 2009.
- [88]G. Sulka, S. Stroobants, V. Moshchalkov, G. Borghs and J. Celis, 'Synthesis of Well-Ordered Nanopores by Anodizing Aluminum Foils in Sulfuric Acid', *J. Electrochem. Soc.*, vol. 149, no. 7, p. D97, 2002.
- [89]H. Masuda and K. Fukuda, 'Ordered Metal Nanohole Arrays Made by a Two-Step Replication of Honeycomb Structures of Anodic Alumina', *Science*, vol. 268, no. 5216, pp. 1466-1468, 1995.
- [90]C. Pacholski, C. Yu, G. Miskelly, D. Godin and M. Sailor, 'Reflective Interferometric Fourier Transform Spectroscopy: A Self-Compensating Label-Free Immunosensor Using Double-Layers of Porous SiO<sub>2</sub>', *J. Am. Chem. Soc.*, vol. 128, no. 13, pp. 4250-4252, 2006.
- [91]T. Zhang, P. Pathak, S. Karandikar, R. Giorno and L. Que, 'A polymer nanostructured Fabry-Perot interferometer based biosensor', *Biosensors and Bioelectronics*, vol. 30, no. 1, pp. 128-132, 2011.
- [92]T. Zhang, Z. Gong, R. Giorno and L. Que, 'A nanostructured Fabry-Perot interferometer', *Opt. Express*, vol. 18, no. 19, p. 20282, 2010.
- [93]G. Mor, O. Varghese, M. Paulose, K. Ong and C. Grimes, 'Fabrication of hydrogen sensors with transparent titanium oxide nanotube-array thin films as sensing elements', *Thin Solid Films*, vol. 496, no. 1, pp. 42-48, 2006.

- [94]H. Masuda, 'Self-Ordering of Cell Arrangement of Anodic Porous Alumina Formed in Sulfuric Acid Solution', *J. Electrochem. Soc.*, vol. 144, no. 5, p. L127, 1997.
- [95]H. Suh and K. Lee, 'Reduction in switching current density for current-induced magnetization switching without loss of thermal stability: Effect of perpendicular anisotropy', *Current Applied Physics*, vol. 9, no. 5, pp. 985-988, 2009.
- [96]R. Furneaux, W. Rigby and A. Davidson, 'The formation of controlled-porosity membranes from anodically oxidized aluminium', *Nature*, vol. 337, no. 6203, pp. 147-149, 1989.
- [97]M. Born, E. Wolf and E. Hecht, 'Principles of Optics: Electromagnetic Theory of Propagation, Interference and Diffraction of Light', *Physics Today*, vol. 53, no. 10, pp. 77-78, 2000.
- [98]R. Murashko, V. Sumarokov, T. Dubovik, V. Kazakov and L. Struk, 'Crucibles for the electron-beam evaporation of aluminum', *Powder Metall Met Ceram*, vol. 13, no. 12, pp. 1000-1003, 1974.